Ph.D. Dissertation of Science

Evolution of deep convection associated with tropical cyclogenesis over the western North Pacific

북서태평양에서 태풍의 발생 과정에 나타나는 깊은 대류의 변화

Minhee Chang

August 2020

School of Earth and Environmental Sciences
Graduate School
Seoul National University

Evolution of deep convection associated with tropical cyclogenesis over the western North Pacific

북서태평양에서 태풍의 발생 과정에 나타나는 깊은 대류의 변화

Supervisor Chang-Hoi Ho, Professor

Submitting a Ph.D. Dissertation of Science
July 2020

School of Earth and Environmental Sciences
Graduate School
Seoul National University

Minhee Chang

Confirming the Ph.D. Dissertation written by
Minhee Chang
July 2020

Chair	_____	(Seal)
Vice Chair	_____	(Seal)
Examiner	_____	(Seal)
Examiner	_____	(Seal)
Examiner	_____	(Seal)

Evolution of deep convection associated with tropical cyclogenesis over the western North Pacific

By
Minhee Chang

A dissertation Submitted to the Faculty of the Graduate School of
Seoul National University in Partial Fulfillment of
the Requirements for the Degree of Doctor of Philosophy

Degree Awarded:
August 2020

Advisory committee:

Professor	Seok-Woo Son, Chair
Professor	Chang-Hoi Ho, Advisor
Professor	Johnny C. L. Chan
Professor	Myoung-Hwan Ahn
Doctor	Myung-Sook Park

Abstract

Multi-day episodes of deep convective bursts (mCB) during tropical cyclone (TC) genesis are easily observed and often considered to be a manifestation of gradual mesoscale organization process. However, their role as a prelude to TC genesis have not been clearly discovered whether every TC genesis is associated with mCB or if TC non-development is less associated with mCB. In this regard, evolution of mCB is investigated among 463 tropical disturbances that developed (80) or did not develop (383) into TCs over the western North Pacific during 2007–2009. Deep convection is identified by using geostationary satellite data when the infrared (IR) brightness temperature is lower than that of water vapor (WV). A diurnal increase from time series of IR minus WV < 0 areas within the disturbance is defined as a convective burst (CB) event, and when CBs occur for at least two consecutive days, it is defined as a mCB. The atmospheric variables from the Modern-Era Retrospective Analysis for Research and Applications, Version 1 and 2 as well as ECMWF ReAnalysis-5 are also analyzed for combined understanding on the multi-day convective-environmental evolution in TC formation.

The results show that mCB are observed in 67.5% of the 80 TC-developing disturbances (i.e., 54 TCs) and in 13.8% of the 383 non-developing disturbances (i.e., 53 disturbances). When the non-developing disturbances with mCB are compared to the developing disturbance with mCB, thermodynamic conditions are not significantly different. However, dynamic conditions are discriminated, as the mid-

to-low tropospheric relative vorticity of non-developing cases are significantly weaker and the vertical wind shear environment is significantly stronger, which account for eventual decay of non-developing disturbance despite the presence of a mCB. Additional analyses revealed that the unfavorable vertical wind shear is mainly formed in the mid-to-upper troposphere, rather than lower-to-mid troposphere. Scale decomposition further verified that the developing disturbances having mCB are located in between the attendant anticyclones, which might promote surface moisture convergence, while non-developing disturbances are not. A representative case study is evaluated by looking at the formation process of TC Hagupit (2008), which confirmed the findings from the composite analysis.

The remaining 32.5% of the TC cases (i.e., 26 TCs) which do not accompany mCB prior to their formation are characterized by abrupt activation of deep convection only one or two days prior to TC genesis in less favorable thermodynamic atmospheric environment compared to TC cases having mCB. Regarding the dynamic components, a vorticity maximum is located in the upper troposphere, with attendant strong vertical wind shear, which later redistributes to the lower-to-mid troposphere with associated abrupt deep convection shortly before TC formation. Particularly, 12 TC cases are the most evident in the vorticity trace in the upper troposphere. One TC formation case, TC Peipah (2007), is scrutinized. As a result, TC genesis process of these 12 TCs are explained by the process of tropical transition, which is commonly observed and well documented over the North Atlantic. The tropical transition is one type of TC genesis pathway regarding an extratropical

precursor transitioning into a TC. In addition, the occurrence of the extratropical precursor in the tropics or subtropics is explained by a strong potential vorticity intrusion in the subtropical upper troposphere, which explains the origin of vorticity maximum in the upper troposphere. The formation pathway of remaining 14 TCs largely resemble that of TC genesis having mCB, also having attendant anticyclones around the pre-TC disturbances. Yet, the magnitude of CB is not as strong as to be defined as mCB, and the location of vorticity maximum is located at the mid-troposphere. A representative case study among these 14 TCs is evaluated by looking at the formation process of TC Koppu (2009), which confirmed the findings from the composite analysis. To understand detailed formation pathway of these 14 TCs, further investigation is needed particularly regarding shallow convective clouds and mid-tropospheric vorticity maximum.

To summarize, this study reveals that mCB is a common feature in pre-TC stages but it cannot be used as an independent predictor for TC genesis. Firstly, because similar number of non-development disturbances are also associated with mCB, the strength of relative vorticity of the disturbance as well as vertical wind shear in the environment need to be considered. Secondly, as some of TC genesis occur after abrupt activation of deep convection, the external dynamic forcing like upper-tropospheric weather phenomena need to be considered as one candidate of TC formation precursors besides mCB. Yet, this study confirms that mCB is effective in filtering out many non-developing disturbances and also efficient in classifying various TC formation pathways.

Keyword: Tropical cyclone development, deep convection, diurnal variation, tropical disturbances, tropical transition, western North Pacific, tropical-extratropical interaction

Student Number: 2013-20340

Table of Contents

List of Tables

List of Figures

1. Introduction

Tropical cyclone (TC) formation requires the transformation of a pre-existing tropical disturbance into a warm core vortex with organized convection—here, TC formation is defined as a process of tropical disturbance transforming into a tropical depression (13–17 m s^{-1}) as indicated by the Joint Typhoon Warning Center best-track dataset (Briegel and Frank 1997; Ritchie and Holland 1999; Davis and Ahijevych 2012). Although more than a hundred tropical disturbances occur over the western North Pacific (WNP) every year, only about 27 TCs develop on average (Ritchie and Holland 1999). Unexpected TC formation accompanying a sudden occurrence of strong gusts, thunderstorms, and heavy rainfall, can seriously threaten adjacent islands and coastal areas. Accordingly, identifying the disturbances that will develop into TCs among many disturbances is one of the vital tasks of operational TC centers. TC formation involves multi-scale phenomena (Houze et al. 2009; Dunkerton et al. 2008) and accompanies interactions between convection and large-scale environments (Cheung et al. 2018). Since large-scale environment conditions favorable to TC genesis are well recognized (Gray 1968), recent focus has been placed on mesoscale impacts, particularly on the contribution of mesoscale convective systems to lower-tropospheric spin up (Bister and Emanuel 1997; Hendricks et al. 2004; Montgomery et al. 2006). While debate still exists concerning which part of the mesoscale convective system (convective or stratiform precipitation region) plays a more significant role in developing tropical disturbances

into TCs, all pathways emphasize the role of cloud clusters that develop up to the tropopause level.

Detailed studies on the dynamic and thermodynamic structure of deep convection in TC formation were performed by comparing tropical disturbances that developed into TCs with those that did not (Raymond and Carrillo 2011; Raymond et al. 2011; Zawislak and Zipser 2014a,b). Using aircraft data in the National Aeronautics and Space Administration's Genesis and Rapid Intensification Processes project, the National Science Foundation/the National Center for Atmospheric Research Pre-Depression Investigation of Cloud-Systems in the Tropics program, and the National Oceanic and Atmospheric Administration Intensity Forecasting Experiment as well as passive microwave satellite measurements, Zawislak and Zipser (2014a) compared the time evolution of the pre-genesis stage of twelve developing cases and three non-developing cases. They indicated area and frequency of rainfall are greater in developing disturbances than non-developing disturbances. Zawislak and Zipser (2014b) also analyzed the thermodynamic conditions for the same developing and non-developing cases using dropsonde data. The results revealed a near-saturated environment in low- to mid-levels for two days prior to TC genesis. The authors also highlight the role of an initially strong midlevel vortex in a humid environment for lower-tropospheric TC vortex intensification, which is consistent with Raymond and Carrillo (2011) and Raymond et al. (2011). Using the aircraft Doppler radar retrievals during Tropical Cyclone Structure-08 experiment, Park and Elsberry (2013) showed that the

convective burst (CB) in the pre-Nuri mission has a lower-tropospheric maximum in latent heating, and that it is a favorable condition for lower-tropospheric spin up. By contrast, non-developing tropical disturbances have deeper layers of nearly identical condensational heating and evaporative cooling rates. In general, understanding of convective processes and relevant dynamical and thermodynamical responses leading to TC formation has been greatly improved by the use of in situ aircraft measurements in recent field campaigns as well as satellite observations. Nevertheless, due to a low frequency of such observations, the limited number of samples collected from each stage of development remains an obstacle to general understanding of the multi-day convective evolution prior to TC genesis.

Taking advantage of the continuity of geostationary infrared (IR) observations, Kerns and Chen (2013) compared developing versus non-developing cloud clusters defined using the cloud top temperature threshold of 208 K. Most TC formation events are related to cloud clusters lasting at least 8 hours (8 h clusters); however, convection associated with non-developing cases also contained 8 h clusters. This implies that the cluster duration alone is not a sufficient condition for TC formation. These authors documented that, rather than the differences in the convection features of the cloud clusters, large-scale environments (e.g., lower-tropospheric vorticity, vertical wind shear, and convergence) are statistically more favorable for developing cloud clusters. Short lifetime of an individual cloud cluster, however, may not properly represent evolutions of a tropical disturbance, which consists of multiple cloud clusters. While cloud clusters tend to develop and decay, primarily following

the typical diurnal cycle over the tropical ocean (Gray and Jacobson 1977; Mapes and Houze 1993; Yang and Smith 2006; Park et al. 2011), tropical disturbance circulations tend to persist for multiple days prior to the genesis of a TC. An earlier study by Zehr (1992) examined the multi-day evolutions of cold IR brightness temperatures (BTs) near tropical disturbances prior to TC formation. Their study shows an earlier convective maximum two days prior to TC genesis, but relatively suppressed convection as genesis is near (also in Zawislak and Zipser 2014a). A recent IR study by Davis and Ahijevych (2012) showed multiple diurnal CBs throughout pre-formation stages and emphasized that the related quasi-persistent deep moist convection (and latent heating) is critical for developing low and mid-tropospheric mesoscale circulations into a TC.

Contrary to general vorticity precursor in the lower-to-mid troposphere over the WNP, upper-tropospheric forcing assisting TC formation has been widely studies over the North Atlantic (Bracken and Bosart 2000; Davis and Bosart 2004; Bentley et al. 2016). For instance, as strong PV intrudes from the extratropical lower stratosphere into the tropical upper troposphere, deep convection can be stimulated at the leading edge of the PV tongue (Funatsu and Waugh 2008; Kiladis 1998; McIntyre and Palmer 1983; Postel and Hitchman 1999; Waugh and Funatsu 2003). The localized deep convection can be driven by a quasi-geostrophic forcing for ascent as either positive differential vorticity advection (Trenberth 1978) or positive PV advection (Hoskins et al. 1985) by the thermal wind. Alternatively, the colder and drier air transported into the upper troposphere serves to destabilize the

tropospheric column by enhancing convective available potential energy (CAPE), thus to foster convectively favorable environments (Juckes and Smith 2000). The associated anticyclonic wave breaking (and PV streamer) over the tropical eastern Pacific and North Atlantic has been attributed to the formation of subtropical cyclones, which can subsequently undergo tropical transition (Davis and Bosart 2003, 2004; Galarneau et al. 2015; Bentley and Metz 2016; Bentley et al. 2017).

On seasonal to climate time-scales, however, the detrimental role of the upper-tropospheric features on TC formations is recently reported in relation with shear and low enthalpy air accompanied with it. For instance, the interannual or the long-term trend of the westward shift in the tropical upper-tropospheric trough (TUTT) is found to alter the mean TC genesis location to the west as well as to suppress the TC genesis frequency in the eastern WNP basin (Wang and Wu 2016; Wu et al. 2015). Similarly, frequent breaking of extratropical Rossby waves is found to decrease the total TC numbers and their intensities as well as to shorten the lifetime of TCs over the North Atlantic basin (Zhang et al. 2016, 2017). The strong vertical wind shear and the transport of cold and dry air associated with such upper-tropospheric features result in tropospheric moisture reduction and significant downdrafts that cause convection to collapse (Ge et al. 2013; Tang and Emanuel 2012).

This study aims to complement the efforts of these prior studies by quantifying and comparing multi-day convective-environmental evolutions associated with developing and non-developing disturbances. Focus is paid, in particular, to a series of CB or pulse events over several consecutive days, since the transition from a

tropical disturbance into a tropical depression is hypothesized to require quasi-stationary latent heating release rather than instantaneous heating. While understanding general convective evolution prior to TC genesis, there may exist some exceptional TC genesis cases showing abrupt organization of deep convection. For these cases, further investigation on the external forcing promoting deep convection around TC precursor and their eventual formation pathway will be introduced. Therefore, this work investigates a total of 463 disturbances—80 developing and 383 non-developing—over the WNP from 2007 to 2009 to answer the following questions:

(1) what percentage of the multiple occurrences of diurnal CBs (multi-day diurnal CB or hereinafter called mCB) are related to TC genesis and non-development,

(2) how large-scale dynamic and thermodynamic variabilities modulate the multi-day evolution of convection for TC genesis and non-development processes, and

(3) how developing disturbance without mCB, if this exists, manage to form a TC?

This manuscript is organized as follows. The datasets and methodology used are introduced in sections 2. In section 3.1, the overall deep convection characteristics will be investigated among all developing and non-developing disturbances, and they will be classified according the occurrence of mCB. In section 3.2, TC genesis pathway having mCB will be investigated in composite analysis in

comparison with non-developing disturbances having mCB, and a case study. In section 3.3, TC genesis pathway not having mCB will be investigated in composite analysis as well as a case study. In section 4 remaining issues, such as a discussion on the role of mCB as a TC genesis precursor, or further discussion on potential vorticity (PV) intrusion on TC genesis will be given. Finally, this study will be concluded in section 5.

2. Data and Methodology

2.1. Data

2.1.1. Tropical disturbance track

Total three types of track datasets over the WNP (0º–40ºN, 100ºE–180º shown in Figure 1) for 2007–2009 are used. For developing disturbances, two track datasets are used. First, six-hourly International Best Track Archive for Climate Stewardship (IBTrACS) data is used as a reference track for developing disturbances. Second, six-hourly Joint Typhoon Warning Center best-track data is used to find TC formation time, a first designation time as a tropical depression. For non-developing disturbances, 3-hourly tropical cloud cluster (TCC) track data (Hennon et al. 2011) is used as a reference track. This TCC track data provides the track of disturbances that can dan evolve into TCs.

2.1.2. Satellite retrieved brightness temperatures

For geostationary satellite data, infrared (IR; centered at 10.8 μm) and water vapor (WV; centered at 6.75 μm) channel BTs from the Multifunctional Transport Satellite-1R (MTSAT-1R) are used. The MTSAT-1R data (Puschell et al. 2002) was obtained from National Meteorological Satellite Center, Korea. The MTSAT-1R, centered at 0º, 140ºE, observes the major TC formation area over the same spatial and temporal domain with best-track data. The BT data are available every hour at 4 km resolution. Such high-resolution data, both in time and space, enabled us to

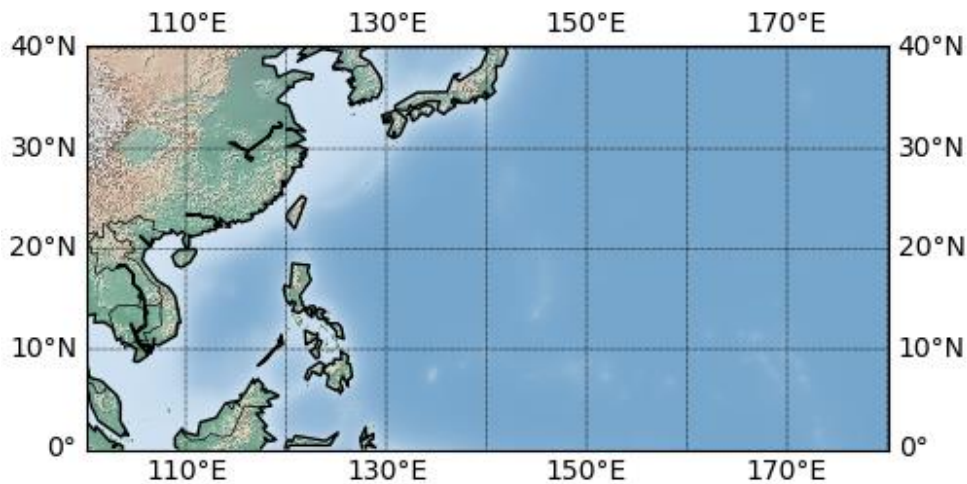

Figure 1. Analysis domain of this study (0º–40ºN, 100ºE–180º).

examine the hourly variability of mesoscale cloud features embedded in large-scale or synoptic-scale precursors (larger than 2000 km in diameter) for five to seven continuous days.

2.1.3. Atmospheric fields from reanalysis

Modern Era Retrospective-analysis for Research and Applications (MERRA) data version 1 and 2 (Bosilovich et al. 2016) are used to track the tropical disturbance vort-max and examine large-scale environmental conditions over the same spatial and temporal domain with the track data. The data is provided in three-hourly intervals at 1.25º latitude × 1.25º longitude for MERRA and at 0.5º latitude × 0.625º longitude for MERRA-2 horizontal resolutions on 42 vertical pressure levels from 1000 hPa to 100 hPa in the National Aeronautics and Space Administration Goddard Earth Sciences Data and Information Services Center online archive (https://disc.gsfc.nasa.gov/). In terms of variables, 600 hPa Ertel's PV is used for the tropical disturbance vort-max tracking. Ertel PV, temperature, zonal and meridional wind, vertical velocity (omega), relative humidity and specific humidity at all pressure levels are analyzed for environmental conditions. When examining the disturbance inner-core temperature, zonal temperature anomaly is used by subtracting the longitudinal average in each latitude. From the variables obtained from MERRA-2 dataset, relative vorticity, divergence, potential temperature, and moisture flux divergence at every pressure level, vertical wind shear between 200 and 850 hPa, and CAPE are calculated. Also, the Ertel PV in isobaric surface is

interpolated on the 350-K potential temperature surface to analyze the PV on an isentropic surface. In order to verify the evolution of lower-to-mid tropospheric relative vorticity associated with convective updrafts, the stretching component in the vorticity equation is calculated and integrated over the time domain starting from the first day of analysis (t_0) $\left(\text{i. e., } \int_{t_0}^{t} -(\zeta + f)\left(\frac{\partial u}{\partial x} + \frac{\partial v}{\partial y}\right) dt\right)$.

The advantage of using MERRA and MERRA-2 is that the three-dimensional atmospheric data are provided at higher temporal resolutions than other global reanalysis data of six-hourly temporal resolutions (https://gmao.gsfc.nasa.gov/reanalysis/MERRA/intro.php) except for ECMWF ReAnalysis-5 (ERA-5). As ERA-5 dataset, one-hourly 0.25º latitude × 0.25º longitude resolution, is released in 2019. Therefore, all the analysis is also validated by using ERA-5.

For daily mean sea surface temperature (SST), the Optimum Interpolation Sea Surface Temperature version 2 (OISST V2) dataset is analyzed, which is provided at 0.25° latitude × 0.25° longitude. The OISST V2 dataset (Reynolds et al. 2007) was obtained from the web site of the National Oceanic & Atmospheric Administration's Office of Oceanic and Atmospheric Research/Earth System Research Laboratory Physical Sciences Division, Boulder, Colorado, USA (https://www.esrl.noaa.gov/psd/).

2.2. Methodology

2.2.1. Potential vort−max tracking

Since any best-track data begins at only several hours before TC formation, five-to-seven-day pre-genesis and two-day post-genesis vort-max positions within developing disturbances, and five-day positions within non-developing disturbances are obtained in this study by following the 600 hPa MERRA PV maxima. Because the 600 hPa layer is a non-divergent layer (Cressman 1961), TC precursor vortex is likely to be traced with low error.

The tracking procedure finds a vort-max position which is a mean location with PV greater than the average for one standard deviation (i.e., vort-max) within a 500 km radius circle centered at the reference position. For developing disturbances (Figure 2a), TC formation day was set to Day 6, and IBTrACS data is used as a reference position, when it is available (Day 6 and 7), to search for the vort-max position. When IBTrACS data is not available (Day 1–5), the vort-max position at neighboring time step at 6 hourlies is employed as a reference position to search for the vort-max position. Similarly, TCC track data is used as a reference position for non-developing disturbances. Among the five-day lifetime of the non-developing disturbances, the day with the largest CB (a day with largest expanded convection area) was set to Day 4, and the TCC track on Day 4 is used as a reference position to find the vort-max position. For the remaining days (Day 1–3 and 5), the vort-max position at neighboring time step is again employed as a reference position to search

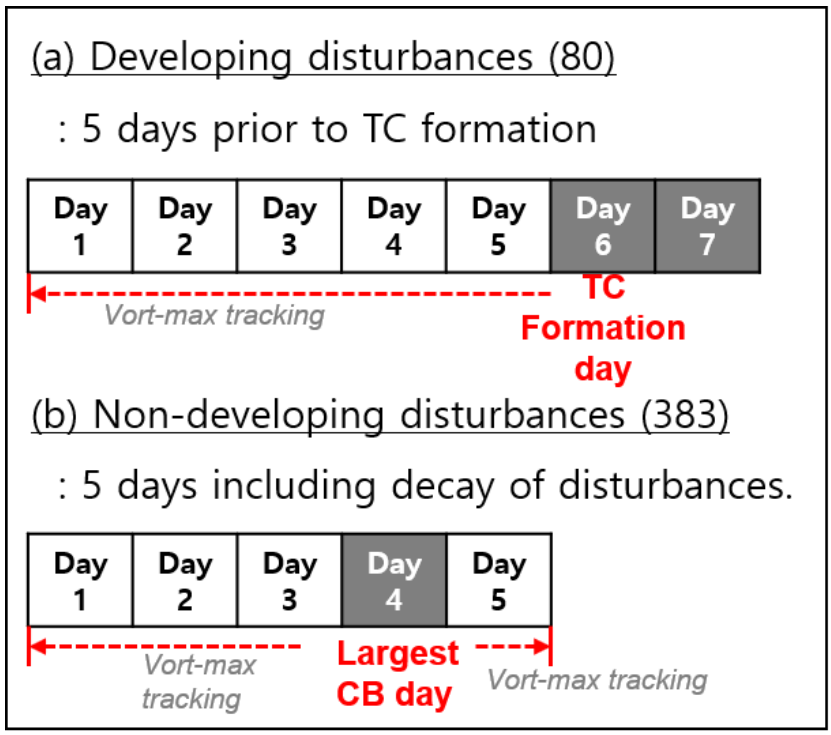

Figure 2. The vort-max procedure on (a) developing and (b) non-developing disturbances.

Table 1. Mean, median, standard deviation of distance between IBTrACS track data and vort-max track data.

	Mean	Median	Standard deviation
Distance	148.3 km	147.3 km	50.5 km

for the vort-max position.

Whereas TCC data detects cloud clusters from the satellite observation, some of non-developing samples may have very weak relative vorticity in the lower-tropospheric (925–850 hPa). To eliminate such disturbances, the non-developing samples with lower-tropospheric vorticity weaker than 5×10^{-6} s^{-1} on Day 4 (Kerns et al. 2008) were eliminated. Also, non-developing disturbances which dissipated due to landfall on Day 5 were eliminated. In addition, several constraints are imposed to eliminate tracks on the domain rim or with irregular movement regarding background advection. After applying these restrictions, 80 developing and 383 non-developing disturbance vort-max tracks are selected for this study.

For simple validation of the vort-max track confidence, this study calculated the distance statistics between IBTrACS track data and vort-max track data. Note that the calculation is only available for the period that IBTrACS data is valid, i.e., some of Day 5 and all Day 6 and 7. The average distance is 148.3 km (1.4 degree), median is 147.3 km (1.4 degree), and standard deviation is 50.5 km (0.47 degree). Considering that our convection area and atmospheric field analysis domain are within 500 km radius and 5-degree radius, respectively, the present result is less likely sensitive to current discrepancy.

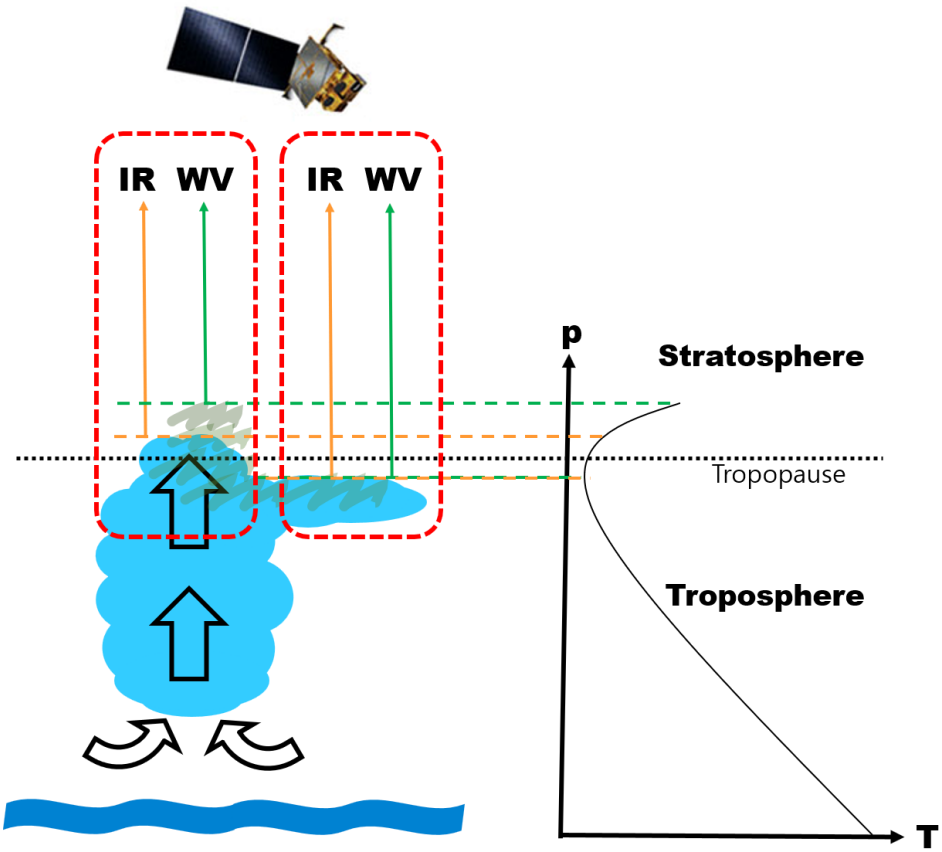

Figure 3. Simple schematics on (left) anvil clouds with convection overshooting and cirrus and (right) average vertical temperature profile in the troposphere and lower stratosphere.

2.2.2. Deep convection area determination

Cloud types are identified from the difference between the two BTs (IR minus WV BTs); deep convection reaching the tropopause when IR minus WV BTs becomes negative, and cirrus when IR minus WV BTs value is positive but small. This method is adopted because, compared to an IR only methodology, IR minus WV BTs is known to be advantageous in identifying deep convective clouds by filtering out cirrus (Bessho et al. 2001; Olander and Velden 2009; Chang et al. 2017). Whereas WV BT is generally lower than or similar to IR BT in the troposphere (anvil cirrus in Figure 3), if convection penetrates the tropopause, WV reaching the lower stratosphere would have higher BT than IR-detected cloud-top temperature near the tropopause due to the atmospheric lapse rate inversion in the stratosphere (Schmetz et al. 1997). Accordingly, negative IR minus WV BTs represents a signal left by the tropopause-penetrating deep convection (convection overshooting in Figure 3).

This study also briefly verifies IR minus WV BTs in comparison with radar reflectivity profiles at 13.8 GHz from Tropical Rainfall Measuring Mission (TRMM) Precipitation Radar (PR). The PR provides the reflectivity profiles at 80 vertical levels from near-surface to the 20 km level. While previous studies (Bessho et al. 2001; Olander and Velden 2009) applied the IR minus WV BTs methodology at mature TC cases, Figure 4 displays the pre-Nuri (2008) case at 1533 UTC 15 August 2008, a day prior to tropical depression formation. Moderate convection with IR BT < 250 K is widely distributed near the pre-Nuri vortex center (Figure 4a), which may contain cirrus as well as deep convection regions. Multiple areas with IR minus WV

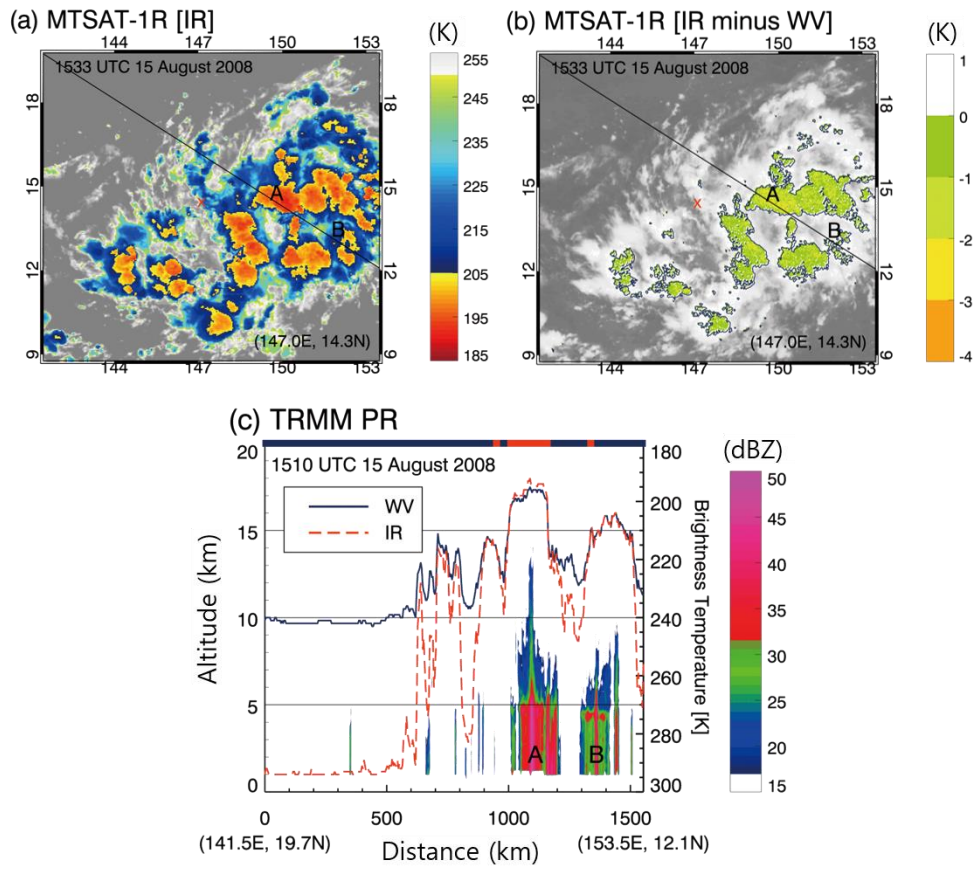

Figure 4. Deep convection feature of the pre-NURI disturbance centered at 14.27ºN, 146.97ºE (red x), observed by two satellites on 15 August 2008; (a) MTSAT-1R infrared (IR) temperature (K), (b) MTSAT-1R brightness temperature difference between IR) and water vapor (WV) channels (K), and (c) vertical cross-section of TRMM PR reflectivity (dBZ; shading) together with the distribution of brightness temperatures of MTSAT-1R IR (blue solid line) and WV (red dashed line) along the black solid line in (a) and (b). In panel c, the ordinate on the left (right) side indicates vertical height in km (brightness temperature in K), and the abscissa on the top represents negative (positive) IR minus WV BTs with red (blue) thick line.

BTs < 0 (Figure 4b) are embedded within a relatively narrow area compared to IR BT < 250 K. The vertical cross-section of the PR reflectivity along the "A" region indicates a deep convection tower with a 13 km PR echo and the surrounding 8–10 km echo tops (Figure 4c). The PR can only detect precipitation-sized ice particles (Park et al. 2007) and is not sensitive to small cloud ice particles. The 13 km PR echo top may indicate much higher cloud top or deeper convection tower. Although cold IR BTs < 210 K are partly observed over the convection cell marked "B" (Figure 4c), the PR radar echo top is lower and the IR minus WV BTs < 0 area is much smaller in this region. Accordingly, IR minus WV BTs < 0 is reasonably correlated with the deep convection tower observed by the PR (more cases were examined but are not shown). Although different thresholds values (e.g., IR minus WV BTs < –1 K, –2 K, or –3 K) have been examined (personal communication with Chris Velden, 2015), areas of deep convection defined here are not very sensitive to these threshold values, and 0 is thus used as the threshold.

Following the 500 km radii relative to the vort-max track, one-hourly time series of IR minus WV BTs < 0 area is constructed and smoothed using a 7-hour running mean as seen an example of Typhoon Sinlaku (2008) in Figure 5. In addition to the positive trend as the genesis nears, the time series of IR minus WV BTs < 0 areas are largely characterized by diurnal variability, with oceanic convection maxima showing in the morning (0600–0900 LT) and minima in the afternoon (1500–1800 LT). (All composite analyses hereafter is shown in local time to demonstrate the diurnal variability.)

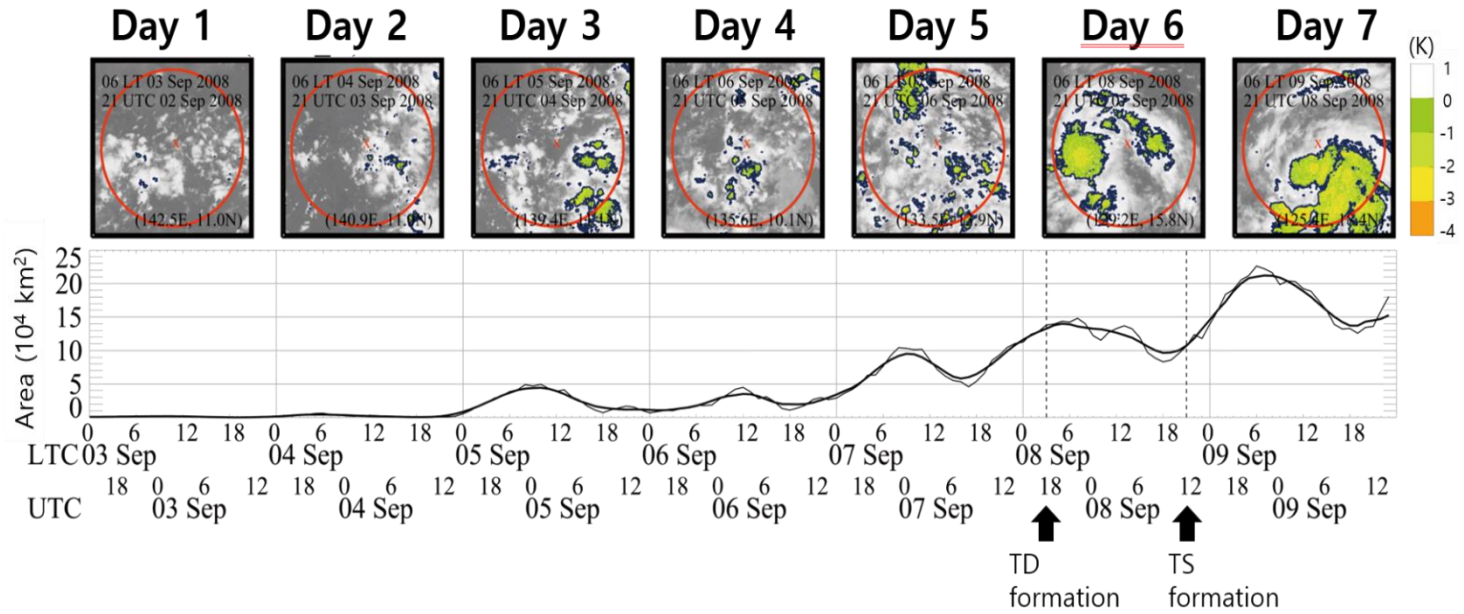

Figure 5. (Top) IR minus WV BTs images of Typhoon Sinlaku (2008) at 6 LT each day (3–9 September 2008). The red circle represents 500 km radius from the vort-max (red 'x') with specific coordinate indicated at the bottom right. (Bottom) Time series of deep convective area constructed from hourly IR minus WV BTs < 0 areas (thin solid line) and its 7-hour running mean (thick solid line). The first and second vertical dashed line each indicates when tropical depression (TD) and tropical storm (TS) forms, respectively.

2.2.3. Hanssen–Kuipers Skill Score

To find lower-limit thresholds applicable to all CB features, Hanssen-Kuipers Skill Score (KSS or Pierce Skill Score or True Skill Statistic) is used for statistical assessment. KSS is defined with simple calculation of hit rate minus false alarm rate, as introduced in Eq 1.

$$\boldsymbol{KSS = Hit\ rate\ - False\ alarm\ rate = \frac{AD - BC}{(A + C)(B + D)}} \qquad \textbf{Eq 1}$$

Here, A, B, C and D are presented in Table 2. KSS is useful in measuring the ability of the forecast to distinguish occurrences and non-occurrences of the event. In this work, the "event" refers to the occurrence of mCB.

2.2.4 Quasi–geostrophic analysis

To evaluate dynamics associated with upper-tropospheric trough before TC formation, quasi-geostrophic ascent/descent are calculated at each pressure level using zonal, meridional and vertical winds and temperatures. This study employed the same method as in Fischer et al. (2017), that solves a modified version of the Sutcliffe–Trenberth form of the quasi-geostrophic omega equation (Eq 2) (Trenberth 1978) using successive over-relaxation.

$$\left(\sigma\nabla^2 + {f_0}^2\frac{\partial^2}{\partial p^2}\right)\omega = f_0\left[\frac{d}{dp}\boldsymbol{V}_\psi \cdot \nabla(\zeta + f) - \nabla^2\left(\boldsymbol{V}_\psi \cdot \nabla\frac{\partial \psi}{\partial p}\right)\right] \qquad \textbf{Eq 2}$$

Table 2. Typical 2 × 2 contingency table.

		Event observed		**Total**
		Yes	**No**	
Event forecast	**Yes**	A (Hit)	B (False alarm)	A+B
	No	C (Miss)	D (Correct negative)	C+D
	Total	A+C	B+D	

2.2.5 Barotropic and Baroclinic Energy Conversion

To evaluate the energetics associated with TC formation, the mean flow and the eddy component are separated by applying a Lanczos filter (Duchon 1979) to zonal and meridional winds at each level. Following Dunkerton et al. (2008), the mean flow is defined as slowly-varying environmental flow which has time scale longer than 9 days, and the eddy is defined as the disturbance with 2.5-to-9-day frequency which may encompass pre-TC circulation.

Here, the barotropic energy conversion (BTEC) from mean kinetic energy (MKE) to eddy kinetic energy (EKE) is calculated as (Hoskins et al. 1983; Cai et al. 2007):

$$\boldsymbol{BTEC} = \frac{\boldsymbol{\partial EKE}}{\boldsymbol{\partial t}} = -\frac{\boldsymbol{\partial MKE}}{\boldsymbol{\partial t}}$$
$$= \frac{\boldsymbol{p_0}}{\boldsymbol{g}}\left\{\frac{\boldsymbol{1}}{\boldsymbol{2}}\left(\boldsymbol{v'^2} - \boldsymbol{u'^2}\right)\left(\frac{\boldsymbol{\partial \bar{u}}}{\boldsymbol{\partial x}} - \frac{\boldsymbol{\partial \bar{v}}}{\boldsymbol{\partial y}}\right) + \left(-\boldsymbol{u'v'}\right)\left(\frac{\boldsymbol{\partial \bar{v}}}{\boldsymbol{\partial x}} + \frac{\boldsymbol{\partial \bar{u}}}{\boldsymbol{\partial y}}\right)\right\}, \quad \textbf{Eq 3}$$

where u and v denote the zonal and meridional wind, respectively, p_0 (1000 hPa) denotes the reference pressure, and g (9.8 m s^{-2}) is gravitational acceleration. The overbar and apostrophe denote time-averaged values by applying a nine-day Lanczos low-pass filter and their residuals, respectively.

2.2.6 Cyclone phase space diagram

To objectively identify thermal structure of pre-TC, the cyclone phase diagram (Hart 2003) is examined by using isobaric height values. This analysis includes calculations on the three components. First, 900–600 hPa geopotential thickness symmetry within 500 km radius relative to the storm motion (B) is calculated by using following Eq 4.

$$\boldsymbol{B = h(\overline{Z_{600\,hPa} - Z_{900\,hPa}}|_R - \overline{Z_{600\,hPa} - Z_{900\,hPa}}|_L),} \quad \textbf{Eq 4}$$

where Z is isobaric height, R and L respectively represents right and left of current storm motion, and the overbar denotes the areal average within a 500 km radius semicircle. The integer h is a positive (negative) unit value for the Northern (Southern) Hemisphere. The other two values are the upper-tropospheric (600–300 hPa) thermal wind (–VTU), and the lower-tropospheric (900–600 hPa) thermal wind (–VTL). They are calculated as below.

$$\boldsymbol{V_T{}^L = -\frac{\partial(\Delta Z)}{\partial \ln p}\Big|_{900\,hPa}^{600\,hPa}}, \text{ and} \quad \textbf{Eq 5}$$

$$\boldsymbol{V_T{}^U = -\frac{\partial(\Delta Z)}{\partial \ln p}\Big|_{600\,hPa}^{300\,hPa}}, \quad \textbf{Eq 6}$$

where, the cyclone height perturbation ($\Delta \boldsymbol{Z}$) within the 500 km radius is defined as the difference between the maximum and minimum values,

$$\boldsymbol{\Delta Z = Z_{MAX} - Z_{MIN},} \quad \textbf{Eq 7}$$

which is also proportional to the magnitude of geostrophic wind, in thermal wind relationship.

2.2.7 Decision tree

To objectively identify the role of mCB as one of TC genesis precursors, decision tree algorithm is adopted. Decision tree is a non-parametric supervised learning method and a white box model which automatically learns the attributes and returns the optimal binary classification method. This method can also be used for regression, but classification more fits to the aim of this study to determine TC formation/non-formation. Thus, the method for classification is adopted here to understand the hierarchical relationships among the attributes.

The predictors are composed of several quantities representing deep convection and atmospheric environments associated with TC genesis. In terms of deep convection, some of CB features which will be described in section 3.1.1 are adopted as well as the occurrence of mCB. In terms of atmospheric environments, the 850-hPa relative humidity and 200-hPa PV, 850-hPa relative vorticity, and 850-and 200-hPa horizontal winds from ERA-5 are analyzed. For the relative vorticity, lanczos low-pass, band-pass, and high-pass filters with the thresholds of 2.5- and 9-days are applied to obtain relative vorticity in different time scales. For the vertical wind shear, 9-days low-pass filter is also applied for horizontal winds to calculate vertical wind shear of slowly-varying shear environment. Total ten attributes are trained with decision tree model to find the hierarchical relationships in association with TC genesis. Here we set 7:3 ratio to randomly divide training and test sets.

The decision tree algorithm is fitted to meet a user-defined total sample weighted impurity of the terminal nodes. Here, the terminal nodes refer to each

branch layer which is automatically defined according to the defined impurity in this study. The impurity used here is Gini impurity, which is calculated as $1-\left(\frac{a}{a+b}\right)^2-\left(\frac{b}{a+b}\right)^2$, where a and b are classified labels. When the Gini impurity is normalized by the sample number, information gain is obtained. Finally, a decision tree constructs binary trees using the feature and threshold that yield the largest information gain at each node.

3. Results

3.1. Features of multi-day Convective Bursts (mCB)

3.1.1. Deep convection characteristics overall

Based on the time series, increases in the deep convection area, i.e., CBs, are detected. During the detection, four primary CB features were identified (Figure 6): CB duration (Δt), expanded deep convection area (ΔA), maximum deep convection area (max(A)) and expanding rate (ΔA/Δt). In Figure 7a, the seven-day IR minus WV BTs time series of Hagupit (2008) is presented with 10 detected CBs. To exclusively focus on the diurnal cycle of deep convection, the membership of CB is defined as the date when its deep convection area reached its maximum (the date of max(A)). For example, the membership of CB spanning from 15 Sep to 16 Sep in Hagupit is Day3. Likewise, the membership of CB spanning from 19 Sep to 20 Sep is Day 7 because the CB reached its maximum at 0000 LTC 20 Sep. Then, if more than two CBs share the same membership, a CB with the largest ΔA is selected. For Day 1, as one small CB and one large CB exist, the larger one is chosen to be 'Day 1 CB'. For Day 2, no CB exists, and so on. Similarly, the same detection process is applied for non-developing disturbances as '40021' example in 2008 shown in Figure 6b. Finally, from 80 developing disturbances, 494 CB events (342 in pre-genesis stage and 152 from after genesis stage) were detected. From the 383 non-developing disturbances, 1661 CB events were detected.

To quantitatively compare the differences in the CB features between non-

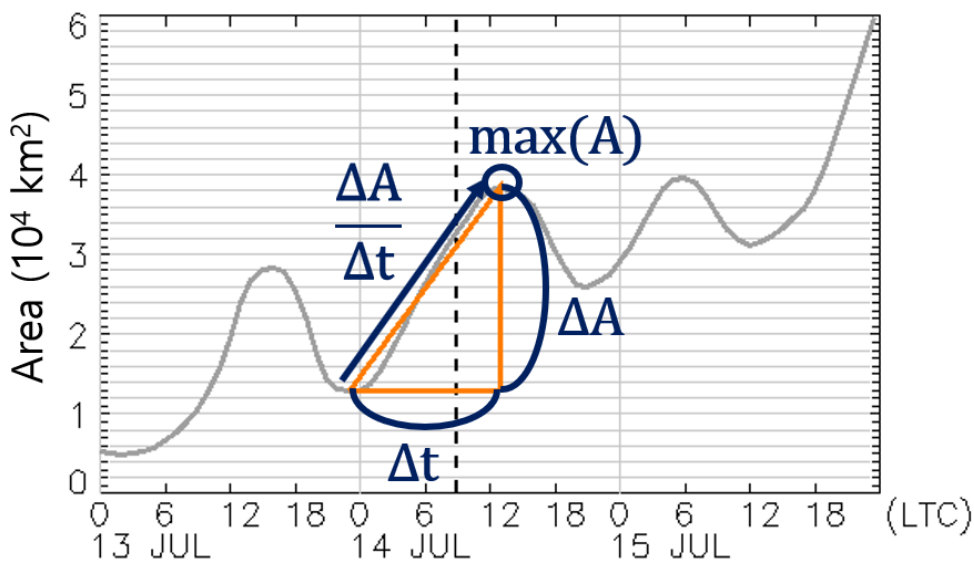

Figure 6. Four primary CB (orange) features (dark blue) indicated on the schematic IR minus WV BTs time series (gray): the CB duration (Δt), expanded deep convection area (ΔA), maximum deep convection area (max(A)) and expanding rate (ΔA/Δt). The four primary CB features are defined from the increasing signal of the deep convection area (orange triangle) every day.

developing and developing disturbances, the normalized frequency distributions for the three categories are shown (Figure 8). For the developing disturbances, the pre- and post-genesis stage are separated for equivalent comparison of pre-TC disturbances with non-developing disturbances. When compared to non-developing disturbances, the duration of CBs in pre-genesis stage of developing disturbances is about one-hour longer in 95% confidence level (Figure 8Figure 6a, Table 3). Likewise, the duration of CBs in post-genesis stage of developing disturbances is again about one-hour longer in 95% confidence level. The standard deviation of duration is the same for non-developing and pre-genesis developing disturbances, while it is smaller for post-genesis developing disturbances. As the mean value of three groups (non-developing and pre-genesis developing and post-genesis developing disturbances) vary, the coefficient of variation is also calculated for even comparison. Note that the coefficient of variation is the ratio of the standard deviation to the mean. The coefficient of variation of duration is also the same between non-developing and pre-genesis developing disturbances, while it is smaller for post-genesis developing disturbances. That is, the duration of CB becomes more regular in diurnal on post-genesis stages, accompanying increases in convection for about 11.6 hours and rest period on the remaining 12.4 hours, when compared to pre-genesis stage or to non-developing samples (Table 3).

The mean of expanded deep convection area is 28,000 km^2 for non-developing disturbances, and it is 50% larger for pre-genesis developing disturbances (i.e., 42,000 km^2, Figure 8Figure 6b, Table 3). Similarly, the mean of expanded deep

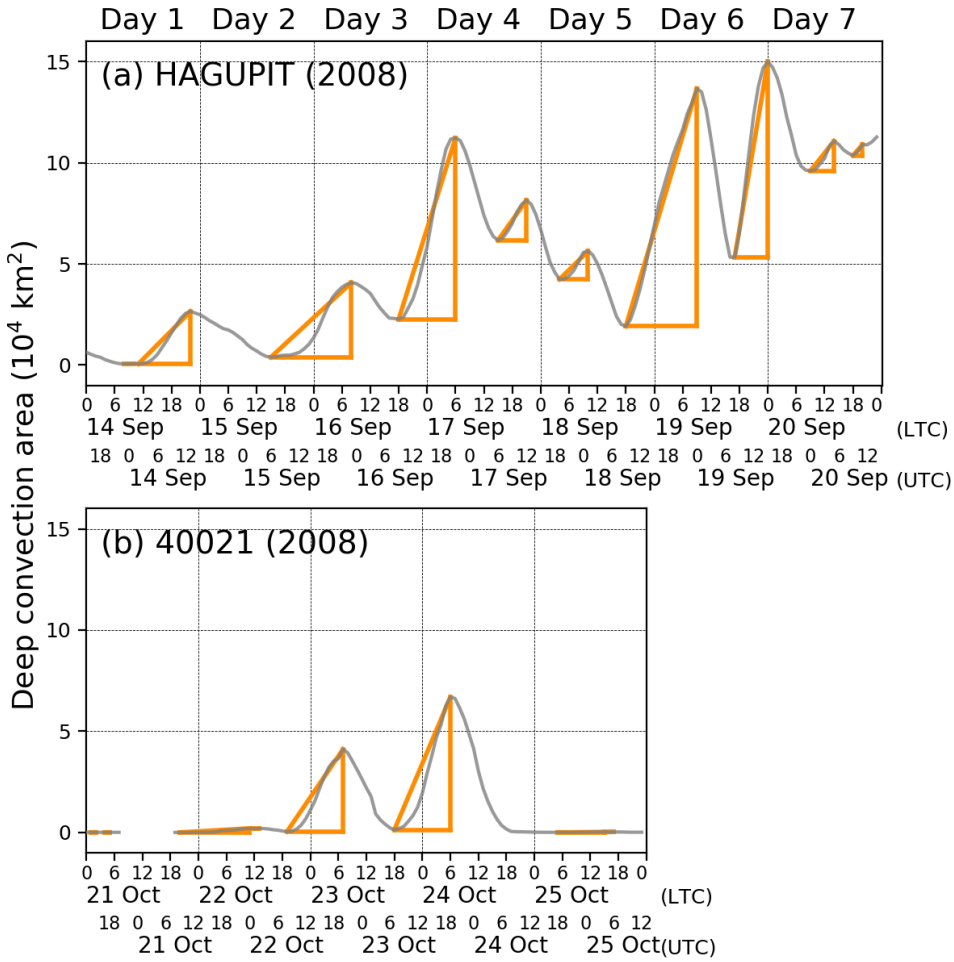

Figure 7. IR minus WV BTs time series (gray) of (a) Hagupit (2008) and (b) non-developing disturbance '40021' (2008) and all detected CBs (orange).

convection area for post-genesis developing disturbances is also about 50% larger (i.e., 64,000 km^2) as it is for pre-genesis developing disturbances. The differences are in 99% confidence level. Larger value of expanded deep convection area indicate more active deep convection within the disturbance. As the mean value varies among three groups, the group with larger mean value present larger standard deviation. When the standard deviation is normalized into coefficient variation, the measure order reverses. The coefficient variation of non-developing disturbance group is the largest, while that of post-genesis stages is the smallest. That is, diurnal expansion of deep convection area also become more regular in its magnitude when the system is developing disturbance, especially in post-genesis stage.

The relationship among the statistics of maximum deep convection area (Figure 6c, Table 3) is also similar with that of expanded deep convection area. The mean of maximum deep convection area is the smallest for non-developing disturbances (38,000 km^2), and it is 50% larger for pre-genesis stages (57,000 km^2). Similarly, it is about 80% larger for post-genesis stage (104,000 km^2) compared to the pre-genesis stage. That is, the maximum reach of deep convection area is larger for pre-genesis developing disturbances than non-developing disturbances, and after TC genesis, the maximum reach becomes even larger, which is true in 99% confidence level. For the standard deviations, a larger value is found when the mean value is larger. For the coefficient variation, that of non-developing disturbance group is the largest, while that of post-genesis stages is the smallest. That is, the maximum reach of diurnal expansion of deep convection area is the larger and is distributed narrower

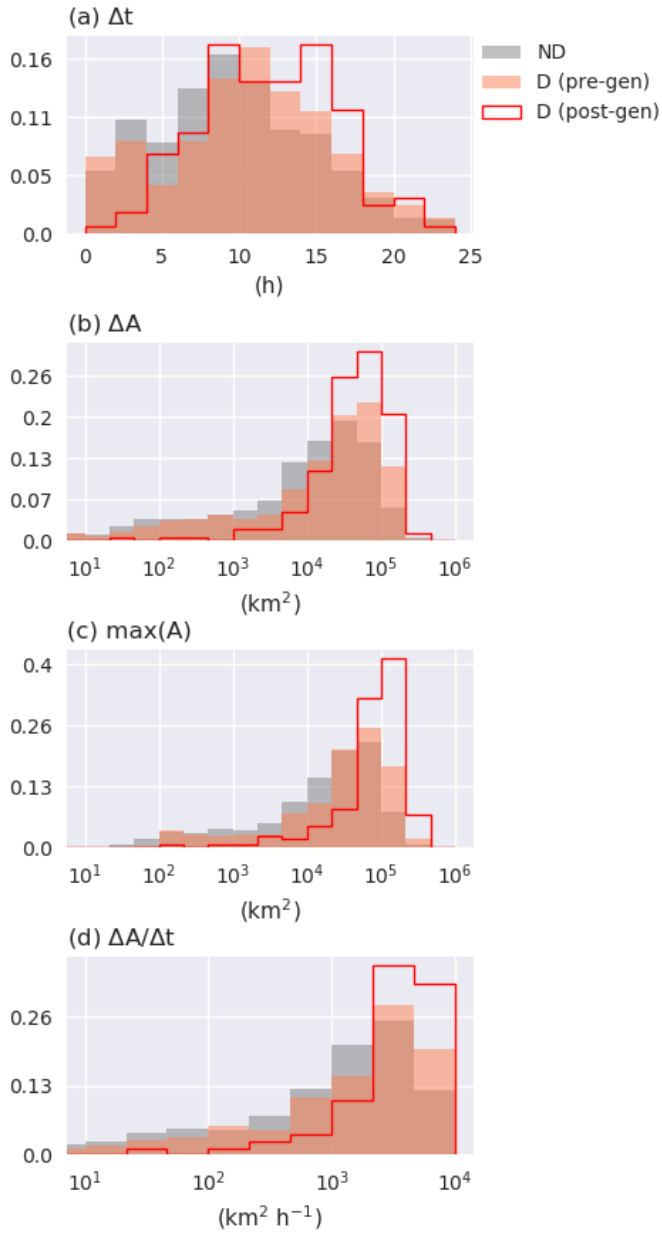

Figure 8. Probability density function of the CB (a) duration (Δt), (b) expanded deep convection area (ΔA), (c) maximum deep convection area (max(A)) and (d) expanding rate (ΔA/Δt) based on the definition of the indices in Figure 6. Grey bars, red bars and red solid line indicate the distribution of non-developing (ND), developing (D) pre-genesis and post-genesis disturbances, respectively.

for developing disturbances, and especially in post-genesis stage.

The mean expanding rate of convection area is the smallest for non-developing disturbances (2,300 $km^2\ h^{-1}$), and it is about 60% larger for pre-genesis stages (3,600 $km^2\ h^{-1}$). Similarly, it is about 40% larger for post-genesis stage (5,200 $km^2\ h^{-1}$) compared to the pre-genesis stage. Larger values of expanding rate may imply occurrence of more explosive convective bursts for developing disturbances, and especially in post-genesis stage, which is true in 99% confidence level. For the standard deviations, the largest (smallest) value is found in pre-genesis (post-genesis) stage of developing disturbances. It is the same for the coefficient variation. This might imply that the expanding rate of pre-genesis stage is the most irregular, which is not found in post-genesis stage.

Overall, the four CB features from developing disturbances at pre-genesis stage tend to be more concentrated at larger values compared to non-developing disturbances, and at post-genesis stage compared to pre-genesis stage. This may possibly related with differences in the system-scale vortex and humidity in then environment, which may affect the diurnal variation of deep convection area (Gray and Jac**o**bson 1977; Mapes and Houze 1993).

Whereas previous analysis shows the general differences between non-developing and developing disturbances, further investigation shows the daily evolution of CB features Figure 9. The sample size of CB features in developing disturbances from Day 1 to 7 is 52, 68, 73, 74, 75, 79 and 73, respectively. The sample size of CB features in non-developing disturbances from Day 1 to 5 is 247,

Table 3. Statistics of the CB (a) duration (Δt), (b) expanded deep convection area (ΔA), (c) maximum deep convection area (max(A)) and (d) expanding rate (ΔA/Δt) of non-developing, developing pre-genesis and post-genesis disturbances. The units are given in the left most column. The single and double asterisks note the 95% and 99% significant difference of the value, respectively, when compared with that of pre-genesis developing disturbances.

		Non-developing disturbances	Developing disturbances (pre-genesis)	Developing disturbances (post-genesis)
Δt (h)	**Mean**	9.6*	10.5	11.6*
	Standard deviation	5.9	5.9	4.6
	Coefficient variation	0.6	0.6	0.4
ΔA (10^4 km^2)	**Mean**	2.8**	4.2	6.4**
	Standard deviation	3.9	4.5	5.2
	Coefficient variation	1.3	1.1	0.8
max(A) (10^4 km^2)	**Mean**	3.8**	5.7	10.4**
	Standard deviation	4.5	5.7	7.0
	Coefficient variation	1.2	1.0	0.7
ΔA/Δt (10^3 km^2 h^{-1})	**Mean**	2.3**	3.6	5.2**
	Standard deviation	2.9	6.5	3.5
	Coefficient variation	1.2	1.8	0.7

349, 348, 373 and 344, respectively.

The duration of CB is distributed in small values on Day 1 for both developing and non-developing disturbances (Figure 9a). For developing disturbances, the distribution of CB duration on Day 2 to 7 are almost consistent, without any noticeable temporal evolution. For non-developing disturbances, the distribution CB duration tend to shift to larger values as the Day goes on, and the distribution shifts to lower value on Day 5. The duration of non-developing disturbances on Day 2, 3 and 5 are distributed in smaller range compared to that of developing disturbances with 95% confidence level on Day 2 and with 99% confidence level on Day 5. On Day 4, however, CB duration for non-developing disturbances is larger than that for developing disturbances in 99% confidence level. In terms of disturbance evolution, however, the CB duration is rather similar for the most of the days except for Day 1 and non-developing samples in Day 5, and it is quite difficult to catch temporal evolution.

For the expanded deep convection area, distributions on Day 1 are concentrated in small values (Figure 9b). For developing disturbances, the expanded deep convection area on Day 2, 3 and 4 are similar with each other, but larger than that on Day 1. Likewise, for developing disturbances, the expanded deep convection area on Day 5, 6 and 7 are similar with each other, but larger than that on Day 2, 3, and 4. For non-developing disturbances, the expanded deep convection area on Day 2, 3 and 5 are lower than developing disturbances, which of Day 3 and 5 are even significant at 99% confidence level. Only the expanded deep convection area on Day

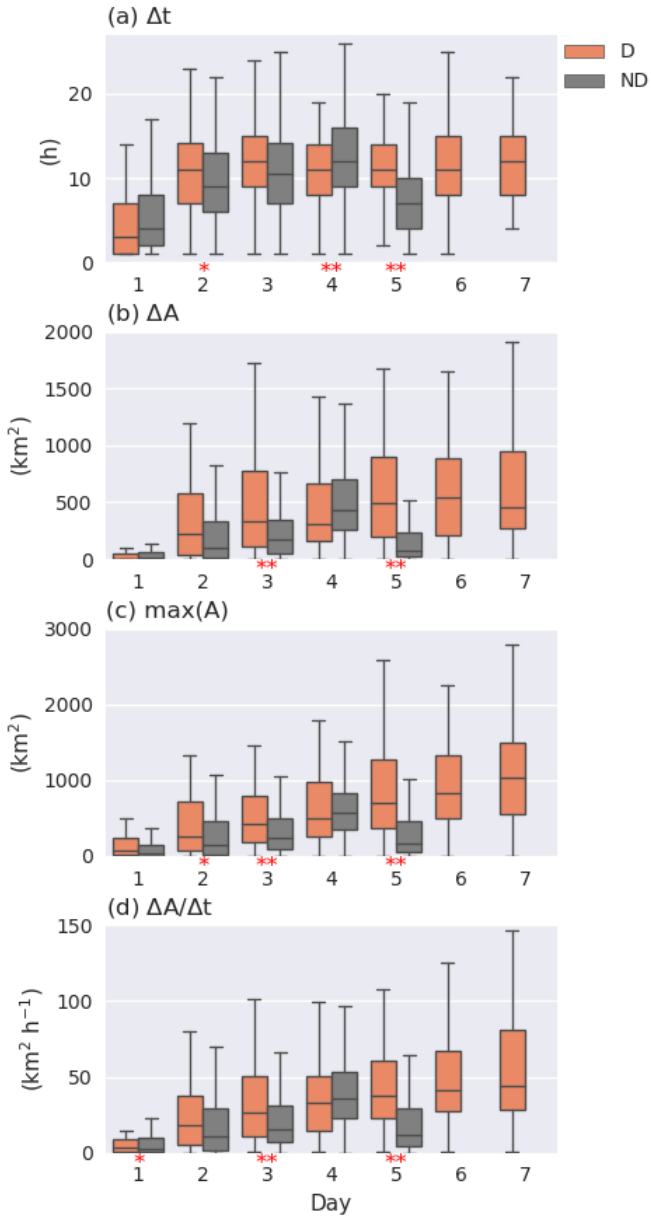

Figure 9. Daily boxplots of the CB (a) duration (Δt), (b) expanded deep convection area (ΔA), (c) maximum deep convection area (max(A)) and (d) expanding rate (ΔA/Δt). The single and double asterisks note the 95% and 99% significant difference of the value, respectively, when compared between non-developing (ND) and developing (D) disturbances on each day from Day 1 to 5.

4 of non-developing disturbances is comparable to that of developing disturbances. When reminding that the day with the largest CB (a day with largest expanded convection area) was set to Day 4 for non-developing disturbances, current result is quite reasonable. Besides, this result also suggests that non-developing disturbances likely accompany a single large CB on Day 4, whereas the CBs in the remaining days are not quite significant. In this regard, the non-developing disturbances are further screened in section 3.1.3.

The maximum deep convection area of developing disturbances shows clear increasing trend in its distribution from Day 1 to 7 (Figure 9c). In other words, maximum reaches of deep convection area gradually increase as TC genesis time approaches. Likewise, that of non-developing disturbances shows increasing trend in its distribution from Day 1 to 4, which suddenly decreases on Day 5, as the disturbance decays. Whereas the distribution on Day 4 of non-developing disturbances are comparable to that of developing disturbances, that on Day 2, 3, and 5 are significantly smaller than that of developing disturbances in 95%, 99%, and 99% confidence levels, respectively. This characteristic may also be closely related with the distribution characteristic in the expanded deep convection area.

The expanding rate of convection area for developing disturbances also show increasing trend in its distribution from Day 1 to 7 (Figure 9d). This is quite reasonable because the duration remains the same (Figure 9a) when the expanded deep convection area tends to increase in time (Figure 9b). This may infer that the deep CB tends to be faster when TC genesis time approaches. Likewise, that of non-

developing disturbances shows increasing trend in its distribution from Day 1 to 4 and decreases on Day 5. The distribution on Day 1, 3, and 5 are significantly smaller than that of developing disturbances in 95%, 99%, and 99% confidence levels, respectively.

Further investigation on the daily distribution of each CB features solidifies the previous understanding on the CB distributions on rough classification. More prominent deep convection is accompanied when the system is more likely to develop into a TC, as the system is expected to be more organized (Gray and Jacobson 1977; Mapes and Houze 1993).

3.1.2. Definition of CB and mCB

As discussed in the previous section, the non-developing disturbances tend to have smaller values of CB features compared with developing disturbances. Also, many of non-developing disturbances likely to have one single major CB on Day 4, rather than a sequence of major CBs on continuous days, according to Figure 9. Therefore, this study further focuses on the "mCB" with sufficient magnitude, which would exclude weak convection from all the selected CB events. In order to screen small scale CBs, which are considered less effective in the system-scale intensification via latent heat release or inducing secondary circulation, arbitrary thresholds are needed.

To objectively determine the thresholds, KSS is employed and total 124 numbers of threshold combinations for durations (ranging 1–12 h with 1 h

increment), expanded deep convection area and maximum deep convection area (ranging 0–60,000 km^2 with 5,000 km^2 increment), and expanding rate (ranging 0–6,000 $km^2\ h^{-1}$ with 500 $km^2\ h^{-1}$ increment) are examined. KSS shows the largest value (0.54) when the combination of all four variables—duration, expended convection area, maximum convection area, expanding rate—are equal to 6 h, 5,000 km^2, 15,000 km^2, 500 $km^2\ h^{-1}$, respectively.

By applying this threshold, hereafter, this study defines CB as convection area increment satisfying four thresholds ($\Delta t \geq 6$ h, $\Delta A \geq 5{,}000$ km^2, $\max(A) \geq 15{,}000$ km^2, and $\Delta A/\Delta t \geq 500$ $km^2\ h^{-1}$). If CBs occur for at least two consecutive days, it is then defined as mCB. As described above, mCB can be understood as an observational evidence of gradual convective organization for tropical disturbance. Depending on the occurrence of it, developing and non-developing disturbances will be categorized into four subcategories in the following section.

In terms of physical scale, 6 h CB duration seems sufficient amount to capture diurnal variation. Expanded convection area of 5,000 km^2 corresponds to the range of meso-beta scales (20–200 km diameter; dimension of mesoscale convective complexes or large thunderstorms; Orlanski 1975). Similarly, maximum convection area of 15,000 km^2 corresponds to the range of the meso-beta scale. To interpret physically, our CB definition implies that convective growth of mesoscale convective complexes or large thunderstorm size continued for more than 6 h may be associated with TC genesis.

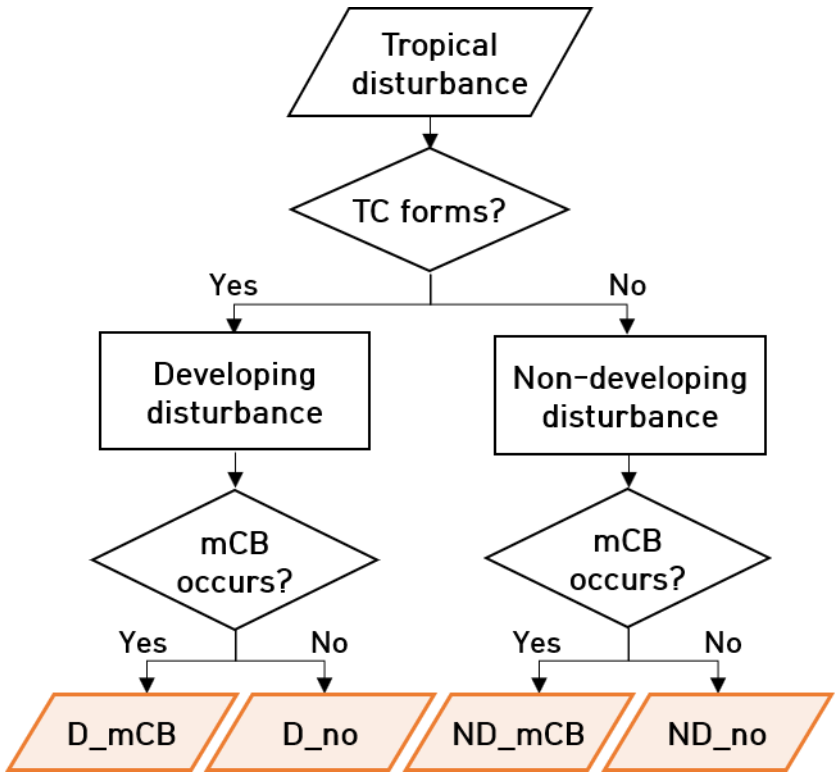

Figure 10. Flow chart of tropical disturbance categorization into four groups (D_mCB, D_no, ND_mCB, and ND_no).

Table 4. 2 × 2 contingency table of developing and non-developing disturbances with and without mCB having optimal KSS value.

	Developing disturbance	**Non-developing disturbance**	**Total**
With mCB	54	53	107
Without mCB	26	330	356
Total	80	383	

3.1.3. Categorization of tropical cyclogenesis

Considering the existence of a mCB during the pre-genesis stage of developing disturbances, and throughout the life cycle of non-developing disturbances, the total 463 (= 80 + 383) disturbances were classified into four groups (Figure 10): developing disturbances with mCB (D_mCB) and without mCB (D_no), and non-developing disturbances with mCB (ND_mCB) and without mCB (ND_no). As shown in Table 4, the majority (67.5%) of TC genesis cases occur after a series of CBs events (D_mCB), while most (86.2%) of non-developing disturbances evolves without mCB (ND_no). A small ratio (13.8%) of non-developing disturbances occur with mCB, but do not develop finally (ND_mCB). And some TCs can develop without mCB, but the considered fraction (32.5%) is relatively low (D_no). Calculated statistical values show 67.5% of hit rate (or probability of detection; A/(A+C) in Table 2), 13.8% of false alarm rate (B/(B+D) in Table 2), and 50.5% of success ratio (A/(A+B) in Table 2). Therefore, it can be expected that there is 50.5% chance that it may develop into TC when arbitrary disturbance exhibits mCB. Further discussion is provided in section 4.1 in terms of the role of mCB as tropical cyclogenesis precursor.

Table 5 presents the list of TC cases which are classified as D_mCB and D_no. In Figure 11, the daily snapshot of the developing and non-developing disturbances of each category. The time of each snapshot is 0000 LTC, because deep moist convection peaks in the nighttime over tropical ocean (Gray and Jacobson 1977; Melhauser and Zhang 2014). The deep convection area of Hagupit (2008) is

Table 5. List of TC cases classified as group D_mCB and D_no.

	D_mCB		D_no
2007	YUTU TORAJI 06W-NONAME PABUK WUTIP SEPAT DANAS NARI WIPHA	FRANCISCO LEKIMA KAJIKI FAXAI TAPAH HAGIBIS MITAG 25W-NONAME 26W-NONAME	KONG-REY MAN-YI USAGI FITOW 14W-NONAME KROSA PEIPAH
2008	01W-NONAME HALONG NAKRI KALMAEGI FUNG-WONG KAMMURI VONGFONG 14W-NONAME SINLAKU HAGUPIT MEKKHALA HIGOS 22W-NONAME MAYSAK		NEOGURI RAMMASUN MATMO FENGSHEN 1W-NONAME NURI 16W-NONAME 17W-NONAME JANGMI BAVI HAISHEN NOUL DOLPHIN
2009	KUJIRA CHAN-HOM LINFA SOUDELOR 06W-NONAME MOLAVE GONI MORAKOT ETAU VAMCO KROVANH	DUJUAN CHOI-WAN KETSANA 18W-NONAME PARMA MELOR MIRINAE 25W-NONAME NIDA 27W-NONAME 28W-NONAME	NANGKA MUJIGAE KOPPU NEPARTAK LUPIT 24W-NONAME

noticeable every day on Day 1 to 7, and its area increases with time. For the case of Bavi (2008), however, the deep convection area is not noticeable on its pre-genesis stage, but only visible on post-genesis stage, i.e., Day 6 and 7. When comparing Hagupit and Bavi, the deep convection initiates earlier and organizes more gradually for D_mCB, whereas the deep convection is less evident in pre-genesis stage and develops rapidly with TC genesis for D_no. For the non-developing disturbances, the deep convection area of "39309" (2008) is noticeable on Day 3 and 4 but decays on Day 5. In terms of deep convection decay on Day 5, after mCB on Day 3 and 4, further investigation would be needed, especially by comparing with D_mCB. For the case of "39917" (2008), deep convection is shown at the periphery of red circle on Day 2, and near the vort-max position on Day 4.

To examine the temporal evolution of deep convection of each category, the composite time series of deep convection area (IR minus WV BTs < 0 area) for the four classified groups are investigated (Figure 12). First, the majority (67.5%) of developing disturbances analyzed in this study (D_mCB; Figure 12a) shows diurnally repeated convection, consistent with many previous reports (Zehr 1992; Davis and Ahijevych 2012; Zawislak and Zipser 2014a). D_mCB shows a prominent diurnal convective evolution before and after TC formation. However, relatively suppressed convection within two days prior to TC genesis (Zehr 1992) is not captured in the present composites of the evolution of convection (Figure 12). Rather, the convective bursts are stably maintained until TC formation. The mismatch may be due to different TC samples or result of composite analysis. While the daily

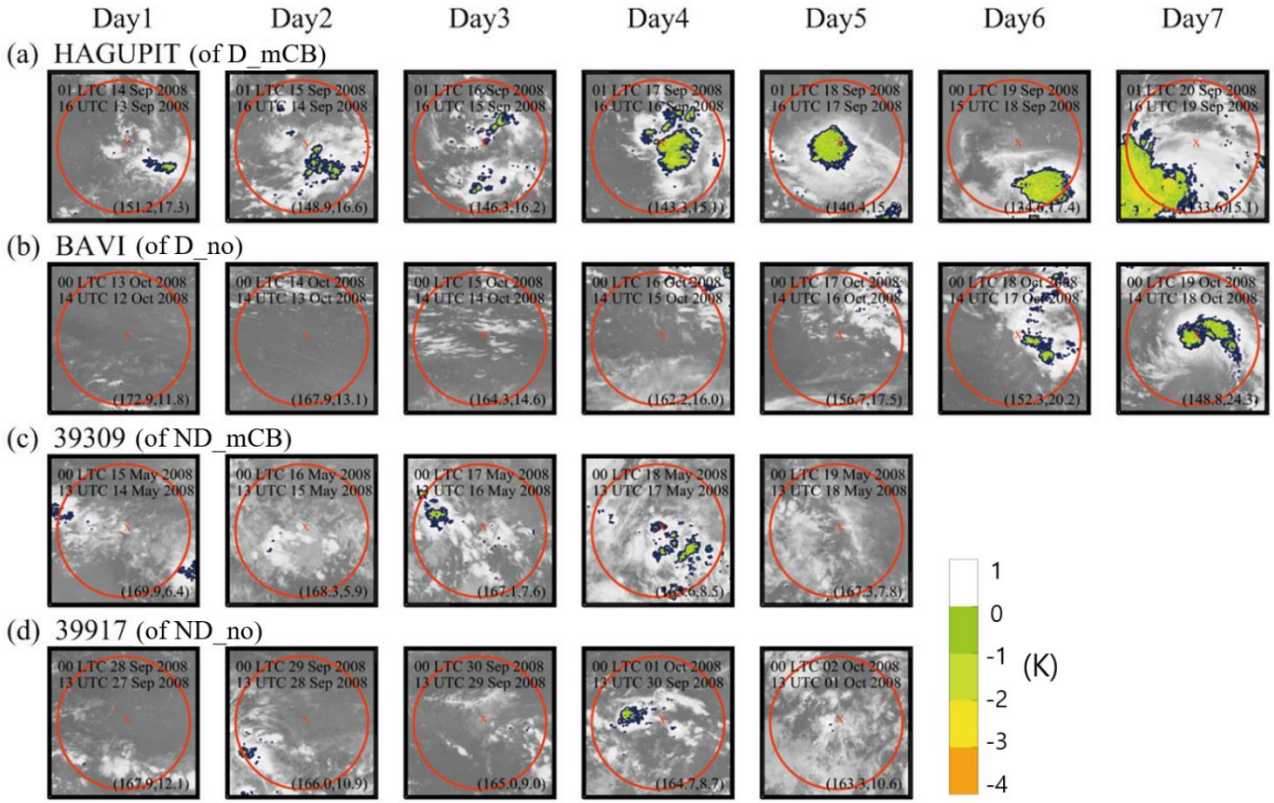

Figure 11. The daily snapshot of IR minus WV image of the sample case in each category: (a) Hagupit of D_mCB, (b) Bavi of D_no, (c) 39309 of ND_mCB, and (d) 39917 of ND_no. The red circle indicates 500-km radius circle centered at the vort-max position (the red 'x' with its coordinate introduced in the bottom right corner).

maximum convection area appears to increase, statistical verification shows that daily increase is not significant at the 90% confidence level; this is consistent with the precipitation analysis by Zawislak and Zipser (2014a).

While multiple episodes of deep CBs occur prior to most TC formation (D_mCB), some (32.5%) disturbances develop into TCs without successive convection (D_no; Figure 12b). Deep convection for D_no tends to be overall suppressed throughout the pre-genesis period but increases several hours prior to the formation day, and becomes more persistent through the diurnal cycle. Following this, a sharp increase in the maximum convection area from the formation day (Day 6) to the next morning (Day 7) is visible, which is entirely different as compared to D_mCB with similar daily convective maxima in the two post-genesis days (Days 6 and 7).

In 13.8% of non-developers (ND_mCB; Figure 12c), a prominent mCB similar to D_mCB is observed. Compared with D_mCB, ND_mCB shows similar diurnal enlargements as D_mCB until Day 4 (the day with maximum convection area), but decreases on Day 5. A statistical comparison of IR minus WV BTs < 0 area values between D_mCB and ND_mCB showed that convection areas on Day 1 to Day 4 are not significantly different from each other at the 95% confidence level (e.g., daily mean value on Day 4 is 5.8×10^4 km for D_mCB and 5.4×10^4 km for ND_mCB). The maximum convection area on the day of TC formation (9.6×10^4 km^2; Day 6) is statistically larger compared with the daily maximum of both non-developing disturbances (7.0×10^4 km^2; ND_mCB) and developing disturbances (5.8×10^4 km^2;

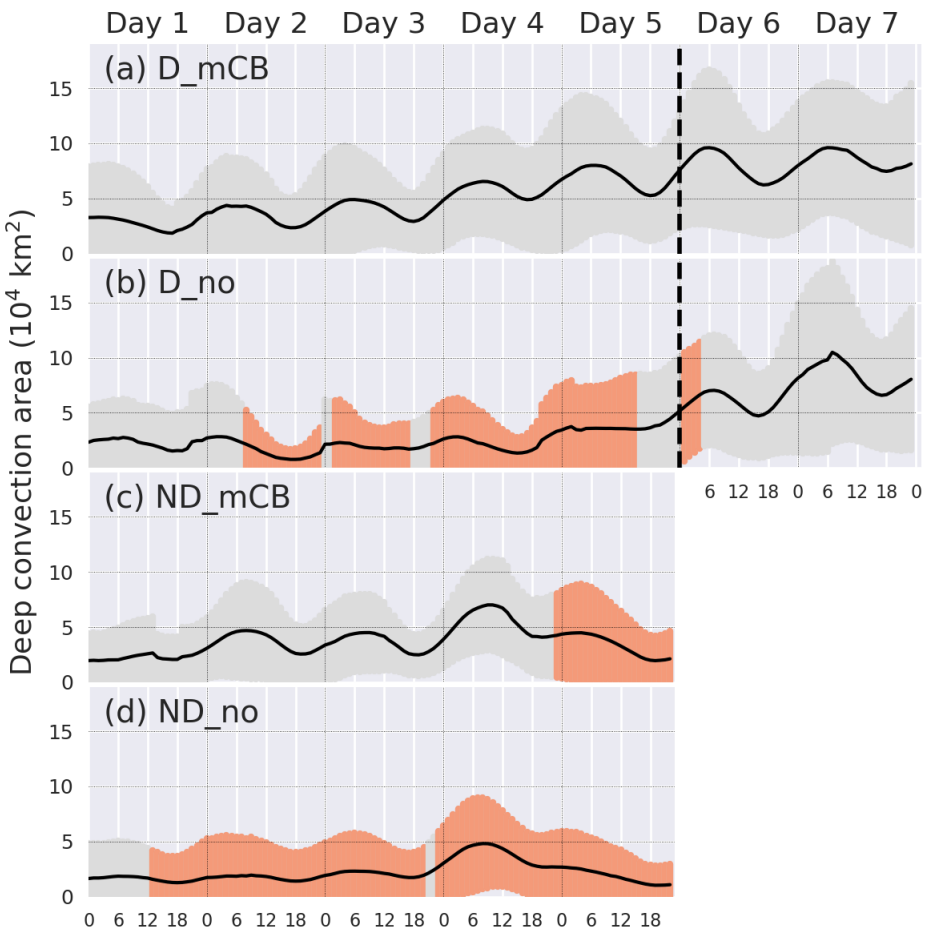

Figure 12. Composite time series of the average (thick solid line) of the deep convection area (that is, IR minus WV BTs < 0 area) with 1.0 standard deviation whiskers (gray and orange) for (a) D_mCB, (b) D_no, (c) ND_mCB, and (d) ND_no. Significantly difference in 95% confidence level between D_mCB and D_no is noted in (b) with orange whiskers, that between D_mCB and ND_mCB is noted in (c), and that between ND_mCB and ND_no is noted in (d). Think black dashed line indicates TC formation.

D_mCB) on Day 4. This significant difference in the convection area is not recognizable until the day of TC formation (Day 6), which confirms the challenges in the forecast of TC formation based on convective signal alone as did in Park et al. (2015).

Most (86.2%) of non-developing disturbances are classified as not having multiple episodes of CBs (ND_no; Figure 12d). That is, most non-developing disturbances are featured with a single CB on Day 4 which satisfies CB thresholds introduced in section 3.1.2, as expected. Non-developing disturbances with less prominent convective activity compared to developing disturbances are also consistent with the results of Zawislak and Zipser (2014a).

Therefore, multiple episodes of CBs prior to TC genesis are common (D_mCB), but the occurrence of mCB is not sufficient for the determination of TC genesis. As a series of CBs also occurs in some of non-developing tropical disturbances (ND_mCB), mCB occurrences represent about 50.5% chance for developing into a TC.

As the composite time series shows clear diurnal cycle of deep convection area, the time distribution of the diurnal peaks is further investigated (Figure 13). For D_mCB, deep convection area reaches its peak the most in the morning, except for Day 1, either in 0000–0500 LTC and in 0600–1100 LTC. For D_no, the early morning peak is not frequently observed on Day 1 and 2. From Day 3, the maximum frequency occurs in the early morning either in 0000–0500 LTC and in 0600–1100 LTC. For ND_mCB, the maximum frequency also occurs in the morning (except for

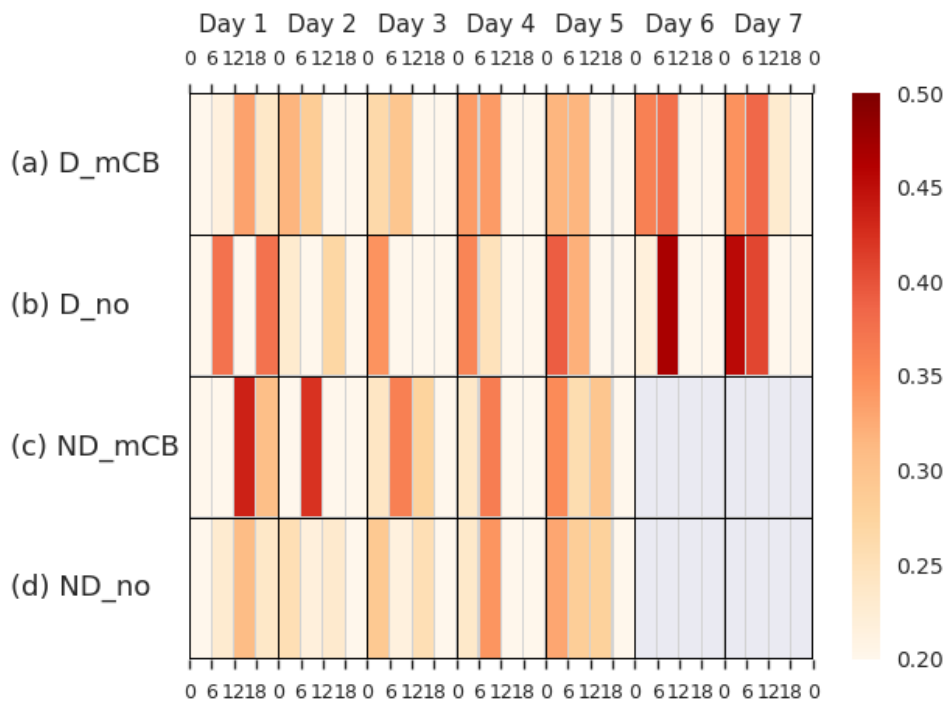

Figure 13. The frequency distribution of the local time (LTC) when the deep convection area reaches its peak. The frequency is calculated in six-hourly bins, and the summation of each black-lined box is equal to 1.

Day 1), but with still large frqeuncy observed in 1200–1700 LTC on Day 3 and 5. For ND_no, the frequency is broadly distributed in all time bins on Day 1, 2, 3, and 5, but the morning peak is found on Day 4. As it is widely known that the oceanic convection tends to peak in the early morning, i.e., around 0600 local time (Gray and Jacobson 1977; Davis and Ahijevych 2012), overall distribution is reasonable. However, when comparing the frequency distribution difference between developing and non-developing disturbances, that developing disturbances tend to have more consistent early morning peaks in 0000–1100 LTC, while the non-developing disturbances tend to have more broad distribution. This may possibly be associated with the strength of disturbance vorticity or environmental moisture, which will require further analysis.

Regarding the overall differences in deep convection characteristics between D_mCB and D_no, it may be associated with multiscale environmental conditions. Before examining the environmental components, the temporal and spatial distributions of TC genesis among D_mCB and D_no is explored. The monthly distribution of both among D_mCB and D_no (Figure 14a) show the highest genesis frequency in September and the lowest genesis frequency in boreal winter (December to February). The TC genesis latitudinal distributions are also similar between D_mCB and D_no (Figure 14b), as the distribution is the highest in 5°N–15°N and the lowest in 20°N–25°N ranges. The TC genesis longitudinal distribution, however, shows slightly different peaks between D_mCB and D_no (Figure 14c). For D_mCB, TC genesis is the most frequent in 120°E–140°E. However, for D_no,

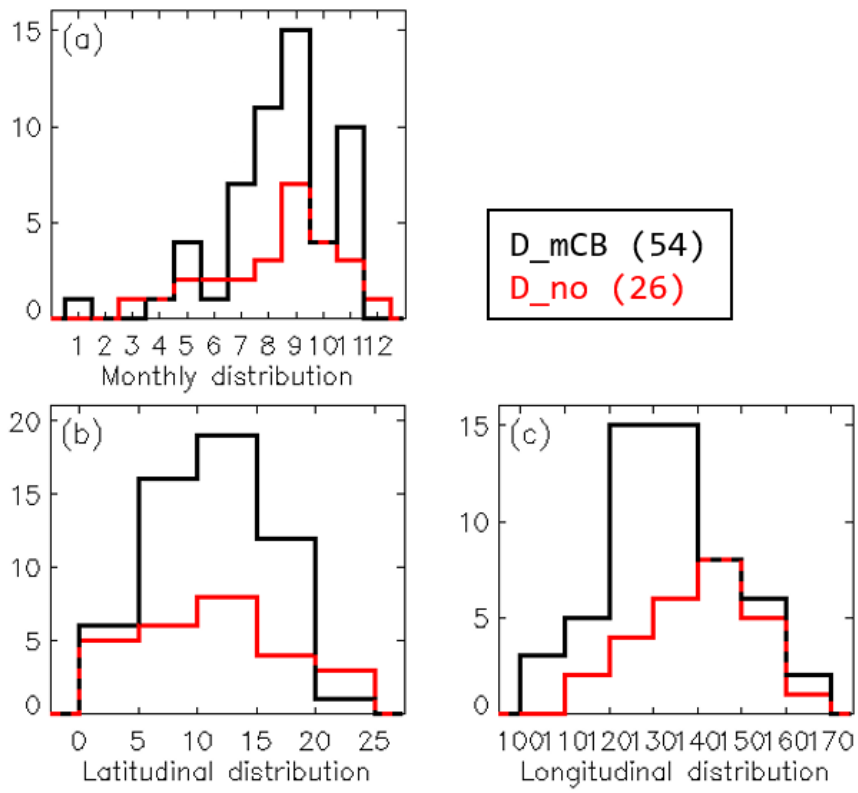

Figure 14. Histogram of (a) monthly, (b) latitudinal, and (c) longitudinal distribution of D_mCB (black; 54 cases) and D_no (red; 26 cases).

TC genesis is the most frequent in 140°E–150°E, which is slightly skewed to the central Pacific compared to D_mCB.

The spatial distribution of TC genesis is shown, divided by four seasons (Figure 15). As already seen in Figure 14b, there is no clear differences in latitudinal distribution between D_mCB and D_no in all seasons. When focusing on the longitudinal distribution, in December-February, a D_mCB sample forms into TC around the Philippines, and a D_no sample forms into TC at around 165°E. Despite very low number of samples, the east-west skewness is evident. In March–May, TC genesis of both D_mCB and D_no samples occur in the east of the Philippines, but still, the D_mCB samples are more skewed to the west, when the D_no samples are more skewed to the east. Similarly, in July–August, the D_mCB samples are more skewed to the west, when the D_no samples are more skewed to the east. This skewness likely manifests the formation environment or mechanism may be different between D_mCB and D_no, but further investigation is needed. In September–November, the TC genesis distributions are not clearly discriminated between D_mCB and D_no.

So far, it is observed that the majority (67.5%) of TC genesis accompany mCB before their formation and tend to form in the western part of WNP (near the Philippines). On the contrary, the minority (32.5%) of TC genesis do not accompany mCB, but rather abruptly develop deep convection, and tend to form in the eastern part of WNP. To better understand TC genesis pathway of these two groups, the evolution of environmental conditions will be investigated in the following section.

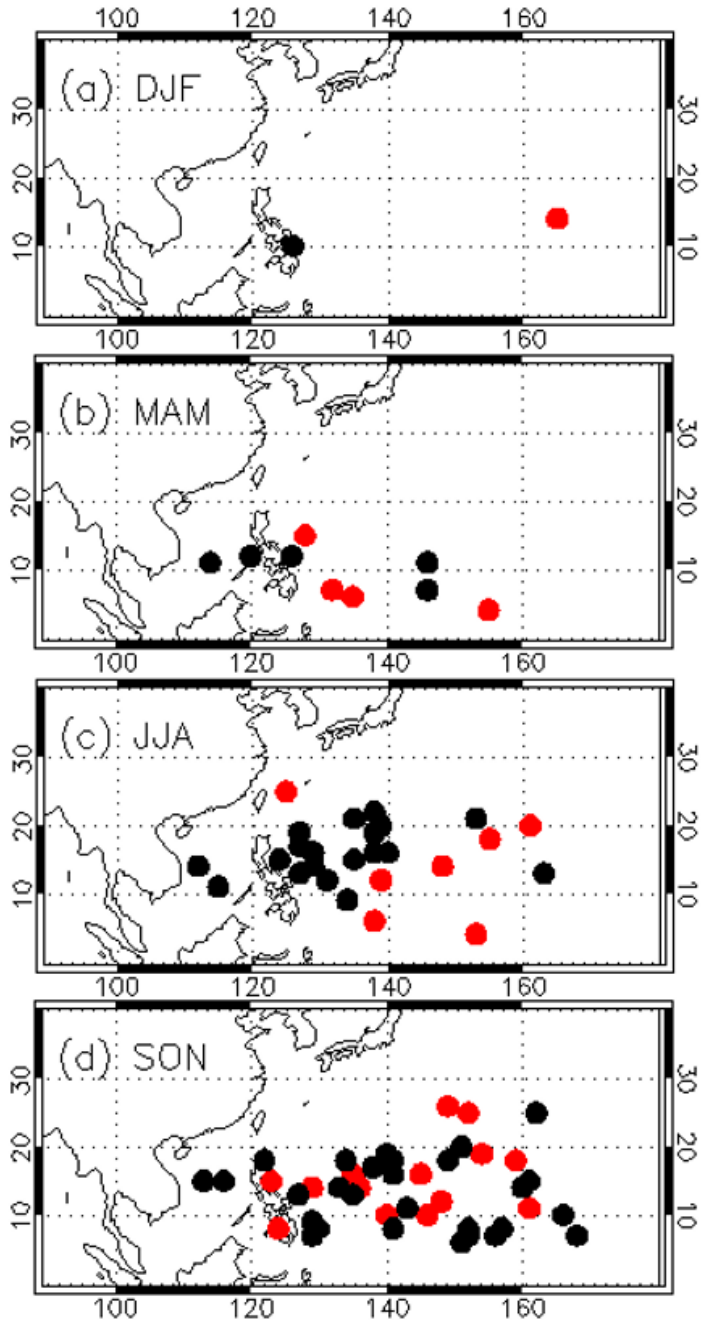

Figure 15. Spatial distribution of TC genesis location during (a) December-February (DJF), (b) March–May (MAM), (c) June–August (JJA), and (d) September–November (SON). Black (red) dots indicate genesis locations of D_mCB (D_no).

Particularly for D_mCB, the formation pathway will be explained by comparing the environmental characteristics with ND_mCB. The comparison will primarily focus on understanding why the daily convective expansion of non-developing disturbances after mCB (Figure 7c) decreases subsequently in contrast to the continuous increase observed in the convection area (Figure 7a). For D_no, the focus will be placed on understanding how TC (or deep convective clouds) can abruptly develop after the absence mCB in preceding days (Figure 7b). Especially, any large-scale factors (or forcing) that can spin-up a TC will be investigated.

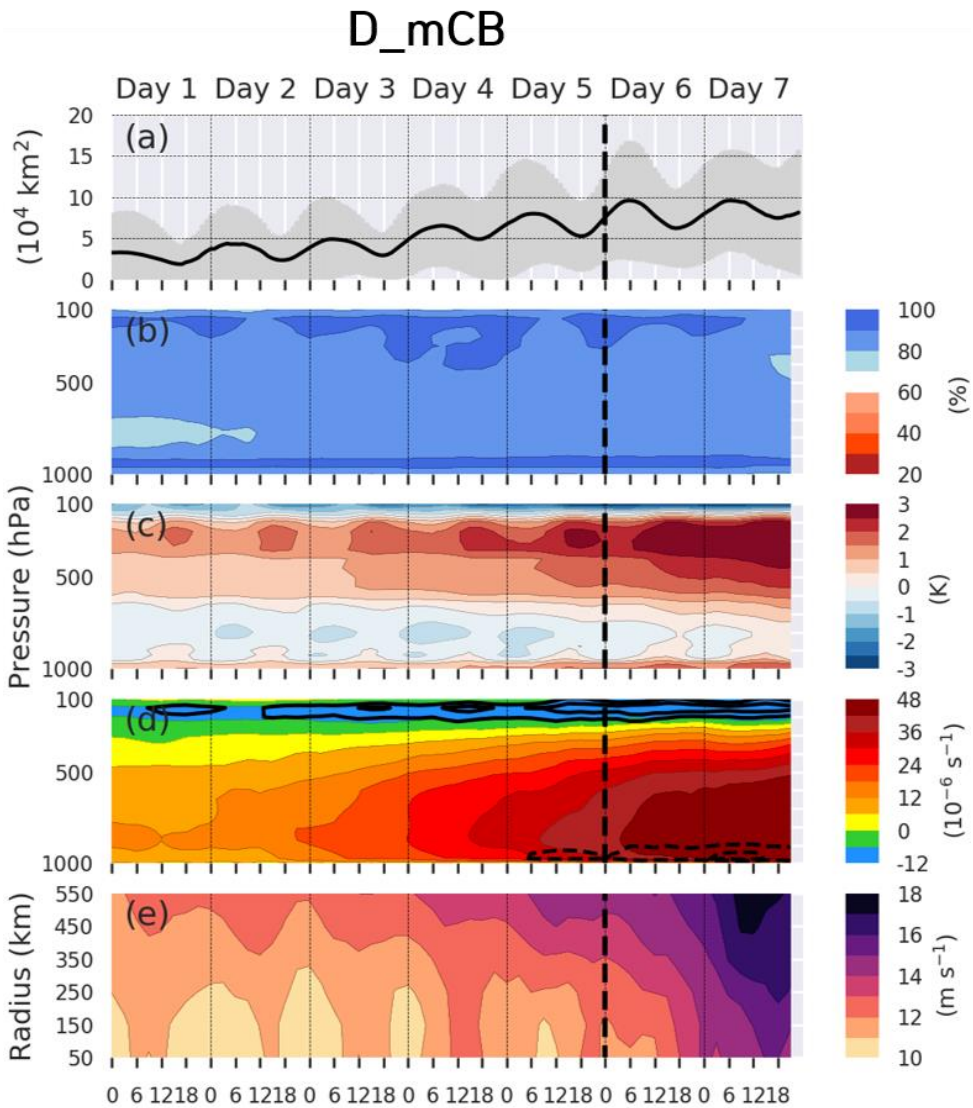

Figure 16. (a) The same as Figure 12a. (b–d) Time-pressure Hovmöller diagram of (b) composite relative humidity (%), (c) composite temperature zonal anomaly (K), and (d) composite relative vorticity (10^{-6} s^{-1}, shading) and divergence (contours at ± 10×10^{-6} s^{-1} and ± 15×10^{-6} s^{-1}) which are area-averaged within 500 km radius circle from the vort-max. (e) Time-radius Hovmöller diagram of composite vertical wind shear. The radius is the distance from the vort-max. All figures are the composite among D_mCB cases and the vertical dashed line indicates the TC genesis time.

3.2. Tropical cyclogenesis with mCB

3.2.1. Multi-scale environment analysis

Firstly, thermodynamic evolution of TC genesis with mCB is examined in view of convective-environmental evolution. Figure 16b shows the time-evolution of area-averaged relative humidity throughout the entire troposphere within 500 km radius circle around the vort-max positions. Overall, the atmospheric condition is very humid (>70%) for D_mCB which favors active convection. In particular, the mid-troposphere (600–500 hPa) remains very humid (> 80%) throughout the entire pre-genesis period. The analysis within 300 km radius and 300-to-800 km annulus consistently indicate mid-tropospheric relative humidity over 80%. Maintaining a high humidity for D_mCB is consistent with previous reports (Nolan et al. 2007; Zawislak and Zipser 2014b), who identified the near-saturation of low-to-mid-troposphere as a necessary condition for genesis. Whereas near-saturation environment revealed by Zawilak and Zipser (2014b) indicates RH over 90% within 1-degree radius around vortex center, lower RH value in current analysis (> 80%) may be due to average over larger area.

The upper-tropospheric zonal temperature anomaly shown in Figure 16c presents a formation or evolution of a warm core. In case of D_mCB, warm temperature anomaly over 1 K is continuously observed since Day 1, and the warm temperature anomaly increases as TC genesis time approaches. On one day before TC genesis (Day 5), warm temperature anomaly exceeds 2.5 K. Thus, TC genesis of

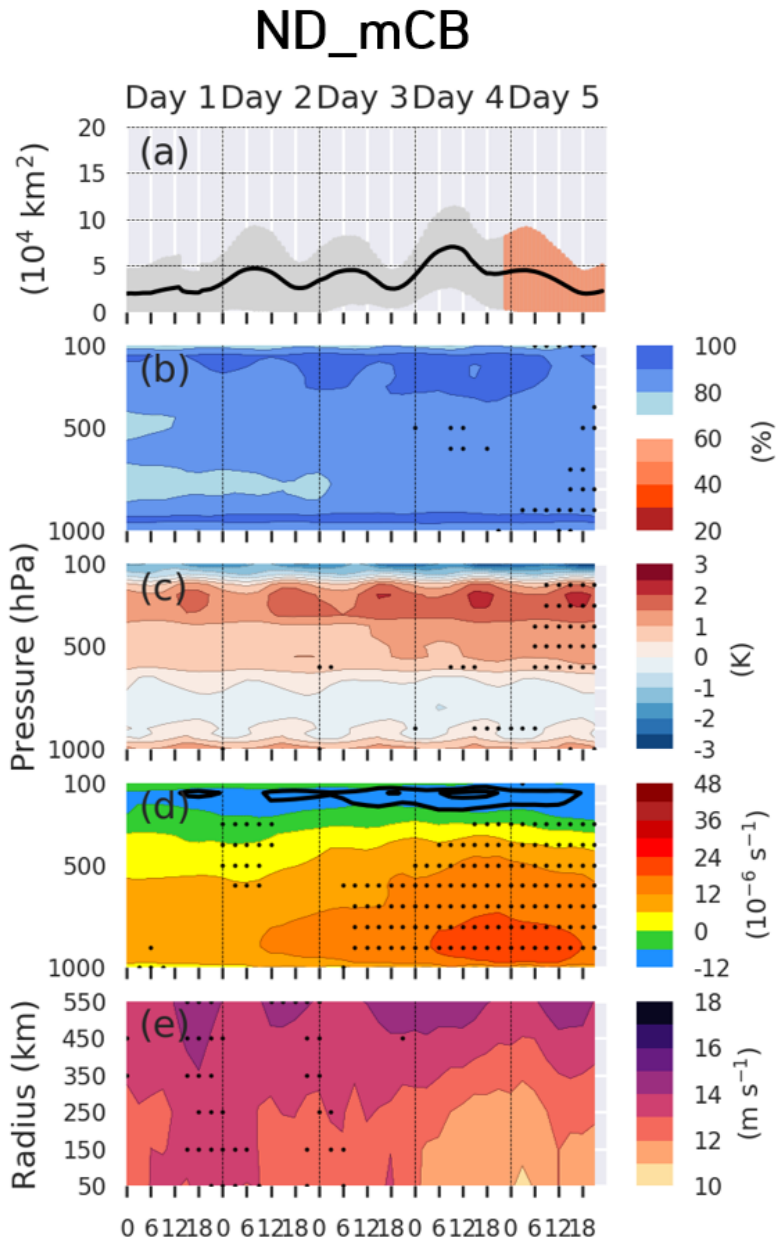

Figure 17. The same as Figure 16 but for ND_mCB. Orange whiskers in (a) and black dots in (b–e) indicate significant difference compared to D_mCB at the 95% confidence level.

group D_mCB is favored in humid thermodynamic condition and its warm-core gradually develops since several days prior to its genesis.

Figure 16d shows the time evolution of relative vorticity and divergence within 500 km radius circle from vort-max positions. Overall, from Day 1, positive relative vorticity with lower-tropospheric maximum occurs. The initially strong cyclonic vorticity ($> 12 \times 10^{-6}$ s^{-1}) in D_mCB gradually intensifies and stretches into the mid- to upper troposphere up to 300 hPa throughout pre- and post-genesis periods. Associated with the strengthening of vorticity, a system-scale secondary circulation with lower-tropospheric convergent inflow ($< -10 \times 10^{-6}$ s^{-1}) and upper-tropospheric divergent outflow ($> 10 \times 10^{-6}$ s^{-1}) is apparent. Earlier presence of upper-tropospheric divergent than that of lower-tropospheric convergence is possibly due to the strong decrease in density with height. Because of the strong decrease in density, the upper-tropospheric divergence (or upper-tropospheric outflow) must tend to be much stronger than the lower-tropospheric convergence (or lower-tropospheric inflow). Within an environment of initially strong vorticity, mCB would promote continuous vorticity strengthening, prominent secondary circulation, and eventual TC genesis, consistent with idealized numerical simulation results of Wissmeier and Smith (2011) and Wang (2014).

Vertical wind shear magnitude within 350 km radius is small (< 12 m s^{-1}) on Day 1–3 among D_mCB and the diurnal variation in magnitude is evident, which becomes lower than 11 m s^{-1} during the nighttime near the vort-max center. The vertical wind shear increases as TC genesis time approaches (Day 4–7), due to the

presence of TC-related circulation as well as large-scale wind shear. As the wind fields near TC genesis require careful interpretation, the focus is rather placed on Day 1–3, as the earlier days which would primarily indicate the large-scale wind shears. On Day 1–3. the gradual TC genesis process which initially contained stronger lower-tropospheric relative vorticity (Figure 16d), is likely favored with relatively low vertical wind shears, since vertical wind shear may inhibit vertical vorticity alignment or induce dry air entrainment, either of which can weaken the system (Gray 1968; Nolan et al. 2007; Davis and Ahijevych 2012; Park et al. 2013; Tang and Emanuel 2012; Penny et al. 2015). Thus, low vertical wind shear would enable a better organization of the deep convective cloud clusters from the earlier stage, which allows for more gradual intensification of the incipient precursor vortex into a TC.

For non-developing disturbances, very moist (> 80%) mid-tropospheric and moist (> 70%) entire troposphere is observed from Day 1 (Figure 17b). Relative humidity environment of ND_mCB is significantly analogous to D_mCB in 95% confidence level, only except for several height on Day 4 and Day 5. This is consistent with mCB evolution, as the consistent evolution bifurcates after Day 4 between D_mCB and ND_mCB (Figure 12a, c). Despite such favorable thermodynamic environment, deep convection activity among ND_mCB decays after Day 4.

The upper-tropospheric zonal temperature anomaly of ND_mCB accompanies warm temperature anomaly is apparent since Day 1 and gradually intensifies every

day (Figure 17c). The magnitude is statistically analogous to that of D_mCB, in 95% confidence level. As the deep convection activities are statistically equal between D_mCB and ND_mCB, the amount of latent heat release would also be comparable, which the warm core is subject to. Thus, the evolution of ND_mCB is not quite separated from those of D_mCB particularly in thermodynamic aspect including relative humidity, warm-core anomaly as well as deep convection activity.

Initial lower-tropospheric relative vorticity on Day 1 and 2 of ND_mCB (Figure 17c) also similar to that on the same day of D_mCB at 95% confidence level. However, the strength of relative vorticity of ND_mCB becomes significantly lower than that of D_mCB on Day 3, despite of similar magnitude of deep convection activities. For a system-scale secondary circulation, only the upper branch, i.e., upper-tropospheric divergence ($> 10 \times 10^{-6}$ s^{-1}), is evident, while the lower branch, i.e., lower-tropospheric convergence ($< -10 \times 10^{-6}$ s^{-1}) is not. Despite satisfying such moist atmospheric conditions after a series of convective bursts, ND_mCB circulations finally decay after Day 4 partly because the low-to-mid tropospheric relative vorticity is not intensified strong enough on Days 3 and 4, or due to strong vertical wind shear. This will further be discussed in the following section.

Although the initial vorticity of ND_mCB is similar to that of D_mCB (Days 1 and 2), vertical wind shear in the nighttime of Days 1 and 2 for ND_mCB (Figure 17e) is significantly stronger than that for D_mCB at the 95% confidence level. In the horizontal distribution (Figure 18), the area with strong vertical wind shear (> 14

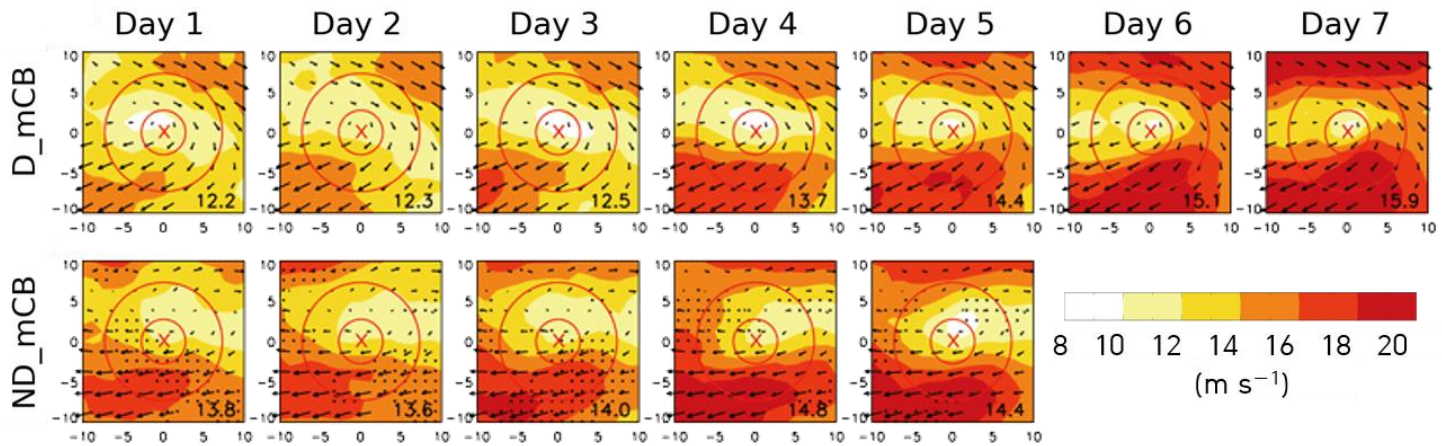

Figure 18. Composite fields of vertical wind shear (m s^{-1}) between 200 hPa and 850 hPa shown in vector (arrows) and scalar values (shading) for (a) D_mCB and (b) ND_mCB. Each panel represents 0000 LTC of each day. Two concentric red circles indicate 3-degree and 8-degree radii from the composite vort-max center (red 'x'). Black dots in (b) note significant difference between ND_mCB and D_mCB in 95% confidence level. The magnitude on the right bottom indicates the mean value of 3-to-8-degree annular area.

m s^{-1}) is much widely distributed, almost the half of 8-degree radius circle for ND_mCB on Day 1–5. For D_mCB, on the contrary, the area with strong vertical wind shear (> 14 m s^{-1}) is only located in the southwest corner within the 8-degree radius circle. The relatively strong wind shear of ND_mCB (> 13.6 m s^{-1}; Days 1 and 2) would promote unfavorable conditions for deep convection to organize and contribute to a stronger vortex, as introduced previously, in terms of vertical vorticity misalignment (Davis and Ahijevych 2012) or dry air entrainment (Penny et al. 2015).

The examination on atmospheric variables suggest that dynamic elements, such as relative vorticity and environmental vertical wind shear play the instrumental role in TC formation of D_mCB group, when compared to ND_mCB group. Therefore, dynamic elements are further investigated in different timescales.

The relative vorticity is decomposed into the disturbance-scale (2.5–9 days, Figure 19) and slowly-varying large-scale (longer than 9 days, Figure 20) vorticities. The synoptic-scale relative vorticity at 850 hPa shows a significant difference in its intensity since Day 1 within the 5-degree radius circle. This is a distinctive characteristic, when concerning the fact that the relative vorticity magnitude in Day 1 and 2 are comparable between D_mCB and ND_mCB before the scale decomposition (Figure 16d, Figure 17d). One more distinctive feature is found in synoptic-scale. On Day 1–3 of D_mCB an anticyclonic vorticity is featured in the northwest of the pre-TC disturbance. However, such feature is not apparent in the same days of ND_mCB. On Day 3 of D_mCB, the other anticyclonic vorticity emerges in the southeast of the pre-TC disturbance, which becomes very clear on

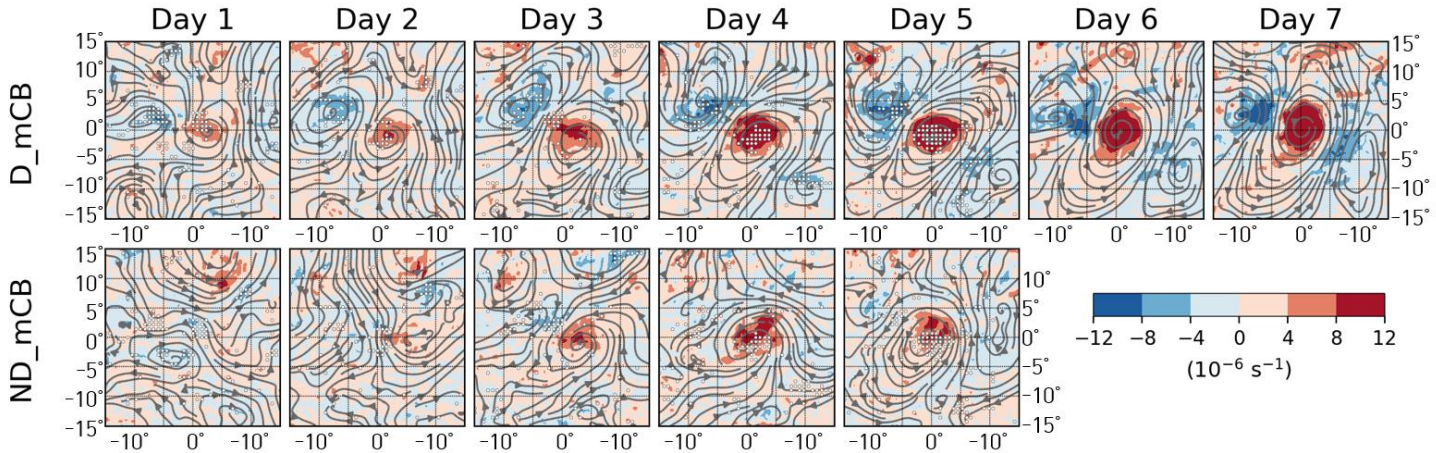

Figure 19. Composite fields of synoptic-scale (i.e., 2.5-9 days band-pass filtered) 850 hPa relative vorticity (shading, 10^{-6} s^{-1}) and horizontal wind (streamlines) of (top) D_mCB and (bottom) ND_mCB every day. The coordinate is set according to the composite vort-max center. White dots indicate significant difference between D_mCB and ND_mCB in 95% confidence level.

Day 4–7. Such a wave of anticyclone-cyclone-anticyclone of D_mCB would enhance the pressure gradient in the lower troposphere and attendant northeasterly and southwesterly around the disturbance would promote water vapor transport (Galarneau et al. 2015).

Relative vorticity in the slowly-varying environment (Figure 20) also shows differences between D_mCB and ND_mCB. Note that for slowly-varying component, there exist little change through Day 1–5 (or Day 1–7) because 9-day lowpass filter is applied. Thus, Day 3 is selected as a representation by considering the time when the strength of composite relative vorticity (Figure 16d) becomes significantly different between D_mCB and ND_mCB. On Day 3 of D_mCB, the majority of pre-TC disturbances are located in the area where slowly-varying large-scale relative vorticity both at 600 hPa and 850 hPa are high. Also, the horizontal wind streamlines converge around the majority of pre-TC disturbances. On Day 3 of ND_mCB, the majority of non-developing disturbances are also located in the area where slowly-varying large-scale relative vorticity both at 600 hPa and 850 hPa are relatively high in the WNP. But, the magnitude of slowly-varying large-scale relative vorticity of ND_mCB is much lower than that of D_mCB especially at 600 hPa. The difference between two are shown in the right most panels in Figure 20. The majority of pre-TC disturbances are located in the higher relative vorticity region, while the majority of non-developing disturbances tend to locate in the lower relative vorticity region. Also, the significance of the relative vorticity magnitude is clear at 95% confidence level.

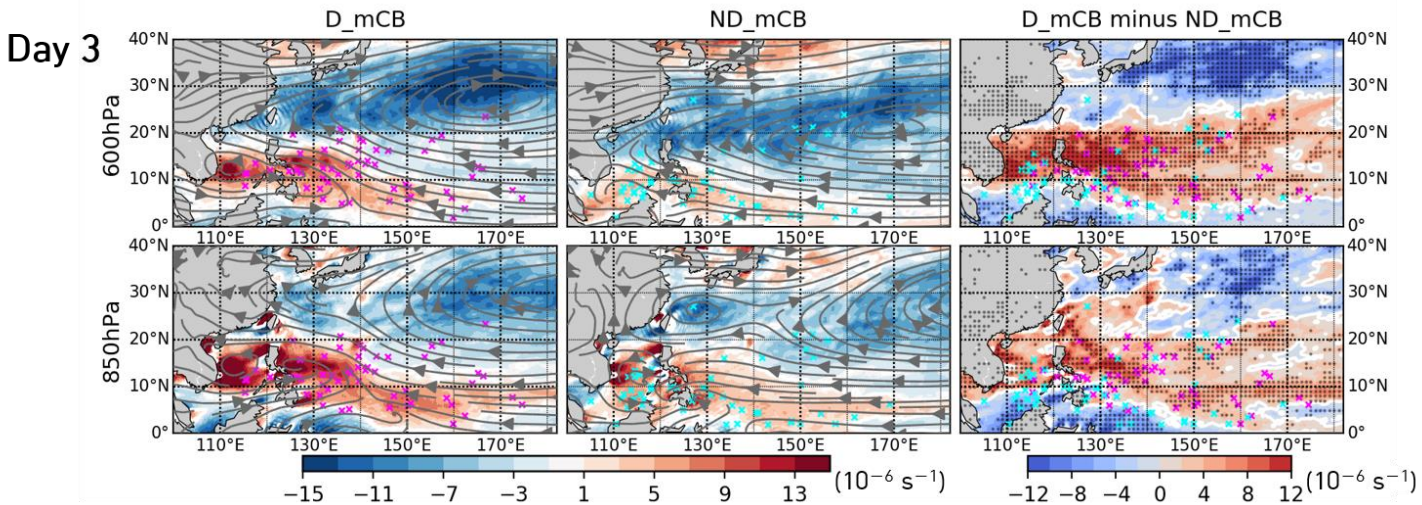

Figure 20. Composite fields of slowly-varying (i.e., 9 days low-pass filtered) relative vorticity (shading, 10^{-6} s^{-1}) and horizontal wind (streamlines) at (top) 600 hPa and (bottom) 850 hPa of (left) D_mCB, (center) ND_mCB, and (right) ND_mCB minis D_mCB on Day 3. Cyan and magenta 'x' indicate the vort-max locations of D_mCB and ND_mCB disturbances. Black dots in the right panels indicate significant difference between D_mCB and ND_mCB in 95% confidence level.

Figure 21 shows slowly-varying large-scale vertical wind shear environment of D_mCB and ND_mCB on Day 3. This time, the vertical wind shear is analyzed in three different height intervals: between 200 hPa and 850 hPa (top panels in Figure 21), 200 hPa and 600 hPa (middle panels in Figure 21), and 600 hPa and 850 hPa (bottom panels in Figure 21). When examining the vertical wind shear between 200 hPa and 850 hPa, it is found that the majority of pre-TC disturbances locate at the low-shear valley (< 12 m s^{-1}), while the majority of non-developing disturbances locate away from the low-shear valley. When separating the vertical wind shear in two different height intervals, the mid-to-upper tropospheric vertical wind shear accounts for most of the tropospheric vertical wind shear. The difference between the vertical wind shear magnitude between D_mCB and ND_mCB solidifies that pre-TC disturbances tend to distribute over favorable wind shear environment while non-developing disturbances are not. Also, the non-developing disturbances are rather concentrated at around the Philippines where the vertical wind shear is significantly high.

To summary, the composite analysis on D_mCB and its comparison with ND_mCB provided the general view of TC genesis pathway of D_mCB group. The pre-TC disturbances of D_mCB tend to have strong initial relative vorticity and gradually intensifies, and the attendant anticyclone at the northwest of the disturbance is featured since several days before TC formation. Besides, the intensity of vertical wind shear at the mid-to-upper troposphere tend to be low, which would favor the vorticity intensification after active deep convection activities. In the same

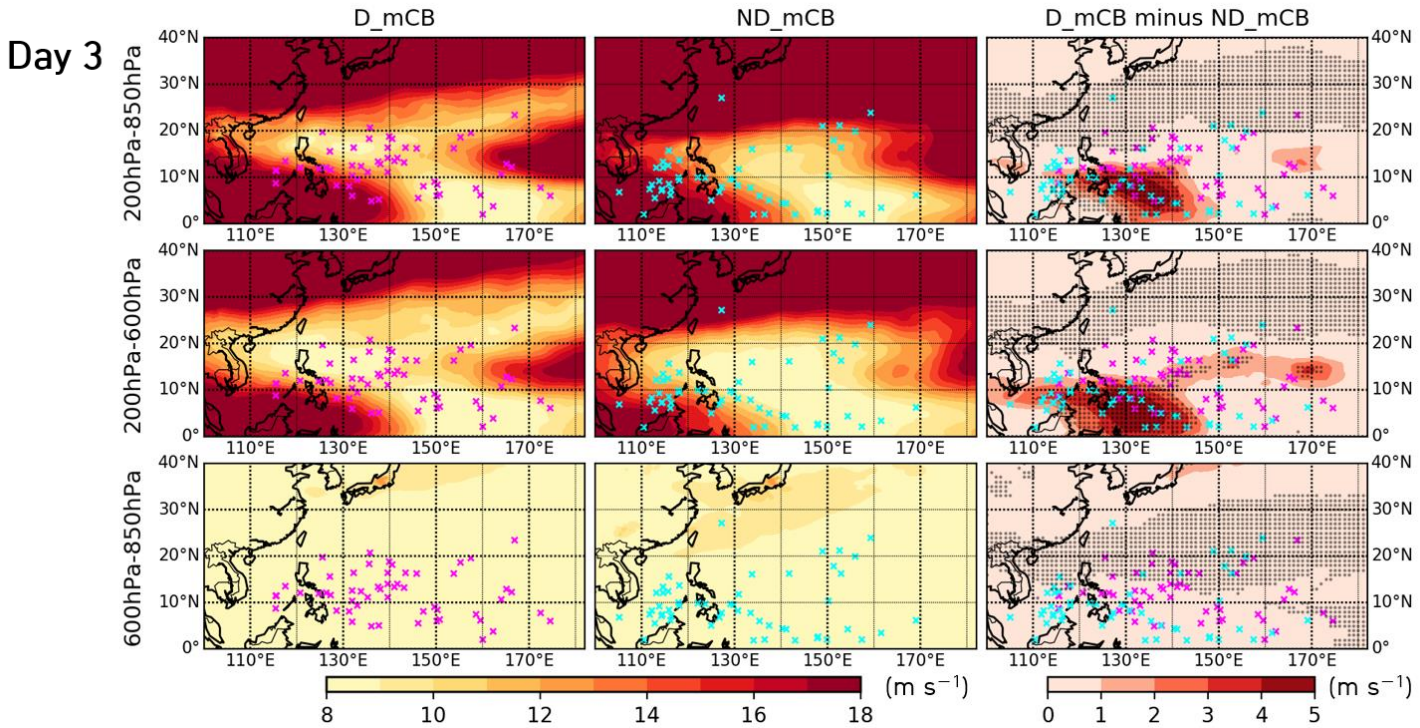

Figure 21. Composite fields of slowly-varying (i.e., 9 days low-pass filtered) vertical wind shear environment (m s^{-1}) between (top) 200 hPa and 850 hPa, (middle) 200 hPa and 600 hPa, (bottom) 600 hPa and 850 hPa of (left) D_mCB, (center) ND_mCB, and (right) ND_mCB minis D_mCB on Day 3. Cyan and magenta 'x' indicate the vort-max locations of D_mCB and ND_mCB disturbances. Black dots in the right panels indicate significant difference between D_mCB and ND_mCB in 95% confidence level.

vein, the disturbances in ND_mCB group also accompany a series of active CBs, but it decays after a couple of days, due to the weak initial vorticity, and strong mid-to-upper vertical wind shear. The attendant anticyclone is also not found around the non-developing disturbances.

3.2.2. Case study on TC Hagupit (2008)

The previous section describes the composite feature of group D_mCB, here, one representative case is chosen to take a closer look at TC formation process. By considering the thermodynamic and dynamic elements illustrated in the previous section, TC Hagupit (2008) is chosen as a representative case and similarly analyzed.

The deep convection area time series shown in Figure 22a is featured with repeated diurnal (or semi-diurnal) fluctuation. The relative humidity is high (> 70%, Figure 22b) throughout the troposphere except for around 700 hPa for several hours. The only exception feature is the sudden decrease in the mid-to-upper tropospheric relative humidity under 60% one day before TC Hagupit formation. This is likely due to latent heat release associated with convection. The warm temperature anomaly appears on Day 1 and gradually develops (Figure 22c). In this case, the warm temperature anomaly bifurcates on Day 4, a warm-core at the upper troposphere and the other warm-core at the mid-troposphere, which merge on TC Hagupit formation day (Day 6). Especially on Day 5, two warm anomalies are significant. Whereas the deep convection area on Day 5 is quite small compared to the adjacent days (Day 4 or Day6), the bifurcation is thought to be due to different

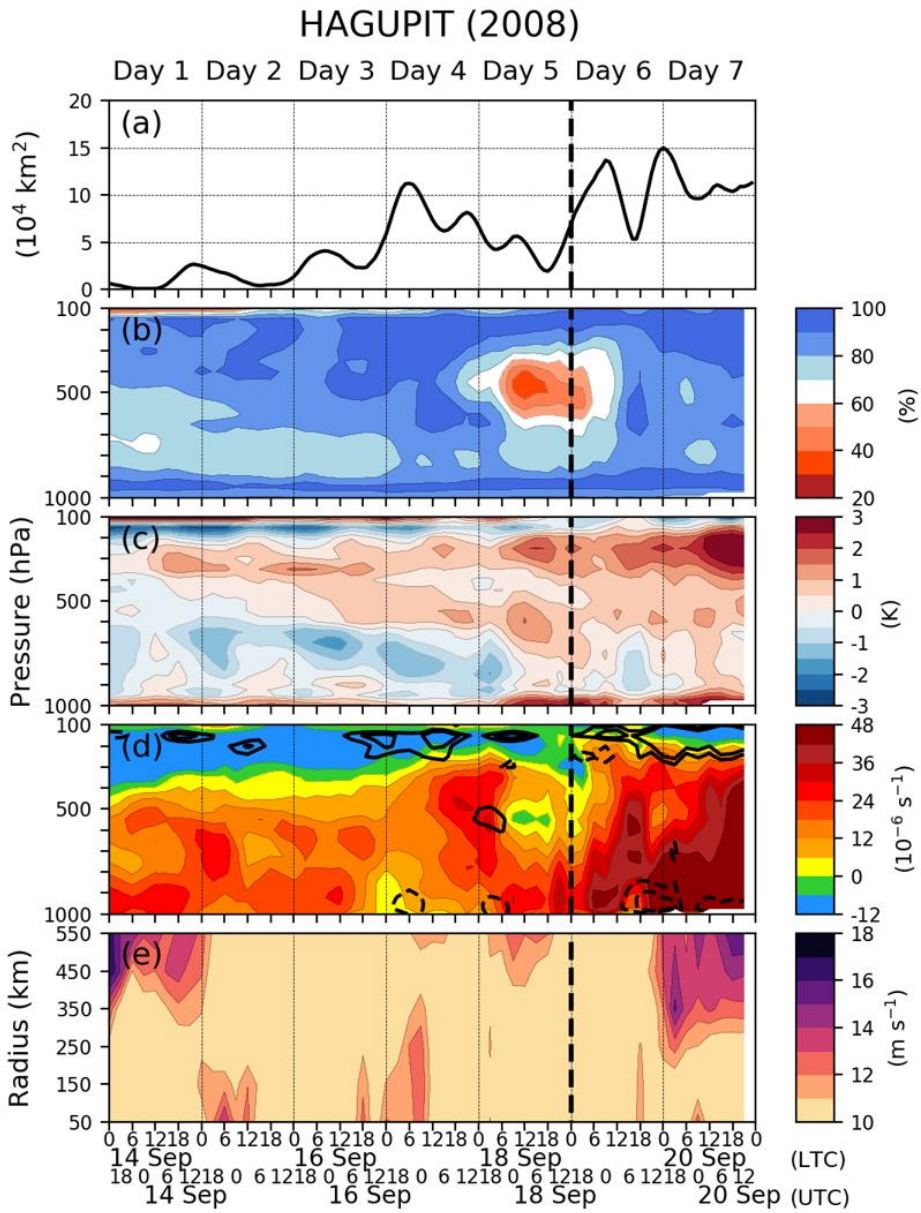

Figure 22. The same as Figure 16 but for Hagupit (2008) case.

height of convection. Moderate height of convection might cause the warm core in the mid-troposphere and deep convection reaching the tropopause (shown in the deep convection time series) might cause the warm core in the upper troposphere. And, integration of latent heat cause by all convection might dropped the relative humidity in the mid-to-upper troposphere. However, this is only a circumstantial speculation and detailed verification will be needed to assert this hypothesis.

The time evolution of relative vorticity in Figure 22d shows the low-tropospheric maximum and gradual intensification. Initially, the relative vorticity is over 16×10^{-6} s^{-1} on Day 1, and as the value reaches over 36×10^{-6} s^{-1} at the end of Day 5, and Hagupit has formed. The attendant secondary circulation occurs on Day 4 and 5 diurnally. The vertical wind shear shown in Figure 22e is lower than 11 m s^{-1} almost the entire pre-genesis period except for several time period.

The following analysis with scale-decomposition also shows consistent result with the composite analysis. In Figure 23a, the disturbance scale vorticity and horizonal wind streamline at 850 hPa are shown. As seen in Figure 19, the wave train of anticyclone-cyclone-anticyclone is clearly depicted around the pre-Hagupit disturbance. The slowly-varying large-scale relative vorticity at 600 hPa and 850 hPa (Figure 23b, c) is complex around pre-Hagupit. Pre-Hagupit disturbance travels along the narrow region of positive vorticities. The slowly-varying large-scale vertical wind shear environment around pre-Hagupit is very low (< 8 m s^{-1}) throughout entire pre-genesis period in between 200 hPa and 600 hPa and throughout entire pre-genesis and post-genesis period in between 600 hPa and 850 hPa. This

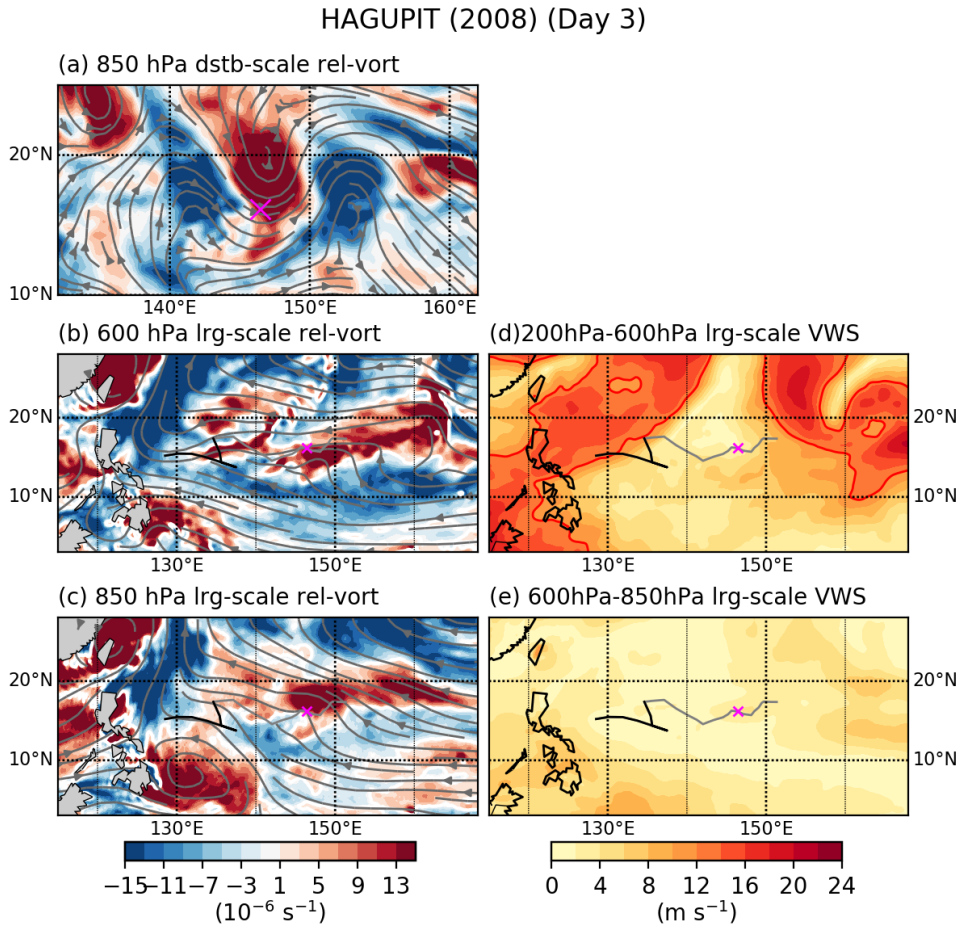

Figure 23. (a) Synoptic-scale (i.e., 2.5-9 days band-pass filtered) 850 hPa relative vorticity (shading, 10^{-6} s^{-1}) and horizontal wind (streamlines). (b, c) Slowly-varying large-scale (i.e., 9 days low-pass filtered) relative vorticity (shading, 10^{-6} s^{-1}) and horizontal wind (streamlines) at (b) 600 hPa and (c) 850 hPa. (d, e) Slowly-varying large-scale (i.e., 9 days low-pass filtered) vertical wind shear environment (m s^{-1}) between (d) 200 hPa and 600 hPa, (e) 600 hPa and 850 hPa. The red contours in (d, e) indicate 12 m s^{-1}. Magenta 'x' indicates the vort-max location, and gray and black solid lines indicate the five-day pre-genesis and two-day post-genesis vort-max track. All information here shows TC Hagupit case on 16 September 0000 LTC (15 September 1400 UTC).

case study on the formation of TC Hagupit (2008) confirms that the composite analysis on D_mCB is valid.

3.2.3. Schematic diagram

By integrating the composite analysis and case study of D_mCB, a schematic diagram is presented in Figure 24a. In comparison with D_mCB, a schematic diagram of ND_mCB is presented in Figure 24b. TC formation of D_mCB shows classical formation pathway. A pre-existing disturbance with incipient vorticity accompanies a series of deep convection prior to TC genesis. The environmental moisture is also abundant for D_mCB (not shown in the schematic diagram) which can promote moisture convergence in the lower troposphere Particularly from this study, existence of anticyclone(‘A’)-cyclone(‘C’)-anticyclone wave train in the lower troposphere is noticed from via scale decomposition in D_mCB, whereas such wave train feature is not noticed from ND_mCB. A series of active deep convection intensifies the relative vorticity around the cyclonic circulation, and the latent heat is released in the mid-to-upper troposphere, forming a warm-core of TC. The strength of vertical wind shear in the environment is very low. As learned from the decay of ND_mCB, strong vertical wind shear in mid-to-upper troposphere would provide unfavorable condition for TC genesis.

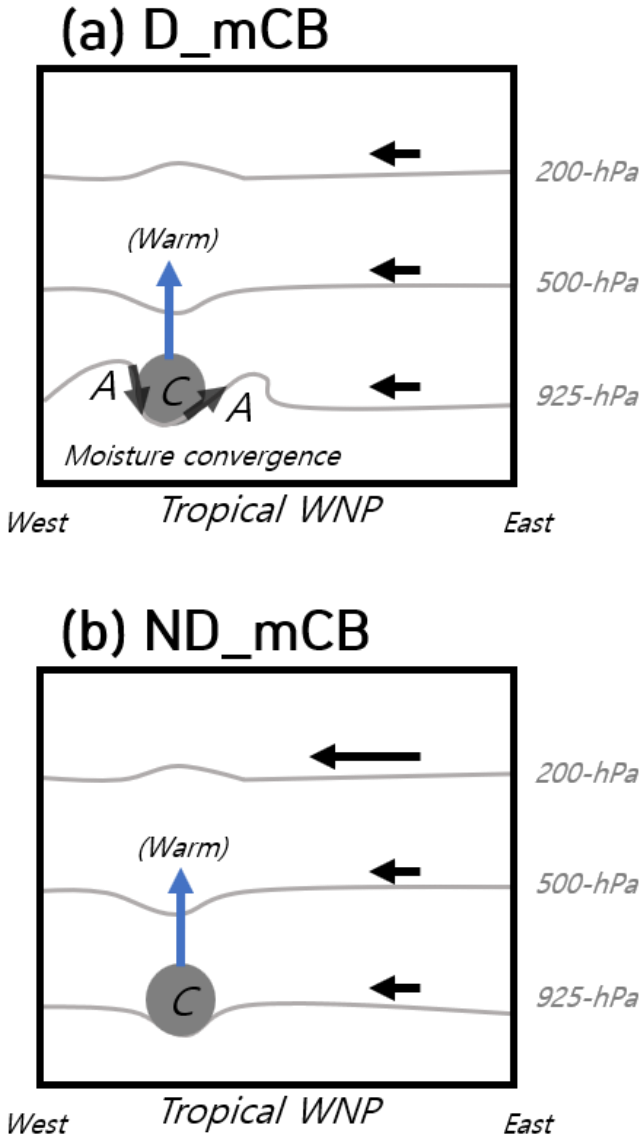

Figure 24. Schematic diagram of TC formation pathway of (a) D_mCB and non-formation of (b) ND_mCB. The dark gray shadings indicate cyclonic circulation, and the gray solid lines indicate geopotential heights. Black arrows are horizontal flow, and blue arrows are convective ascent.

3.3. Tropical cyclogenesis without mCB

3.3.1. Multi-scale environment analysis

From this section the TC formation of D_no will be investigated. Especially, the composite fields of D_no environment will be statistically compared to that of D_mCB environment.

Firstly, thermodynamic evolution of TC genesis without mCB (D_no) is examined in view of convective-environmental evolution. Figure 25b shows the time-evolution of area-averaged relative humidity throughout the entire troposphere within 500 km radius circle around the vort-max positions. In comparison with D_mCB, the low-to-middle (800–400 hPa) atmospheric conditions of D_no remain significantly dry (< 70 %) on Day 1 and 2 in 95% confidence level. On Day 3, humidity increases in the low-to-mid troposphere, but statistical comparison presents significantly dry environment compared to D_mCB. This is consistent with deep convection evolution, because the deep convection area of D_no is also significantly lower than D_mCB. On Day 5, the moist atmospheric condition of mid-level RH > 80% is continuously maintained throughout the troposphere, and deep convection area increases at the end of Day 5, i.e., several hours prior to the TC formation day (Day 6).

The upper-tropospheric zonal temperature anomaly of is under 1 K on Day 1 and 2 (Figure 25c). This warm anomaly gradually increases every day, but the magnitude is lower than that of D_mCB even after TC formation.

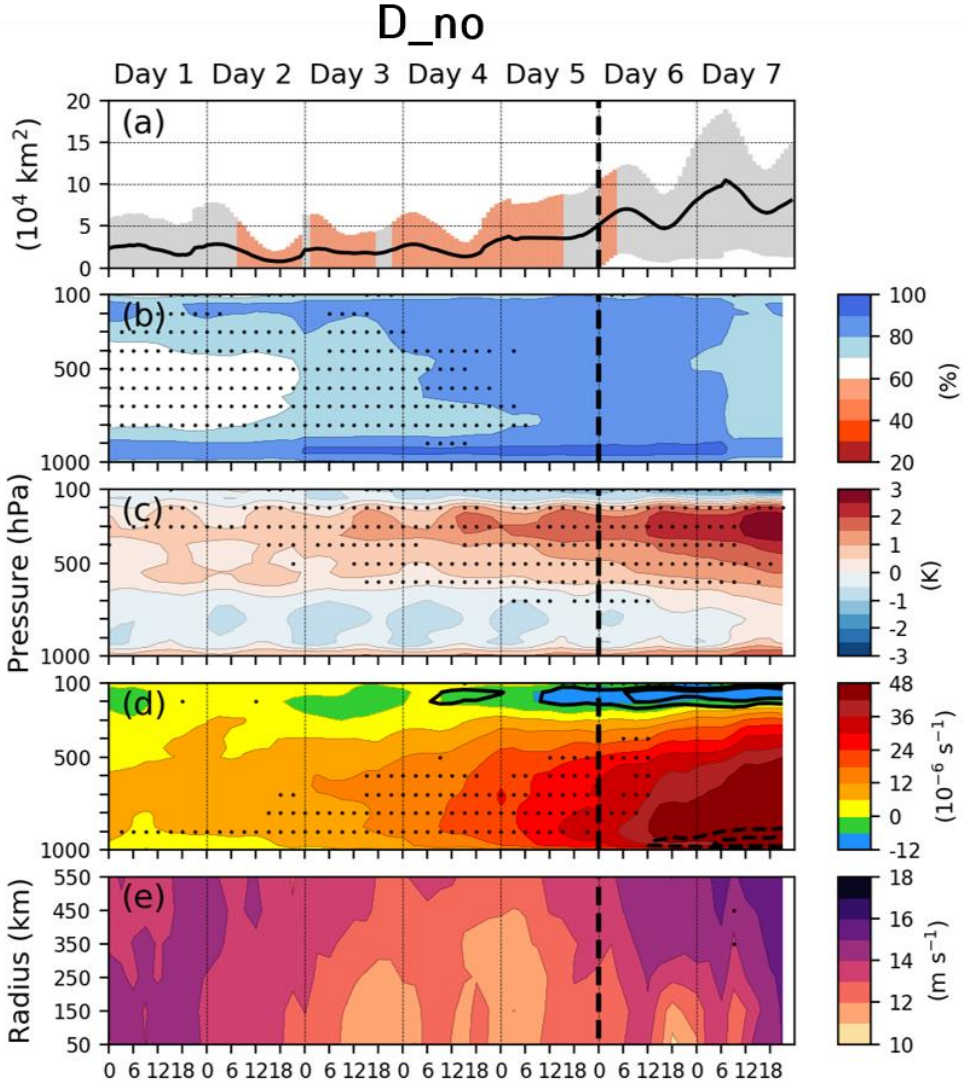

Figure 25. The same as Figure 16 but for D_no. Orange whiskers in (a) and black dots in (b–e) indicate significant difference compared to D_mCB at the 95% confidence level.

The relative vorticity evolution of D_no in Figure 25d is quite interesting. Because on Day 1 and 2, the relative vorticity does not show clear maximum in the lower troposphere, but the relative vorticity ~12 × 10^{-6} s^{-1} is widely distributed in the entire troposphere. Unlike a normal warm-core low-pressure system, which low-level cyclonic inflow is balanced by upper-level anticyclonic outflow, D_no accompanies positive relative vorticity throughout the troposphere. Besides, the intensification of relative vorticity first occurs in the mid-troposphere on Day 3, in contrast to the lower-tropospheric peak in D_mCB. On Day 4, relative vorticity of D_no intensifies in the lower troposphere (22.0 × 10^{-6} s^{-1}), which value is finally larger than that of ND_w (20.9 × 10^{-6} s^{-1}). Consistent with unclear vorticity structure as well as convection activities, the lower-tropospheric branch of system-scale secondary circulation (convergent inflow, < –10 × 10^{-6} s^{-1}) only occurs in post-genesis periods (Day 6 and 7). The upper-tropospheric branch of system-scale secondary circulation (divergent outflow, > 10 × 10^{-6} s^{-1}) is apparent only from Day 4.

Vertical wind shear on Day 1 is stronger than 14 m s^{-1} and that on Day 2 is stronger than 13 m s^{-1} (Figure 25e). The vertical wind shear magnitude within 350 km radius becomes lower than 12 m s^{-1} during the nighttime on Day 3 and 4 but it is still larger than D_mCB. However, the difference between D_mCB and D_no is not significant in 95% confidence level. In addition to a weaker relative vorticity, TC genesis for D_no is not favorable under a strong vertical wind shear. In a previous study by Gray (1968), the impact of the vertical wind shear is known to provide

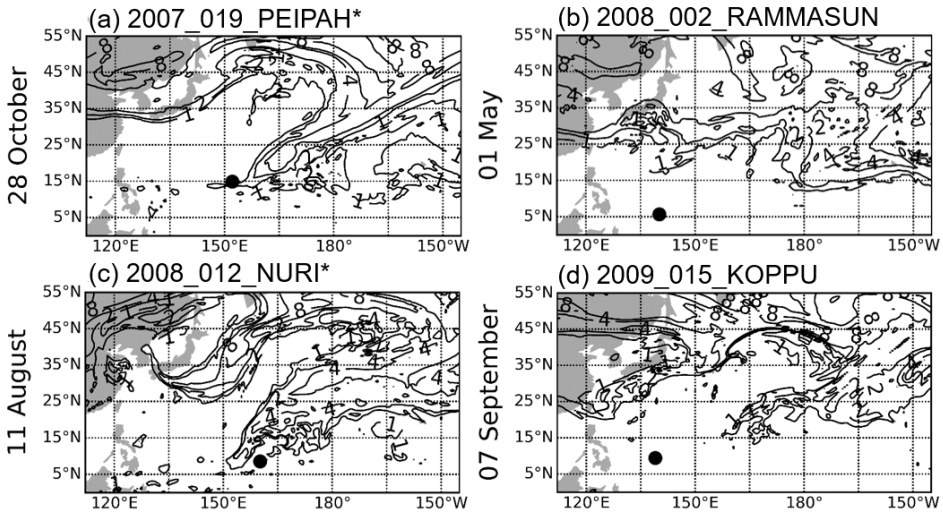

Figure 26. Potential vorticity (contours, 1, 2, 4, and 8 PVU; 1PVU = 1.0×10^{-5} m^2 s^{-1} K kg^{-1}) on the 350-K isentropic surface at five days prior to TC formation of (a) Peipah (2007), (b) Rammasun (2008), (c) Nuri (2008), (d) Koppu (2009). The dots denote the vort-max position of pre-TC. In each title, the asterisk notes a membership on the group of potential vorticities (D_pv) and no-asterisk notes a membership on the group of unknown formation pathway (D_mixed).

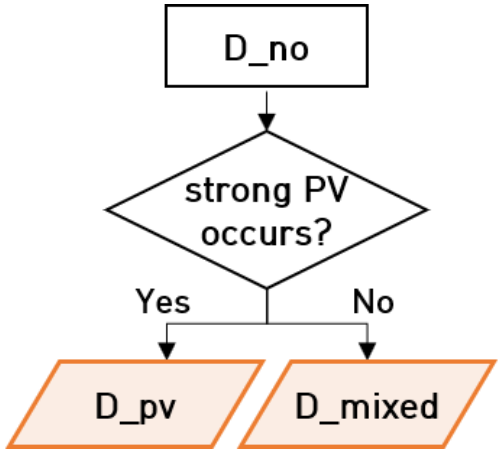

Figure 27. Flow chart of D_no sub-categorization into two groups. D_pv includes TCs, whose formation are likely related with strong PV in the upper troposphere, and D_mixed includes the rest of TCs, whose formation pathway are still unknown.

entrainment to the disturbance, which disturbs the accumulation of condensation latent heating in the vortex, preventing its deepening (Park et al. 2013; Tang and Emanuel 2012).

Yet, the composite analysis on TC formation process of D_no is not fully understood. Convective indication of TC formation in D_no group is found only from a day prior to the formation day, whereas dynamic and thermodynamic environment become favorable only about one or two days prior to the formation. Thus, large-scale environmental monitoring concurrent with convective cluster tracking is important for TC formation forecasting. Given the absence of a series of deep convective bursts, the rapid intensification of the vorticity as well as rapid increase in deep convection area just few days prior to TC formation may be driven primarily by external large-scale forcing such as the TUTT (Sadler 1975, 1976, 1978) or a northeasterly surge (Lin and Lee 2011). Synoptic-scale precursors may vary for each case of TC formation. To identify one possible external dynamic constraint responsible for an abrupt TC formation without mCB, focus is placed on the origin of the high value of relative vorticity in the upper troposphere.

To focus on the strong vorticity in high altitudes, the PV distribution at the 350 -K surface is investigated prior to TC formations. Note that the altitude of 350-K isentropic surface can be different by latitude (e.g., lower stratosphere at mid-latitude and upper troposphere in the tropics, Bluestein 1993; their figure 1.137). The result showed that the pre-TC vorticity of 12 TCs (out of 26) can be traced back to the strong PV in the upper troposphere on three-to-five days prior to their formation

Table 6. TC number, TC name of members of D_no in each year. The members with asterisk belong to D_pv and the rest belong to D_mixed.

Year 2007	Year 2008	Year 2009
00_KONG-REY 03_MAN-YI 04_USAGI* 09_FITOW 13_14W_NONAME 16_KROSA* 19_PEIPAH*	01_NEOGURI 02_RAMMASUN 03_MATMO 06_FENGSHEN 10_11W_NONAME 12_NURI* 15_16W_NONAME* 16_17W_NONAME* 18_JANGMI* 22_BAVI* 24_HAISHEN* 25_NOUL 26_DOLPHIN*	03_NANGKA* 13_MUJIGAE 15_KOPPU 20_NEPARTAK 21_LUPIT* 23_24W_NONAME

(typical examples are shown in Figure 26a, c; hereafter group of D_pv) and the rest 14 TCs could not (shown in Figure 26b, d; hereafter group of D_mixed). The subcategorization algorithm is visualized in Figure 27 and full list of those names and formation years are listed in Table 3. The group D_pv note TC formations are likely related with strong PV in the upper troposphere, and the group D_mixed includes the rest of TCs, whose formation pathway are still unknown.

The track of pre-TC vorticities and the location of TC formations of two groups are compared in Figure 28. Pre-TCs of D_pv originate from the open ocean north of 10°N and also form over the open ocean, whereas the TCs of D_ unknown tend to originate near the equator and forms near the islands, except for several cases. The distribution on the formation month of the year (Table 7) show that TCs in D_pv are distributed from May to December and maximized on September and October, and the formation time of TCs in D_mixed is relatively broad distributed from March to November without any significant seasonal peak.

In Figure 29, the atmospheric evolution of two groups are introduced. The sub-classified group D_pv present very limited deep convection area on Day 1–4. Only in the nighttime on Day 4, a deep convection area increases. On the other hand, the other sub-classified group D_mixed present diurnal fluctuation on its deep convection area. Note that even though the composite time series of deep convection of D_mixed likely shows diurnal fluctuations, the D_mixed disturbances are classified as not having mCB before its formation. When considering the quantitative thresholds of four CB features applied, D_mixed must be having weaker magnitude

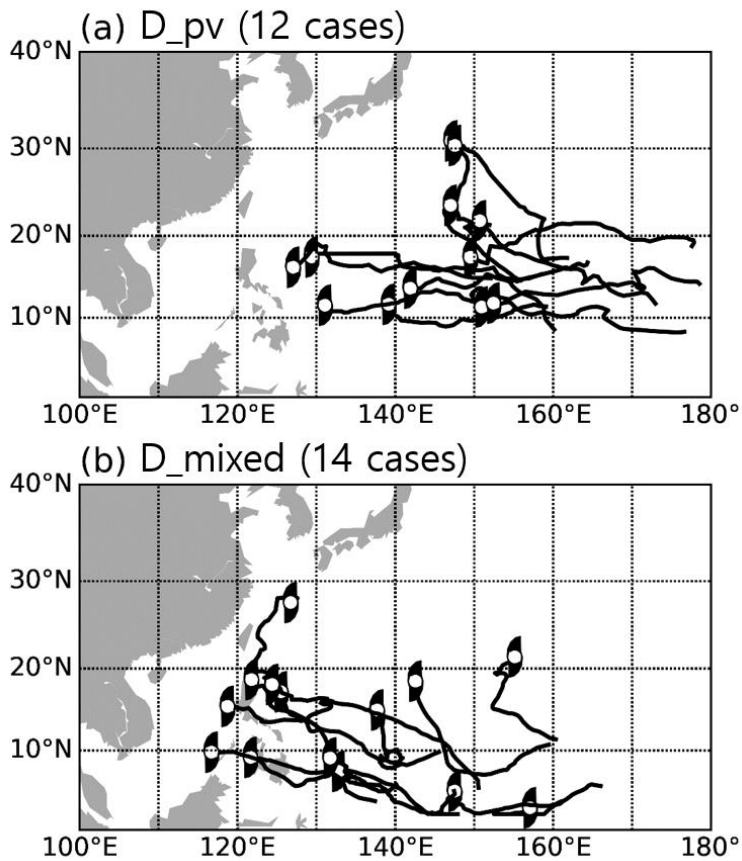

Figure 28. The five-day pre-TC vorticity track (black lines) and the location of TC formation (hurricane signs) of (a) D_pv and (b) D_mixed.

Table 7. Distribution of formation month of the year of (a) D_pv and (b) D_mixed.

	J	F	M	A	M	J	J	A	S	O	N	D	Total
(a) D_pv	0	0	0	0	0	1	1	1	4	2	2	1	12
(b) D_mixed	0	0	1	1	2	1	1	2	3	1	2	0	14

of CBs which features lower quantities than the thresholds. Relative humidity in the low-to-upper troposphere remains under 60% on Day 1–3 among D_pv, forming unfavorable thermodynamic environment for deep convection, which is natural considering the limited area of deep convection. However, the relative humidity increases over 70% in the Day 4 afternoon simultaneous with increase in the area of deep convection. Meanwhile, relative humidity remains over 70% since Day 1 for D_mixed cases. The upper-tropospheric zonal temperature anomaly accompanies negative temperature anomaly on Day 1 of D_pv. The cold temperature anomaly transits into a warm temperature anomaly on Day 3. For D_mixed, however, the upper-tropospheric zonal temperature anomaly accompanies clear warm temperature anomaly since Day 1. The composite characteristics of D_mixed so far are largely similar with that of D_mCB.

Composite analysis on their evolution of relative vorticity of D_pv show that the relative vorticity is maximized in the upper troposphere on Day 1–3. The location of vorticity maximum redistributes into the lower troposphere on Day 3. For D_mixed, the relative vorticity is maximized in the low-to-mid troposphere on Day 1. And the vorticity gradually intensifies, the maximum of vorticity occurs in the mid-troposphere on Day 3. The height location of maximum vorticity on Day 3 is distinctive from that of D_mCB. The magnitude of vertical wind shear within the pre-TC vorticity reaches over 16 m s^{-1} on Day 1 and 2 for D_pv. Strong vertical wind shear is likely to be related with strong relative vorticity and consistent with the absence of deep convection. However, the vertical wind shear is not very strong (<

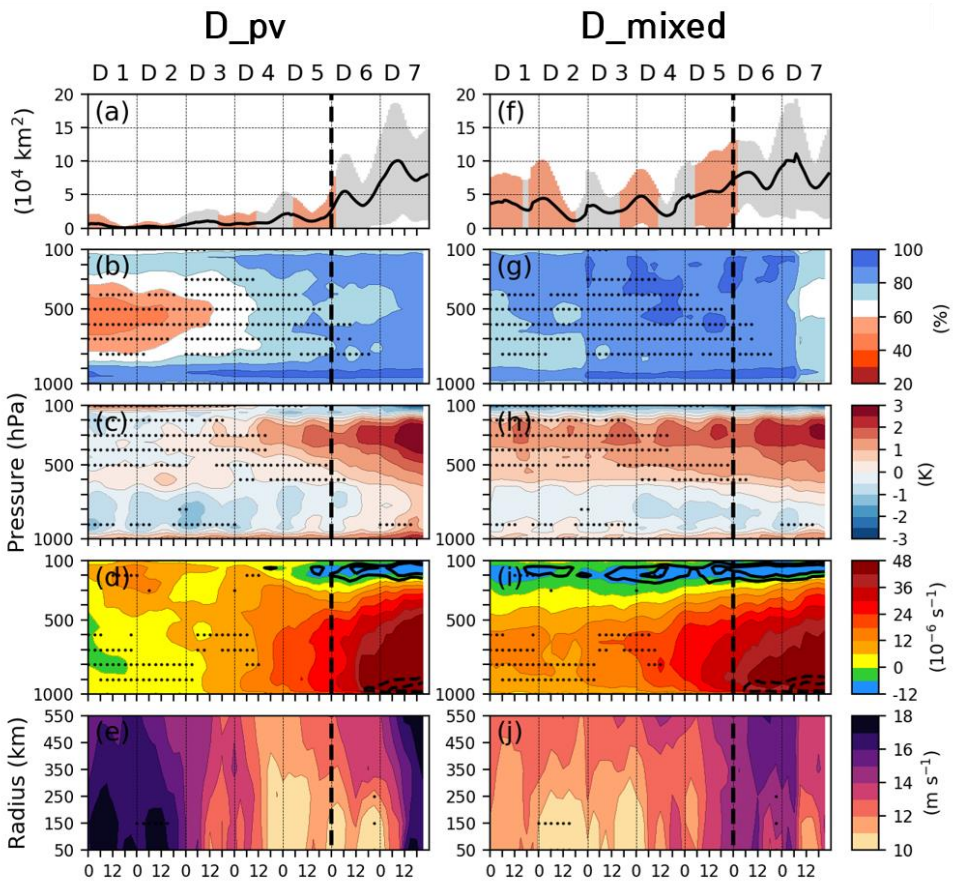

Figure 29. The same as Figure 16 but for D_pv and D_mixed. Orange whiskers in (a, f) and black dots in (b–e, g–i) indicate significant difference compared between D_pv and D_mixed at the 95% confidence level.

12 m s^{-1} near vort-max center) for D_mixed.

D_pv includes 12 TCs out of 80 during 2007–2009, which accounts for 15% of total, eventually developed into a TC despite the absence of multi-day diurnal deep convection under the environment of low relative humidity and strong vertical wind shear. To further scrutinize the TC formation pathway of D_pv, TC Peipah (2007) is selected for a case study in the next section. A special focus is placed on the role and origin of strong relative vorticity in the upper troposphere to explain how the unfavorable environment of TC formation (such as low relative humidity and strong vertical wind shear) evolves to a favorable one. Finally, the transition of cold temperature anomaly into a warm temperature anomaly will be explained.

D_mixed includes 14 TCs out of 80 during 2007–2009, which accounts for 17.5% of total. This group of pre-TC present a diurnal fluctuation in its deep convection area, but the CB magnitudes do not satisfy the threshold quantities defining mCB. Overall atmospheric evolution is consistent with the group D_mCB, but the only difference is found in the vertical location of relative vorticity maximum. Unlike D_mCB, which has the vorticity maximum in the lower troposphere, D_mixed shows mid-tropospheric vorticity maximum on Day 3, i.e., three days before TC formation. The TC formation pathway of D_mixed group is thought to be overall similar with D_mCB.

The synoptic-scale (2.5–9 days) relative vorticity among D_pv and D_mixed are shown in Figure 30 and the field is statistically compared to that of D_mCB. Both for D_pv and D_mixed, the attendant anticyclones are clearly shown around

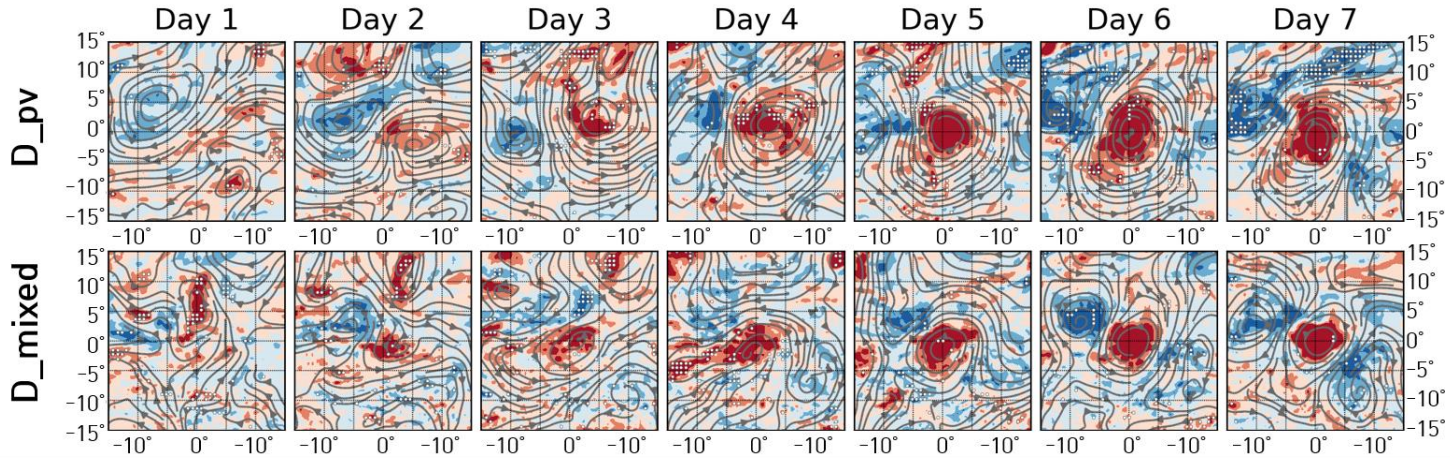

Figure 30. The same as Figure 19 but for (top) D_pv and (bottom) D_mixed. White dots indicate significant difference compared to D_mCB in 95% confidence level.

pre-TC disturbance. For D_pv, an anticyclone is more dominant than a cyclone on Day 1. The size of cyclone and anticyclone are similar on Day 2 and the size of cyclone becomes more dominant on Day 3 to 7. Both the size of cyclone and the magnitude of relative vorticity of D_pv are significantly larger than those of D_mCB in 95% confidence level. As the size of cyclone exceeds 7 degree in radius, the anticyclone in the east is not clearly shown. For D_mixed, overall pattern and size resembles that for D_mCB. An anticyclone-cyclone-anticyclone wave train can be found every day except for Day 1. When compared to D_mCB, the circulation pattern is less clear but the magnitude of positive and negative relative vorticities is larger in 95% significance level.

Relative vorticity in the slowly-varying environment on Day 3 of D_pv and D_mixed are shown in Figure 31. On Day 3 of D_pv, the majority of pre-TC disturbances are located away from the area where slowly-varying large-scale relative vorticity both at 600 hPa and 850 hPa are high. This feature implies possibility that TC formation of D_pv group may be less associated with slowly-varying large-scale relative vorticity in the mid-to-lower troposphere. On Day 3 of D_mixed, the majority of pre-TCs are located in the area where slowly-varying large-scale relative vorticity both at 600 hPa and 850 hPa are relatively high in the WNP. But, the magnitude of large-scale relative vorticity of D_mixed is lower than that of D_mCB especially at 600 hPa. Whereas the streamlines confluence around pre-TCs of both D_mCB and D_mixed, the meridional shear of streamlines around D_mixed seems to be larger than that around D_mCB.

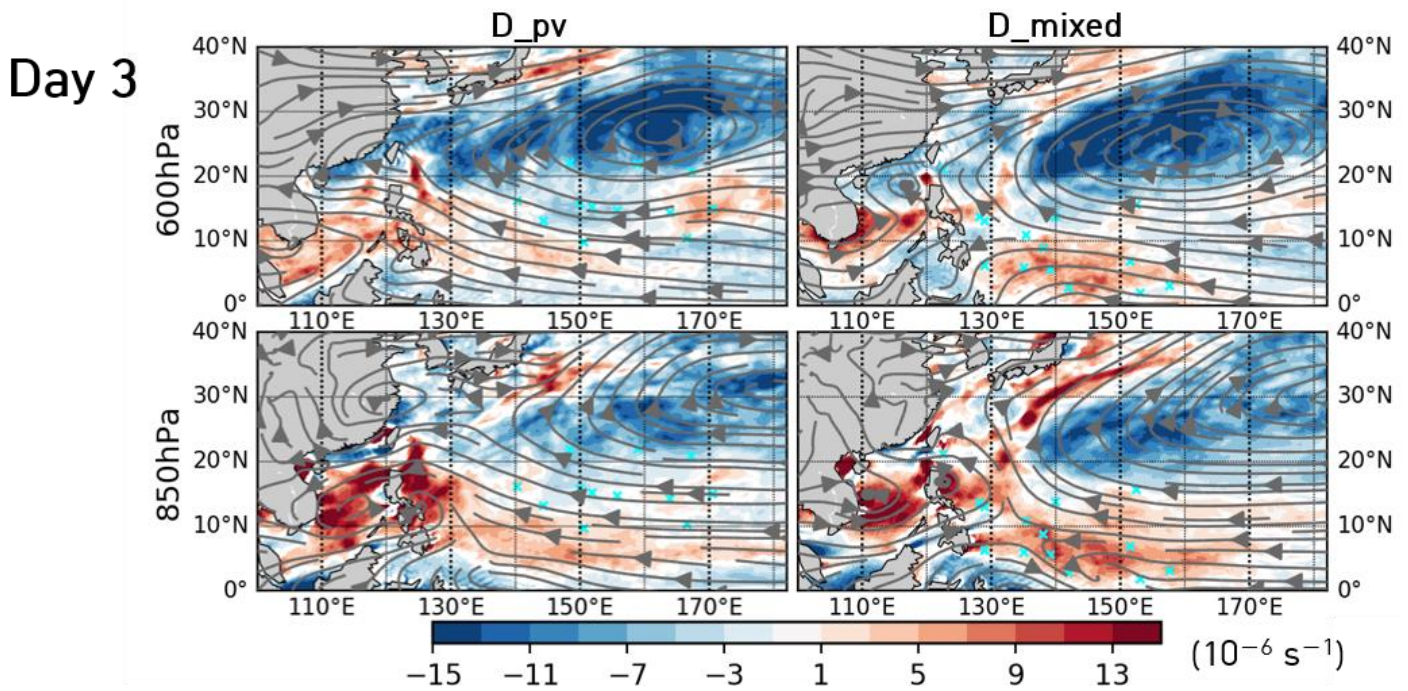

Figure 31. Composite fields of slowly-varying (i.e., 9 days low-pass filtered) relative vorticity (shading, 10^{-6} s^{-1}) and horizontal wind (streamlines) at (top) 600 hPa and (bottom) 850 hPa of (left) D_pv and (right) D_mixed on Day 3. Cyan 'x' indicates the vort-max locations of each D_pv and D_mixed disturbances.

Figure 32 shows slowly-varying large-scale vertical wind shear environment of D_pv and D_mixed on Day 3 in three different height intervals: between 200 hPa and 850 hPa (top panels in Figure 32), 200 hPa and 600 hPa (middle panels in Figure 32), and 600 hPa and 850 hPa (bottom panels in Figure 32). The pre-TCs of D_pv are located around the tongue of large vertical wind shear between 200 hPa and 850 hPa in the WNP. The pre-TCs of D_mixed are also located in the other tongue of large vertical wind shear between 200 hPa and 850 hPa in the WNP. When separating the vertical wind shear around D_pv and D_mixed in two different height intervals, the mid-to-upper tropospheric vertical wind shear again accounts for most of the tropospheric vertical wind shear. Whereas the most of the feature of D_mixed resemble that of D_mCB, the mid-to-upper (600-200 hPa) tropospheric vertical wind shear environment around D_unknown are higher than D_mCB.

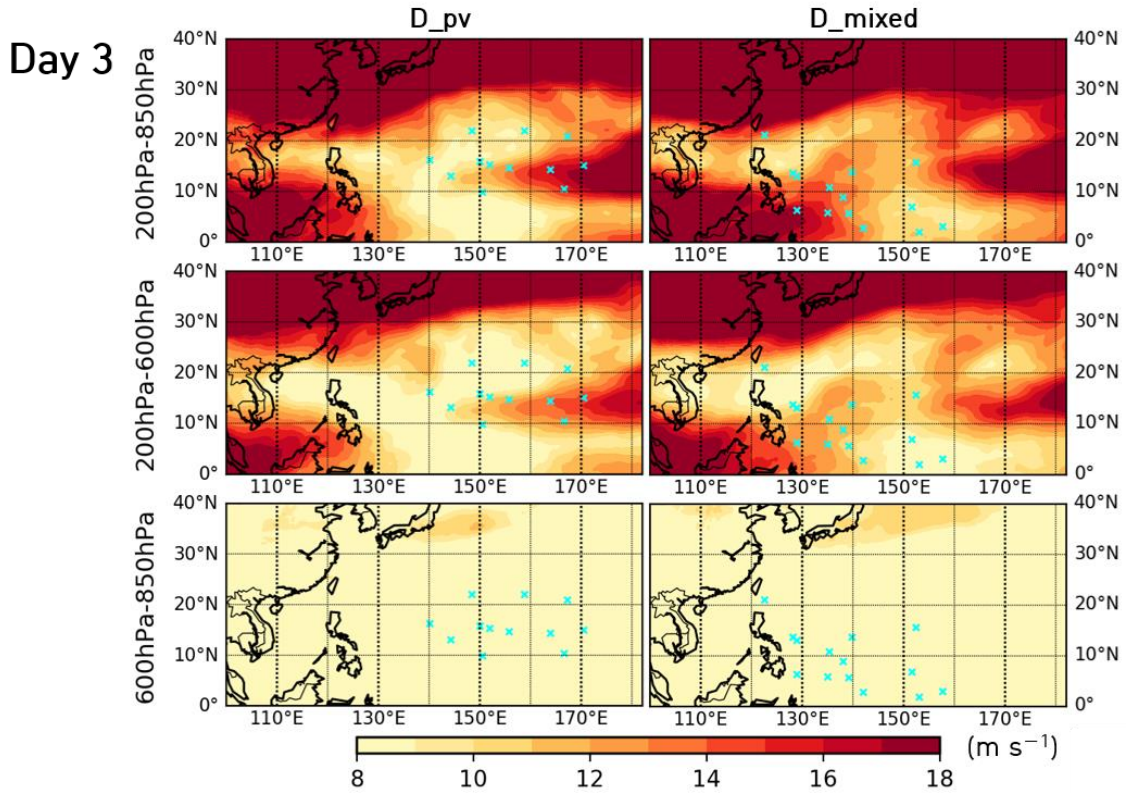

Figure 32. Composite fields of slowly-varying (i.e., 9 days low-pass filtered) vertical wind shear environment (m s^{-1}) between (top) 200 hPa and 850 hPa, (middle) 200 hPa and 600 hPa, (bottom) 600 hPa and 850 hPa of (left) D_pv and (right) D_mixed on Day 3. The red contours indicate 12 m s^{-1} (left and center panels) and 5 m s^{-1} (right panels) Cyan 'x' indicates the vort-max locations of each D_pv and D_mixed disturbances.

3.3.2. Case study on TC Peipah (2007)

Typically, a TC precursor disturbance originates from the tropics and moves westward following the synoptic wind pattern (e.g., subtropical anticyclone). When it reaches the western extent of the subtropical ridge, it propagates poleward with additional effects of the beta drift. The pre-Peipah (the precursor vort-max of Peipah) is different from the typical TC precursor in the WNP; it is of a non-tropical origin and moves in a much different path as shown in the Peipah's vort-max track from 7 days before (27 October) to 1 day after (4 November) its formation (Figure 33a). The Peipah vort-max, the PV maximum at 600- to 400-hPa average, originated from the subtropics at 29.2°N and 171.6°E on 27 October and subsequently moved southwestward. After 30 October, the vort-max position moved northwestward or westward within the 12–18°N until it was developed into Peipah on 3 November.

Similar to the difference in vort-max track between the two periods, that is, 27–30 October and 31 October to 3 November, the vertical structure of relative vorticity (Figure 33b) and the environmental vertical wind shear (gray line in Figure 33c) are also different between the two periods. A relative vorticity maximum is located in the upper-to-middle troposphere (500–100 hPa) during the first period, whereas the maximum vorticity occurs in the lower-to-middle troposphere (1,000–500 hPa) during the second period. Vertical wind shear around pre-Peipah exceeds 16 m s^{-1} in the first period (27–30 October), but became weaker (below 12 m s^{-1}) in the second period (31 October to 3 November) as the vort-max moved south into the tropical western Pacific. The area of deep convection increases on 28 and 30 October 1200

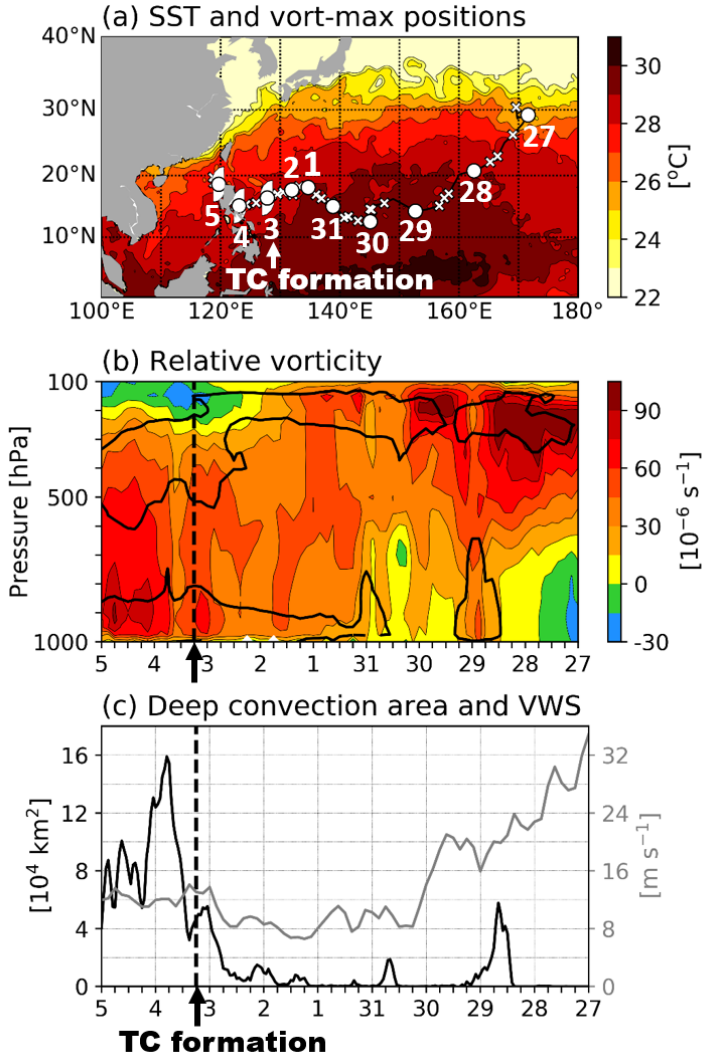

Figure 33. (a) The 8-day mean sea surface temperature (K) and 1-hourly (black line), 6-hourly (white cross), and daily 0600 UTC (white circles for pre-TC and hurricane signs for TC) vort-max positions of Peipah on 27 October to 5 November 2007. (b) Time-height diagram of relative vorticity (shading, 10^{-6} s^{-1}) and vorticity stretching rate (thick black contour, 7×10^{-6} s^{-2}) averaged within a 500-km radius about the vort-max positions. (c) One-hourly time series of deep convection area (black line, 10^4 km^2) constructed from IR minus WV BTs below 0 K area within a 500-km radius about the vort-max positions and 3-hourly time series of average vertical wind shear (gray line, m/s according to the axis on the right) within the same radius. The vertical dashed line in (b–c) indicates the date of Peipah formation. Note that zonal axis (time) in (b–c) is from right to left.

UTC in a 2-day interval during the first development period (black line in Figure 33c). During the second period, diurnal variation of deep convective area starts in small amplitude (< 8,600 km^2) within the weak vertical wind shear environment on 1 and 2 November, then the area of deep convection increases rapidly on 3 November as it develops into a TC. Two different driving forces for deep convection in each development period will be examined in this section. Firstly, the environmental characteristics associated with the transition of pre-Peipah between the first and second development periods will be described. After that, the role of strong upper tropospheric vorticity and the driving mechanism of deep convection in the first development period will be examined. The energetics of the interaction between the slowly varying environment and pre-Peipah are then discussed to describe the low-tropospheric TC vortex spin-up and subsequent TC formation in the second development period.

For the 7 days prior to the formation of Peipah, SSTs and vertical wind shear provided favorable environments for tropical transition (Davis and Bosart 2003, 2004, 2006; Sadler 1975, 1976, 1978) . In Figure 33a, pre-Peipah remained over regions where SST exceeded 26 °C. Strong vertical wind shear of over 16 m s^{-1} in the first development period was reduced to below 12 m s^{-1} in the second development period, providing favorable conditions for TC genesis (Gray 1968; Park et al. 2013; Tang and Emanuel 2012). In the environment of warm SST and weak vertical wind shear, an extratropical cold-core low is transformed into a tropical warm core low.

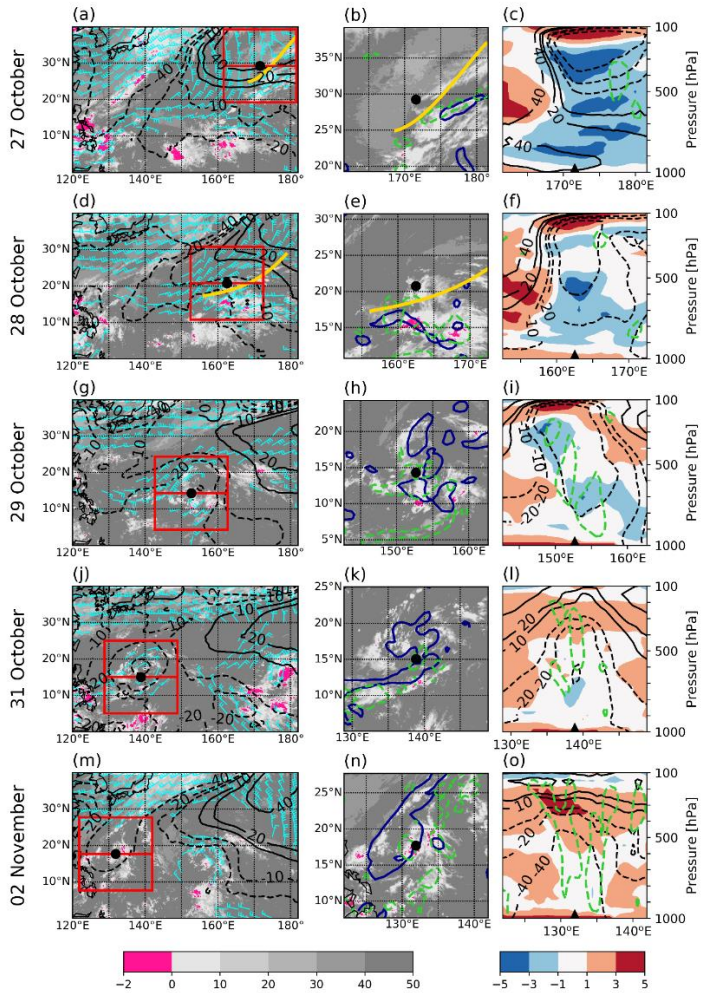

Figure 34. (a, d, g, j, m) MTSAT-1R IR minus WV BTs (K), 925 hPa zonal height anomaly (solid and dashed black contours, ±10, ±20, ±40 m) and 200 hPa horizontal wind vectors (over 16 m s^{-1} in barbs) at 0600 UTC on (a) October 27, (d) October 28, (g) October 29, (j) October 31, and (m) November 2. Time of the panels within each row are identical. (b, e, h, k, n) Enlarged MTSAT-1R IR minus WV BTs image within the red box in (a, d, g, j, m). Solid dark blue contour and dashed green contour each indicates 925 hPa relative vorticity of 30×10^{-6} s^{-1} and 500 hPa vertical velocity of –0.2 Pa s^{-1}, respectively. The yellow line in (a, b, d, e) represents the TUTT axis. (c, f, i, l, o) Vertical cross sections along the horizontal red line crossing the vort-max position in (a, d, g, j, m). Zonal height anomaly (solid and dashed black contours, ±10, ±20, ±40 m) and zonal temperature anomaly (shading, K) and vertical velocity (dashed green contours, –0.2 Pa s^{-1}) are plotted. The black dots in the first and second columns and triangles in the third column denote the vort-max position.

On 27 October, the traced-back vort-max is located within the TUTT (yellow line in Figure 34a, b indicates the TUTT axis) as shown in the 200 hPa wind field. Note that TUTT is a type of upper tropospheric trough that extends from the eastern to the WNP (Sadler 1975). Figure 34b shows the typical cloud distribution around the TUTT: a broad cloud-free region (IR minus WV BTs over 30 K) to the west of the trough and stretched cirrus (IR minus WV BTs below 10 K) to the east of the trough following the 200 hPa southwesterly flow (Figure 34a). The cross section of the TUTT is shown in Figure 34c. The negative height anomaly is maximized in the upper troposphere and penetrates into the middle troposphere. The entire troposphere below the TUTT is filled with negative temperature anomalies as the TUTT transports cold air equatorward from the higher latitudes. In the lower troposphere, no significant negative height anomaly appears around the vort-max position either in Figure 34a, c; however, a narrow region of a cyclonic relative vorticity at 925 hPa is indicated to the east the vort-max position in Figure 3b, colocated with 500 hPa ascending motions. Note that a cyclonic vorticity is not necessarily associated with negative height anomalies.

On 28 October, the TUTT penetrates further equatorward, as evidenced in the 200 hPa wind field in Figure 34d. In the lower troposphere, the cyclonic relative vorticity (Figure 34e) at 925 hPa is located southward from the vort-max position. This cyclonic vorticity region is associated with deep convective cloud areas, which are also co-located with 500 hPa ascending motions (Figure 34e). This deep convection persists for more than 6 h (see deep convection peak on 28–29 October

in Figure 33c); the low tropospheric relative vorticity amplifies with time (see the thick black contour in Figure 33b) as convective ascent stretches the preexisting low-level vorticity (Wissmeier and Smith 2011). The TUTT generally limits TC genesis via significant vertical wind shear (Penny et al. 2015) , but it can occasionally assist TC genesis by inducing strong updrafts over an ambient surface low (Sadler 1975, 1976, 1978; Trenberth 1978) or by destabilizing the troposphere (Juckes and Smith 2000). Considering the current examination on geostationary satellite images and atmospheric variables, the role of TUTT will be elaborated in the following.

On 29 October, the 925 hPa negative height anomaly deepens to develop a closed contour of −40 m near the vort-max (Figure 34g). Within this negative height anomaly, several patches of cyclonic relative vorticity are located (Figure 34h). The 200 hPa wind field in Figure 34g illustrates that the TUTT-cell is detached from the upper tropospheric trough. Along the 200 hPa cyclonic wind field, the cirrus clouds (IR minus WV BTs below 10 K) are scattered into a large rim shape. In the vertical cross section, the zonal height anomaly depicts a vertically well-developed cyclonic system with a cold temperature anomaly within it (Figure 34i). The axes of both the cold and negative height anomalies are tilted westward, and ascending motion exists throughout the troposphere (in several fragments) along the tilted axes of the temperature and the height anomalies. As this cold-core disturbance travels within the tropics, its structure begins to change.

On 31 October, as the vort-max moved into a weak vertical wind shear environment (below 12 m s^{-1}; Figure 33c), the low-pressure system developed a

vertical structure without notable tilting (Figure 34l). In the lower troposphere, a clear lower tropospheric low is established (Figure 34j, l) with the cyclonic relative vorticity of over 15×10^{-6} s^{-1} from 1,000 to 100 hPa (Figure 33b). The zonal temperature anomaly plot (Figure 34l) shows a warm-core-like feature, as the positive temperature anomaly appears in the upper troposphere above 500 hPa, while weak cold anomaly still remains in the lower troposphere. The reduced cold anomaly is likely due to the latent heat release from the transient deep convection on 30 October (Figure 33c). The negative height anomaly reaches near 200 hPa where the warm temperature anomaly is observed. Note that it is supported by the remaining 200 hPa cyclonic flow observed in Figure 34j, suggesting that the system still has some cold-core characteristics compared to the warm temperature anomaly surrounding the east and west of the vort-max position at lower-to-middle troposphere (Figure 34l).

After 2 days, a narrow deep convective cloud band (IR minus WV BTs below 0 K) developed near the vort-max position (Figure 34m, n); ascending motion through the entire troposphere is also evident as in Figure 34o. The superposition of deep convection (or ascending motion) over the lower tropospheric vortex is known to amplify the low-level cyclonic system via low tropospheric vortex stretching (see the thick black contour in Figure 33b; Wang 2014; Wissmeier and Smith 2011). In the cross section (Figure 34o), the largest warm anomaly, over 3 K, in the upper troposphere appears in the center; the zonal height anomaly also shows a strong negative (positive) height anomaly in the lower (upper) troposphere. The pronounced

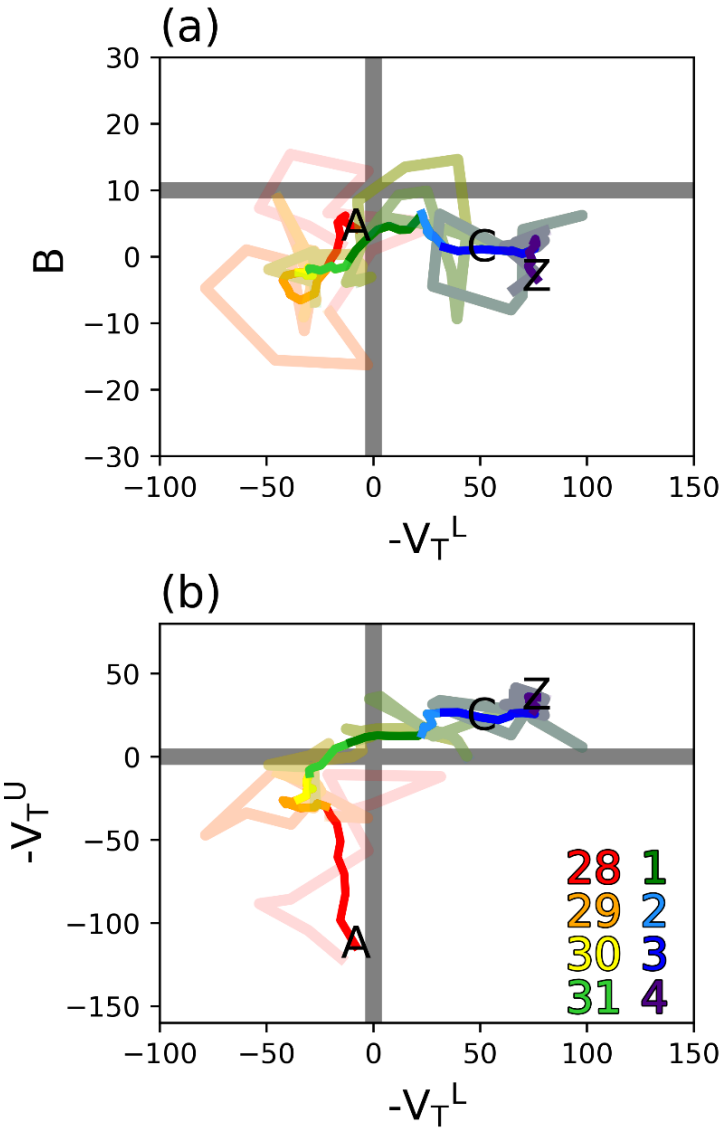

Figure 35. Cyclone phase diagram of pre-Peipah. Phase evolution of (a) $-V_T^L$ vs. B and (b) $-V_T^U$ vs. $-V_T^L$ are plotted where parameter B indicates 900 to 600 hPa storm-relative thickness symmetry, $-V_T^L$ indicates 900 to 600 hPa thermal wind, and $-V_T^U$ indicates 600 to 300 hPa thermal wind. Starting from October 28 0000 UTC (A) to November 4 2100 UTC (Z), the three-hourly status of pre-Peipah (light colored line) and it's 25-hour running average (vivid colored line) are plotted by corresponding colors of each date indicated at the right bottom in (b). The TC formation time (November 3 0600 UTC) is indicated as "C".

warm-core low then continues to strengthen on the following day and finally develops into Peipah on 3 November.

To objectively identify thermal structure of pre-Peipah, the cyclone phase diagram (Hart 2003) is plotted for 28 October to 4 November (Figure 35). The lower tropospheric cyclonic circulation is insignificant on 27 October (not shown). In Figure 35a, the value of the 900- to 600-hPa geopotential thickness symmetry (B) is mostly confined within ±10 m. A cyclone with B < 10 m is considered to be either a non-frontal structure or an occluded low; the pre-Peipah case corresponds to the latter (Hart 2003; R. E. Hart, personal communication, 18 April 2018).

In Figure 35b, the phase of the cyclone is located in the lower left quadrant on 28–30 October and transfers to the upper right quadrant on 1–4 November. Specifically, the upper tropospheric (600–300 hPa) thermal wind ($-V_T^U$) represents an upper tropospheric cold-core feature on 28–30 October ($-V_T^U < 0$), a neutral on 31 October ($-V_T^U \sim 0$), and an upper tropospheric warm-core feature on 1–4 November ($-V_T^U > 0$). In terms of the lower-tropospheric (900–600 hPa) thermal wind ($-V_T^L$), a lower tropospheric cold-core feature on 28–31 October ($-V_T^L < 0$) transits into a lower tropospheric warm-core feature on 1–4 November ($-V_T^L > 0$). Overall, the objectively diagnosed cyclone phase diagram verifies the tropical transition after 31 October.

In the first development period, the formation of a cold-core low (the precursor to Peipah) is explored further here in terms of a PV intrusion in the upper troposphere. It has been reported that a cut-off low or stratospheric PV streamer in the upper

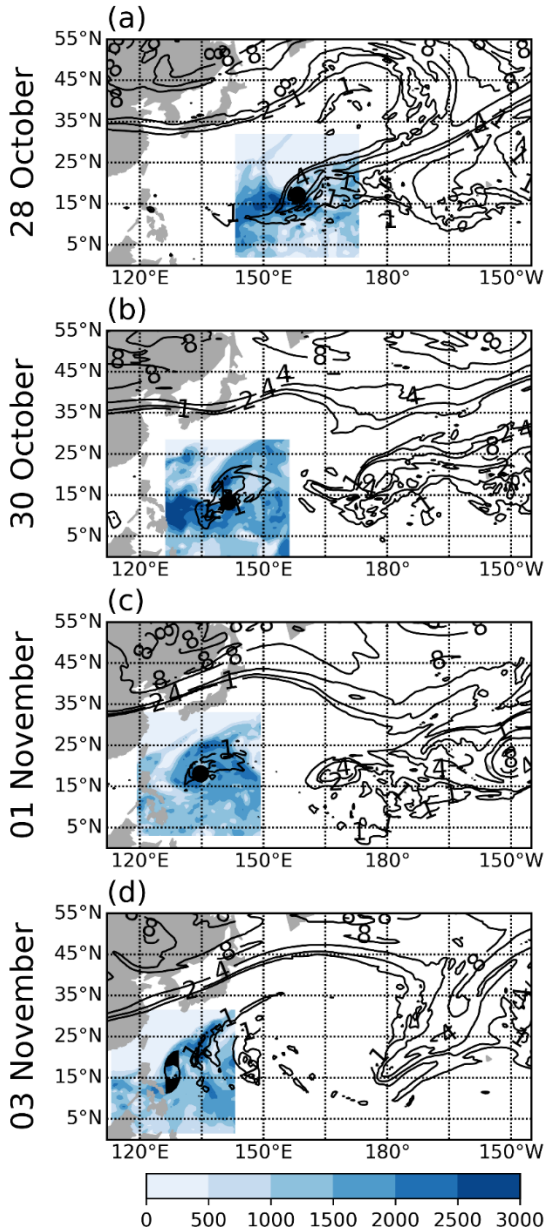

Figure 36. Potential vorticity (contours, 1, 2, 4, and 8 PVU; 1PVU = 1.0×10^{-6} m^2 s^{-1} K kg^{-1}) on the 350-K isentropic surface and CAPE (shadings, J kg^{-1}) (a) at 1200 UTC on October 28, at 1800 UTC on October 30, (c) at 0600 UTC on November 1, and (d) at 0600 UTC on November 3. CAPE is presented within 30° × 30° box around the vort-max position to focus on the main region. The dots and TC symbol each denote the vort-max position of pre-TC and TC, respectively.

troposphere associated with anticyclonic Rossby wave breaking (Martius et al. 2007; Waugh and Polvani 2000; Wernli and Sprenger 2007) can initiate organized deep convection (Waugh and Funatsu 2003) and a subtropical cyclone (Galarneau et al. 2015) by destabilizing the troposphere (Juckes and Smith 2000) or through quasi-geostrophic forcing for ascent (Hoskins et al. 1985; Trenberth 1978). Some of these subtropical cyclones occasionally develop into TCs as they travel across a warm SST region (Bentley et al. 2017).

Consistent with these previous studies, the role of upper tropospheric PV forcing and attendant deep convection on 28 and 30 October are explained by investigating the CAPE (Figure 36), and quasi-geostrophic vertical motion (Figure 37). In order to evaluate the quasi-geostrophic vertical motion, this study employs the same method as in Fischer et al. (2017) that solves a modified version of the Sutcliffe-Trenberth form of the quasi-geostrophic omega equation (Trenberth 1978) using successive overrelaxation.

On 28 October, the developing Rossby wave breaks anticyclonically (see the southwest-northeast tilting of PV contours around 160°E–180° in Figure 36a), resulting in an intrusion of high PV air from the midlatitude lower stratosphere into the subtropical upper troposphere by following the 350-K isentropic surface as previously explained; note that the altitude of 350-K isentropic surface can be different by latitude (e.g., lower stratosphere at midlatitude and upper troposphere in the tropics (Bluestein 1993; their Figure 1.137). This equatorward PV intrusion can also be seen from the strong upper tropospheric relative vorticity in Figure 33b,

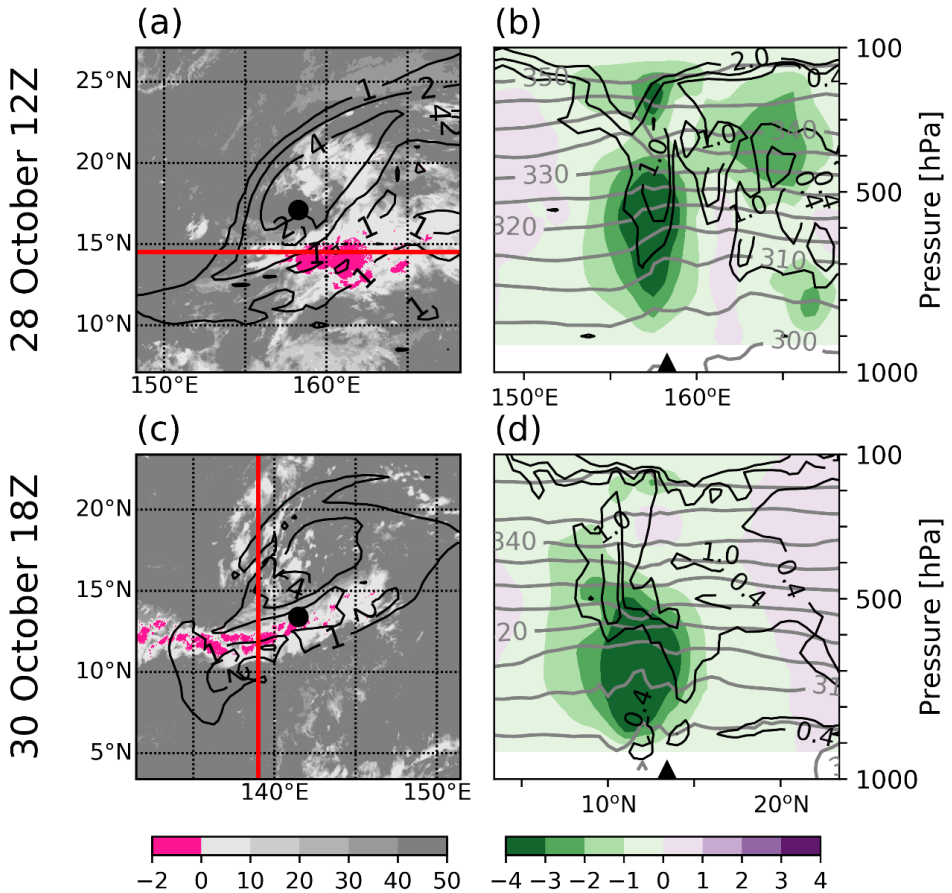

Figure 37. (a, c) The 350-K potential vorticity (contours, 1, 2, and 4 PVU) and MTSAT-1R brightness temperature difference image (shading). The black dot denotes the vort-max position. The vertical cross section following the red line, which transverses the region with deep convection, is illustrated on the right column. (b, d) Ertel potential vorticity (black contours, 0.4, 1 and 2 PVU), potential temperature (gray contours, K) and quasi-geostrophic vertical velocity ω (shading, 10^{-1} Pa s^{-1}) cross section. The triangle indicates the center of the red line, that of (b) and (d) having the same longitude and latitude with the vort-max position of (a) and (c), respectively. The time of top figures are 1200 UTC on October 28 and that of bottom figures are at 1800 UTC on October 30.

associated with the occurrence of the TUTT (Figure 34a) before the onset of the pre-Peipah system. As anticipated in the quasi-geostrophic dynamics, the PV intrusion modulated both static stability and vertical motion in the entire troposphere (Figure 36a, Figure 37a, b). Specifically, the reduced static stability is identified with the high CAPE value in Figure 36a in the southern edge of the PV tongue. The cross section in Figure 37b also shows strengthened static stability in the upper troposphere (see stronger potential temperature gradient around 158°E and 500–300 hPa in Figure 37b) and weakened in the lower-to-mid troposphere (around 158°E and 800–600-hPa in Figure 37b). Moreover, the quasi-geostrophic ascent observed throughout the entire troposphere (Figure 37b) is located in the southeast edge of the PV trough where deep convection appears (Figure 37a). Overall, both the wide area of destabilization (i.e., the area with high CAPE value) and the deep quasi-geostrophic ascent explain the development of deep convection to the south of the TUTT on 28 October.

The structure of subtropical cyclone shown in Figure 37b is further analyzed by calculating the frontogenesis $[\mathrm{F} = \frac{\mathrm{d}}{\mathrm{dt}}(\nabla\theta)]$, because the deep convection area resembles a cold front. The result verifies that the frontogenesis shows no correspondence with the region of deep convection (Figure 38). Also, the examination of temperature, potential temperature, equivalent potential temperature, and specific humidity shows that the equivalent potential temperature field is more associated with specific humidity distribution rather than temperature distribution (Figure 39). Also, moisture convergence in the lower troposphere is evident

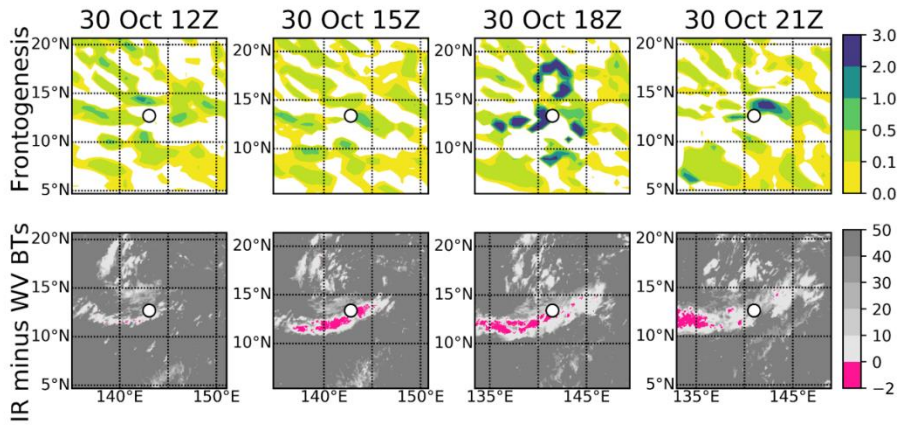

Figure 38. (Top row) Calculation of frontogenesis function and (bottom row) MTSAT-1R brightness temperature difference image (IR minus WV; shading, K) about the vort-max position plotted in three-hourly from October 30 12Z to 21Z.

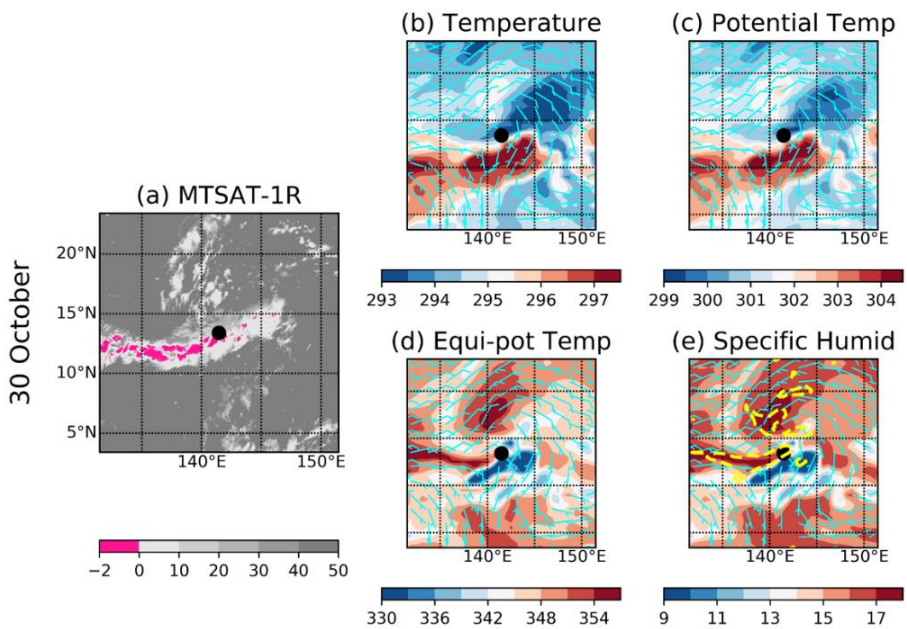

Figure 39. (a) MTSAT-1R brightness temperature difference image (IR minus WV; shading, K). (b–e) The 925 hPa (b) temperature, (c) potential temperature, (d) equivalent potential temperature, and (e) specific humidity (shading, K for temperatures and 10^{-5} g kg^{-1} for specific humidity) with horizontal wind vectors. Dashed yellow contours in (e) indicates the 925 hPa moisture flux divergence of −20 g kg^{-1} s^{-1}. The black dots denote the vortex center.

(Figure 39e). However, the calculation of quasi-geostrophic ascent/descent shows significant quasi-geostrophic updrafts over the deep convection (Figure 38d), this study concluded that the deep convection on 30 October is driven by quasi-geostrophic dynamics, not by the frontogenesis.

On the following days, the amplified Rossby wave trough penetrated deep into the tropics (29 October, not shown) and subsequently cut off (30 October, 141.5°E and 13.4°N in Figure 36b). In this period, the narrow and long deep convection (Figure 37c) occurs at the southern periphery of the cut-off PV. The calculated CAPE value is larger than 2,000 J kg^{-1} around the region where deep convection occurs, and vertical gradient of potential temperature in the cross section decreases showing the reduced static stability (around 11.5°N and 900–600 hPa in Figure 37d). Moreover, the calculated quasi-geostrophic vertical motion indicates strong ascent over the region of deep convection. This deep convection persisted for about 6 h (Figure 33d) and the warm-core feature of the precursor TC becomes clearer on 1 November (Figure 34l).

On 1 and 3 November, a completely detached cutoff low is weakening gradually (Figure 36c, d), as also shown in weakening of the upper tropospheric relative vorticity (Figure 33c). The quasi-geostrophic vertical motion significantly weakens as well (not shown). The location of maximum relative vorticity subsequently changes from upper troposphere into lower troposphere as deep convection becomes diurnal (Figure 33b, c) in the environment of high CAPE (Figure 36c, d). This vertical redistribution of vorticity may possibly be explained by diabatic heating of

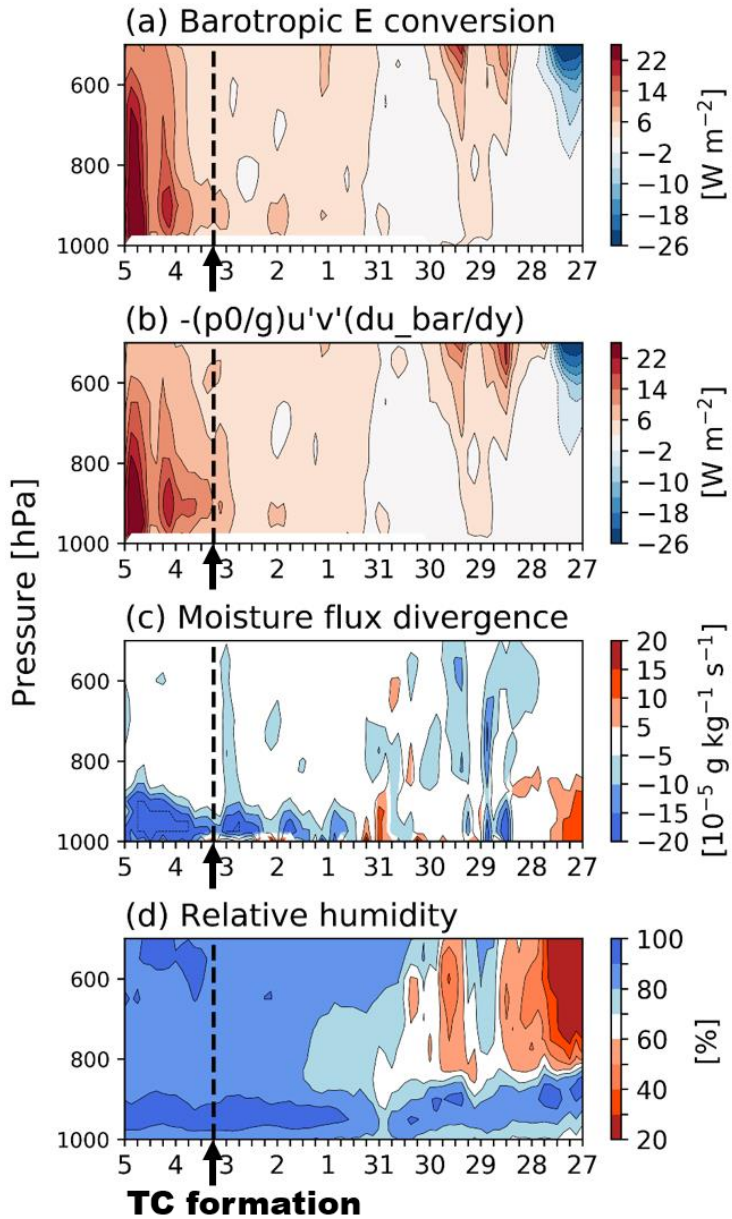

Figure 40. Time-height diagram of (a) barotropic energy conversion (W m^{-2}), (b) the term with meridional gradient of zonal wind ($-\frac{p_0}{g}u'v'\partial\bar{u}/\partial y$) in Eq 3 (W m^{-2}), (c) moisture flux divergence (10^{-5} g kg^{-1} s^{-1}), and (d) relative humidity (%) averaged within a 500 km radius from the vort-max position. The vertical dashed line indicates the date of Peipah formation. Note that zonal axis (time) in (b–c) is reversed.

deep convection as Raymond (1992) demonstrated that PV increases (decreases) below (above) the level of maximum diabatic heating in non-advective PV tendency equation.

On 31 October to 2 November, the warm-core low is clearly identified (Figure 34l, o), and the lower tropospheric vortex gradually strengthens (Figure 33b). In this section, such process is examined in terms of the BTEC (Figure 40a) and moisture flux divergence (Figure 40c). The BTEC from MKE to EKE is calculated as explained in section 2.2.5 and Eq 3.

The neutral value of 1,000 to 500 hPa BTEC from 27–29 October began to increase on 31 October (Figure 40a). The conversion from MKE into EKE was closely correlated with intensification of relative vorticity (Figure 33b). Here, the increasing BTEC was mainly due to the term including the meridional gradient of zonal wind ($-\frac{p_0}{g}u'v'\partial\bar{u}/\partial y$) in Eq 3 (Figure 40b); that is, the slowly varying easterly winds favored the eddy growth. In fact, the pre-TC vorticity entered the region of cyclonic shear (increasing mean easterly with latitude; positive values in Figure 41) since 29 October and the interaction between the pre-TC vorticity and environment become favorable for eddy growth since 31 October (Figure 41).

Moisture flux convergence (negative values in Figure 40c) in the lower troposphere became diurnally periodic on late 31 October, in contrast to previously less organized distributions. The moisture flux convergence was likely a result of surface vortex strengthening. Enhanced surface winds leads to an increase in surface moisture and heat fluxes (Emanuel 1986), especially over the warm ocean (>26 °C,

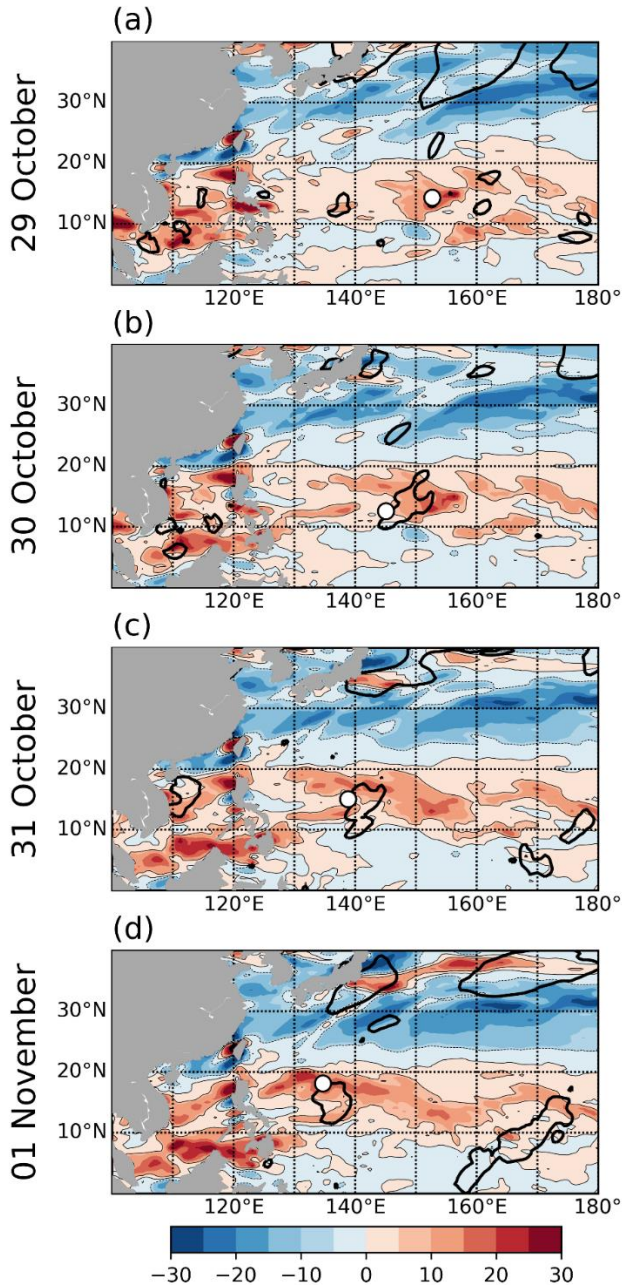

Figure 41. The 925 hPa meridional gradient of zonal wind ($-\partial\bar{u}/\partial y$; shadings, 10^{-6} s^{-1}) and the product of the horizontal wind anomalies ($u'v'$; contour, 20 m^2 s^{-1}) at 0600 UTC on (a) October 29, (b) October 30, (c) October 31, and (d) November 1. The dots denote the vort-max position of pre-TC.

Figure 33a) and with weak vertical wind shear (<16 m s^{-1}, Figure 33c). As the moisture flux convergence increases, the relative humidity in the lower troposphere increases as well, forming a favorable environment for deep convection by substantial moistening. Prominent moisture flux convergence and associated surface latent heat fluxes would have contributed to deep convective activities since 1 November. As the remnant of cutoff PV remains in the upper troposphere (evident Figure 36c and strong upper tropospheric relative vorticity in Figure 33b), the deep convective activity may slowly increase during 1–2 November. After the upper tropospheric vorticity decays, the area of deep convection increases rapidly and Peipah develops.

To summarize, this case study suggests that the BTEC enhancing EKE and relative vorticity is among the possible factors for enhancing moisture flux convergence. Nevertheless, more complex factors leading to the increase in moisture flux convergence may exist, for example, shallow to moderate convection (Figure 34h, k) that brings moisture flux convergence to intensify the low-level vorticity (Wang 2014). The eventual maintenance of moisture flux convergence and positive feedback between the vortex strength and the latent heat fluxes after this day would have resulted in the formation of Peipah.

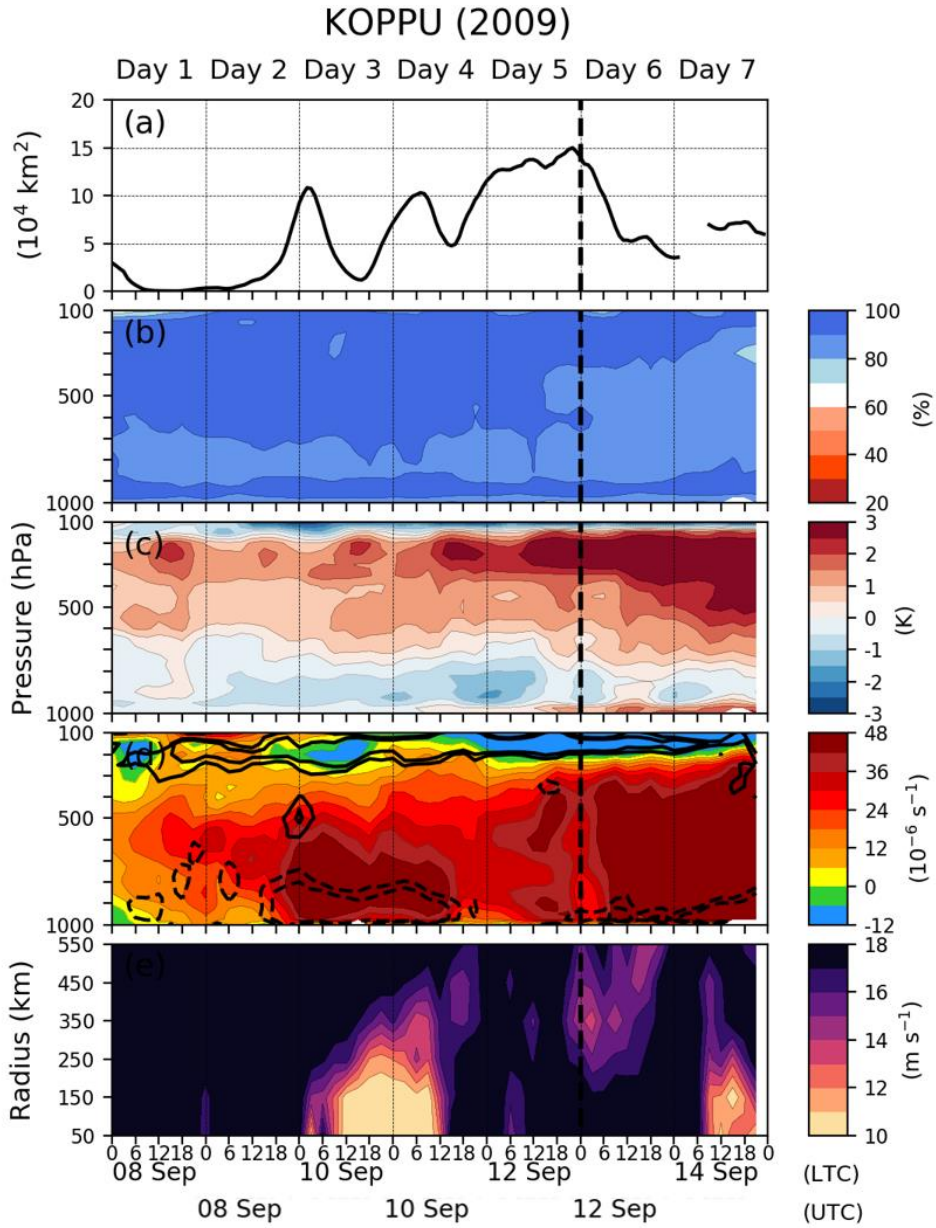

Figure 42. The same as Figure 16 but for Koppu (2009) case.

3.3.3. Case study on TC Koppu (2009)

As shown in Figure 26d, pre-Koppu is not traced back to strong PV in the upper troposphere whereas mCB is not observed prior to its formation. This case is chosen as representative case for a case study of group D_mixed. Overall analysis is consistent with the case study of Hagupit. The deep convection time series is shown in Figure 42a. As in the composite time series (Figure 29f), mCB-like diurnal fluctuation is observed in pre-Koppu. However, the magnitudes of CB features do not satisfy mCB definition thresholds. The relative humidity reaches over 80% throughout the entire troposphere (Figure 42b) and the warm core anomaly is clearly featured since Day 1 (Figure 42c). On Day 1, the relative vorticity maximum is located in the mid-troposphere around 500-to-600-hPa pressure height. The vorticity maximum locates in the lower troposphere since Day 3. The vertical wind shear magnitude is very high (> 18 m s^{-1}), which is the only exception feature that does not represent the group D_mixed.

The following analysis with scale-decomposition also shows consistent result with composite analysis (Figure 43). The synoptic-scale distribution of low-level relative vorticity presents a pair of anticyclone and cyclone. The large area of positive relative vorticity is noticeable which extends about 10° in zonal scale. The mid-and-lower tropospheric large-scale relative vorticity presents elongated positive relative vorticity area surrounded by horizonal wind shear, i.e., southeasterly to the north of pre-TC and northwesterly to the south of pre-TC. The magnitude of large-scale vertical wind shear around pre-TC is stronger at mid-to-upper troposphere,

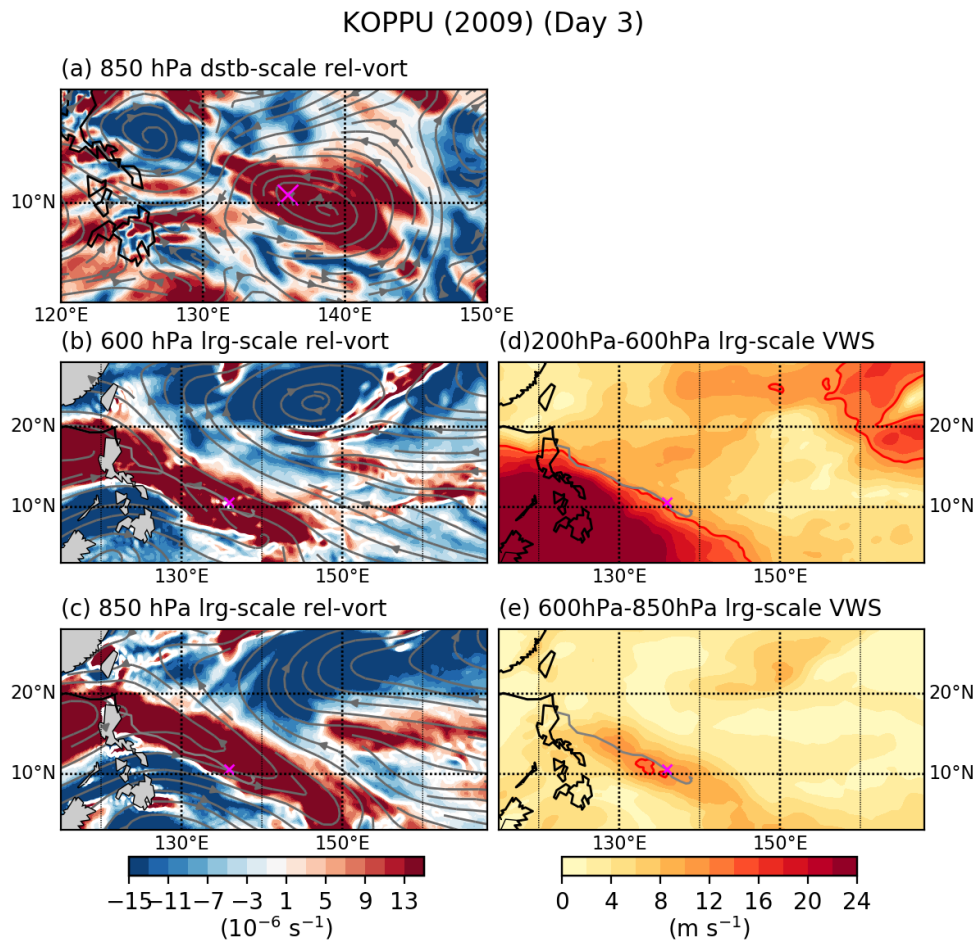

Figure 43. The same as Figure 23 but for Koppu (2009) case.

compared to mid-to-lower troposphere. In the mid-to-upper troposphere, the vertical wind shear contrasts in the either side of pre-TC track.

3.3.4. Schematic diagram

By integrating the composite analysis on D_pv and the cases study on Peipah, the formation pathway of D_pv can be summarized in three steps, especially in terms of convective updrafts (Figure 44). Step 1 accounts for the quasi-geostrophic-forcing for ascent induce by TUTT and initiation of a surface extratropical disturbance. The TUTT in the WNP formed through PV intrusion from the stratosphere. This also explains the presence of a vorticity maximum in the upper troposphere several days before TC formation. As TUTT drags cold air from the higher latitudes the negative temperature anomaly is identified at this time period. Step 2 includes a transient state when the cold-core disturbance is transformed into a warm-core disturbance in the tropics. At this moment, the PV trough in the upper troposphere breaks anti-cyclonically and forms a cut-off low, or a TUTT-cell. The transition is supported by the latent heat release via another deep convection associated with quasi-geostrophic-forcing for ascent induced by the TUTT-cell. In Step 3, the lower-tropospheric vorticity grows via BTEC. The kinetic energy from large-scale background flow fed the pre-TC vorticity to grow. As the lower-tropospheric vorticity intensifies over warm ocean surfaces, surface convergence of moisture favors deep convection. The subsequent accumulation of latent heat diabatically redistributes PV in the troposphere and led to the formation of Peipah.

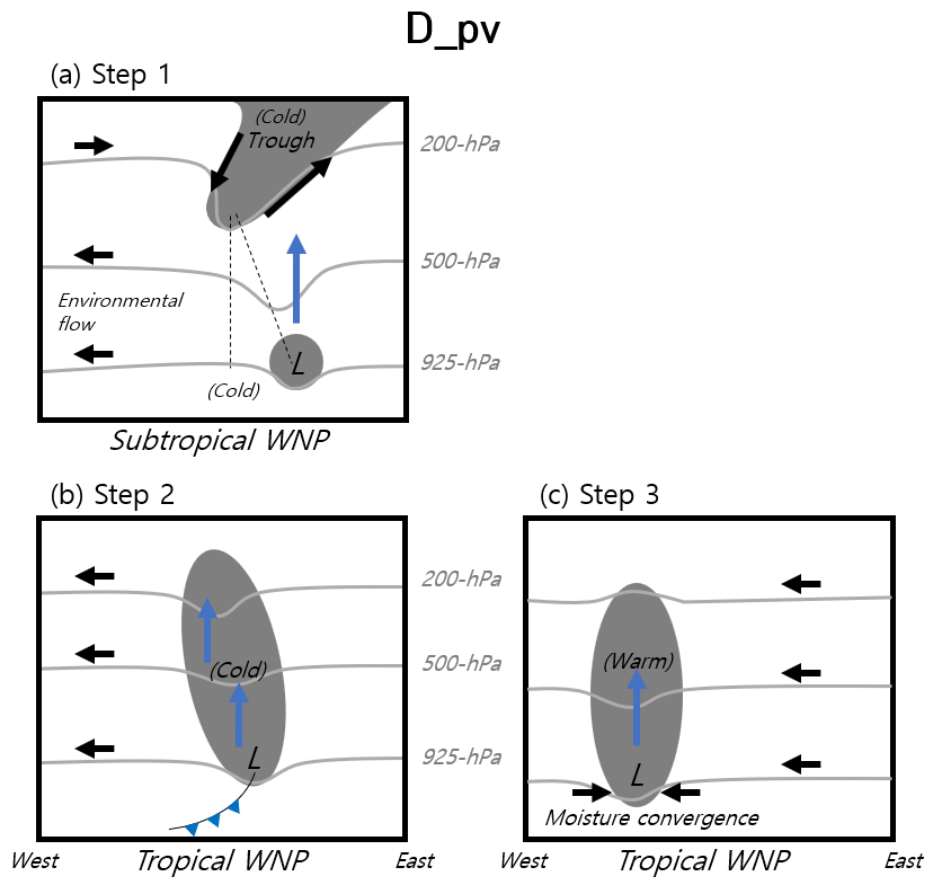

Figure 44. Schematic diagram of the formation of Peipah through a tropical transition over the WNP. The dark gray shadings and gray lines indicate cyclonic circulation and geopotential height, respectively. Black arrows are flow direction while blue arrows are convective ascent. (a) Step 1: Initiation of lower-tropospheric low via quasi-geostrophic ascent induced by an upper-tropospheric trough over the subtropics. (b) Step 2: An extratropical disturbance has formed after step 1 and another quasi-geostrophic ascent takes places. (c) Step 3: Formation of TC (with the strength of tropical depression) by low-tropospheric moisture convergence over the tropics as the eddy kinetic energy increases by obtaining barotropic energy from the mean flow.

For D_mixed, the composite analysis and the case study on Koppu show that overall formation pathway resembles that of D_mCB. The series of mCB-like deep convection occurs prior to their formation but smaller in CB feature magnitudes. For the large-scale environment, favorable thermodynamic and dynamic environment are found, only except for substantial vertical wind shear in some cases. Also, pre-TCs are located over the elongated area of positive large-scale relative vorticity surrounded by horizonal wind shear. For the synoptic scale, the anticyclone('A')-cyclone('C')-anticyclone wave train are found, as did in D_mCB. The location of positive vorticity maximum, however, is located in the mid-troposphere, which is different from D_mCB.

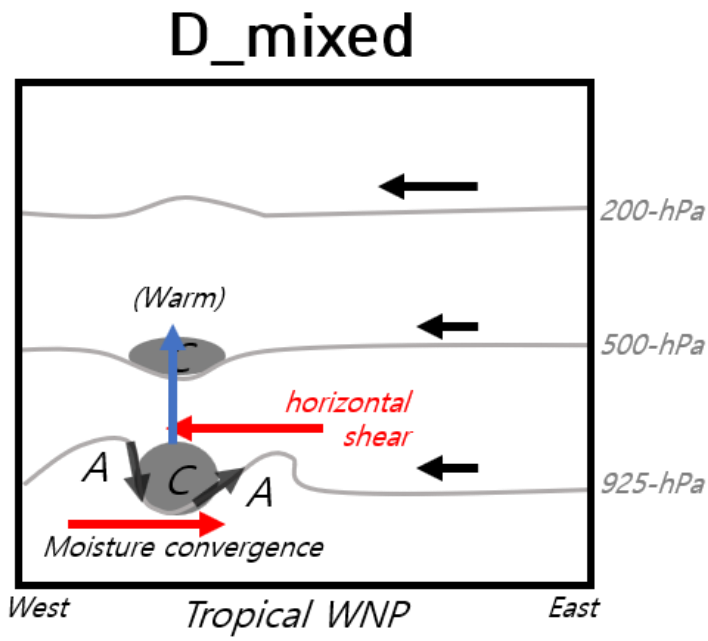

Figure 45. Schematic diagram of TC formation pathway of D_mixed. Overall characteristics resembles D_mCB. Here, however, the relative vorticity magnitude in the mid-troposphere is similar to that in the lower-troposphere, and the large-scale horizontal shear is observed around the disturbance.

4. Discussion

4.1. The role of mCB as tropical cyclogenesis precursor

Tropical disturbance classification with mCB in section 3.1.3 revealed 54 developing TCs and 53 non-developing TCs to accompany mCB. In this section the validity of mCB as one of TC precursors will be discussed by taking two methods.

Firstly, simple examination is applied to filter non-developing disturbances before checking the occurrence of mCB. Because, the sample size of developing and non-developing in this study are not really fair, as there exist more than 4 times as many non-developing samples (383), compared to the developing samples (80). Thus, many of the non-developing disturbances lack any qualities that could be considered favorable for development.

Here, the “strongest” 80 non-developing disturbances are selected and compared with developing disturbances, hoping this way being more useful for the forecasting implications of this study. In terms of the “strongest”, this study examined two types; one type is top 80 non-developing disturbances sorted by strength of expanded deep convection area (ΔA) on Day 4 (type 1); the other type is top 80 non-developing disturbances sorted by strength of lower-tropospheric (925–850 hPa) relative vorticity on Day 4 (type 2). The definition of two types considered their thresholds satisfactory among all developing disturbances. After selecting top 80 non-developing disturbance, they are classified according to mCB

Table 8. Contingency table of developing and non-developing disturbances among different samples.

	Developing disturbance	Non-developing disturbance		
		Raw	Type 1	Type 2
With mCB	54	53	16	25
Without mCB	26	330	64	55
	80	383	80	80

occurrence (Table 8).

Analysis of type 1 shows that 20% of non-developing disturbances have mCB. Comparison of convective-environmental evolution between developing and non-developing disturbances with mCB shows consistent results with the earlier analysis; developing disturbance with mCB tends to have weaker vertical wind shear on Days 1 and 2 and begins to have greater mid-to-lower-tropospheric relative vorticity on Day 3.

Analysis of type 2 shows that 31.25% of non-developing disturbances have mCB. Comparison of the developing disturbances against non-developing ones with mCB does not show any significant differences in convective-environmental evolution. This implies that using relative vorticity as a primary decisive attribute to classify developing or non-developing disturbance is less effective than using expanded convection area.

However, current simple inspection limits understanding on the relative importance of mCB among other attributes, for example expanded deep convection area (ΔA) or strength of lower-tropospheric (925–850 hPa) relative vorticity. Thus, as a second method, the decision tree algorithm, which explained in section 2.2.7, is applied on various attributes, including mCB, to discuss about relative importance among them.

The predictors trained in the decision tree is listed in Table 9 which encompasses the previous findings. Two decision tree models, “Day 3” model and “Day 4” model, are designed by training different datasets. The “Day 3” model

Table 9. The list of variables and their descriptions trained in decision tree of "Day 3" model. That of "Day 4" model is written inside the parenthesis. For developing disturbances, same variables but on different day is used for data augmentation.

Variable	Description	Augmentation
RH850	Mean 850-hPa relative humidity (%) on Day 3(4)	Same value on Day 4(5)
Relv850meso	Mean 850-hPa relative vorticity (< 2.5 days, 10^{-6} s^{-1}) on Day 3(4)	
Relv850synop	Mean 850-hPa relative vorticity (2.5-to-9 days, 10^{-6} s^{-1}) on Day 3(4)	
Relv850large	Mean 850-hPa relative vorticity (> 9 days, 10^{-6} s^{-1}) on Day 3(4)	
VWSlarge	Mean vertical wind shear (> 9 days, m s^{-1}) on Day 3(4)	
PV200	Maximum 200-hPa potential vorticity (PVU) during Day 1-3(1-4)	Same value during Day 1-4(1-5)
mCB	Existence of mCB during Day 1-5 (0=no, 1=mCB)	Same value
maxA	Maximum of max(A) (10^4 km^2) during Day 1-3(1-4)	Same value during Day 1-4(1-5)
dAdt	Maximum of dAdt (10^3 km^2 h^{-1}) during Day 1-3(1-4)	
dA	Maximum of dA (10^4 km^2) during Day 1-3(1-4)	

dataset consists of each variable on Day 3 among 80 developing and 383 non-developing disturbances. As the size of developing dataset is too small, each variable on Day 4 among 80 developing disturbances are added. Thus, “Day 3” model predicts TC formation either on Day 3 or Day 4. In the same way, “Day 4” model dataset is prepared, making the “Day 4” model to predict TC formation either on Day 4 or Day 5.

For each model, the minimum impurity thresholds are set to be 0.0005, 0.001, 0.002, 0.005, 0.01, 0.02, and 0.05, and the model accuracy for each impurity threshold are calculated and shown in Figure 46. As expected, overall accuracy is higher in “Day 4” model than in “Day 3” model. When the minimum impurity thresholds are larger than or equal to 0.02, the performance of two models are equal. For “Day 3” model, the lower accuracy is found in lower thresholds of minimum impurity thresholds. For “Day 4” model, the highest accuracy (87.7%) is obtained when the minimum impurity threshold is equal to 0.002 (marked in triangle in Figure 46). However, in this case, the number of terminal nodes is too large (9), making the tree too complex and difficult to explain. As a subjective notion, the optimal decision tree model is determined as when the minimum impurity threshold is set to 0.01 (marked in star in Figure 46). In this case, the accuracy is 85.3% and the number of terminal nodes is 5, making easy to understand (Figure 47).

According to Figure 47, a tropical disturbance is first classified according to the occurrence of mCB. If the disturbance has mCB (a “False” branch in the first terminal node in Figure 47), the magnitude of 850 hPa relative vorticity in synoptic

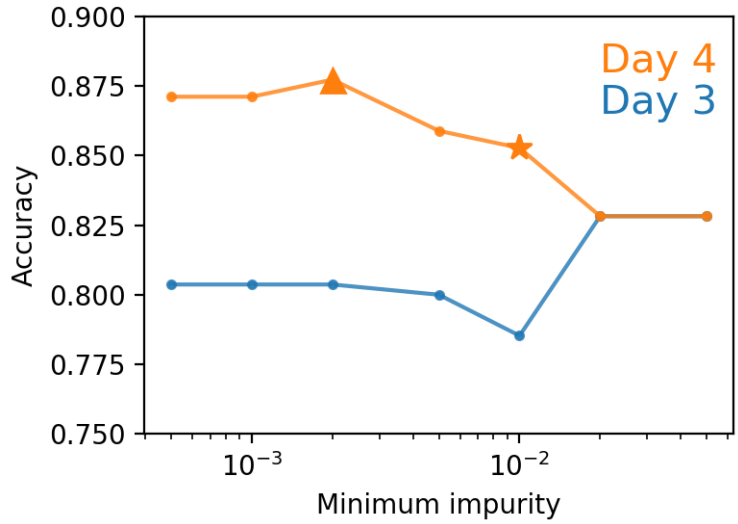

Figure 46. The accuracy distributions according to different threshold of minimum impurity of "Day 3" and "Day 4" models. The triangle indicates the highest accuracy and the star indicates the model with optimal terminal nodes.

time scale is examined. If the magnitude exceeds 11.23×10^{-6} s^{-1}, TC formation is forecasted. This is consistent with the significant difference in 850 hPa relative vorticity which was already found in section 3. If not, the magnitude of 850 hPa relative vorticity in synoptic time scale as well as the maximum deep convection area are adopted as thresholds for TC prediction.

If a disturbance does not have mCB (a "True" branch in the first terminal node in Figure 47), the magnitude of 850 hPa relative vorticity in synoptic time scale is examined with different threshold value. If the magnitude is under 7.548×10^{-6} s^{-1}, non-formation is forecasted. If the magnitude exceeds that value, disturbance having maximum deep convection area larger than 799.254×10^{4} km^2 is predicted for TC formation.

To summarize, the decision tree analysis verifies the hierarchical relationship among the attributes that the mCB provides the largest information gain in TC genesis prediction, and it is followed by 850 hPa relative vorticity in synoptic scale, maximum deep convection area and 850 hPa relative vorticity in large scale. The last two attributes seem to be in equal hierarchy.

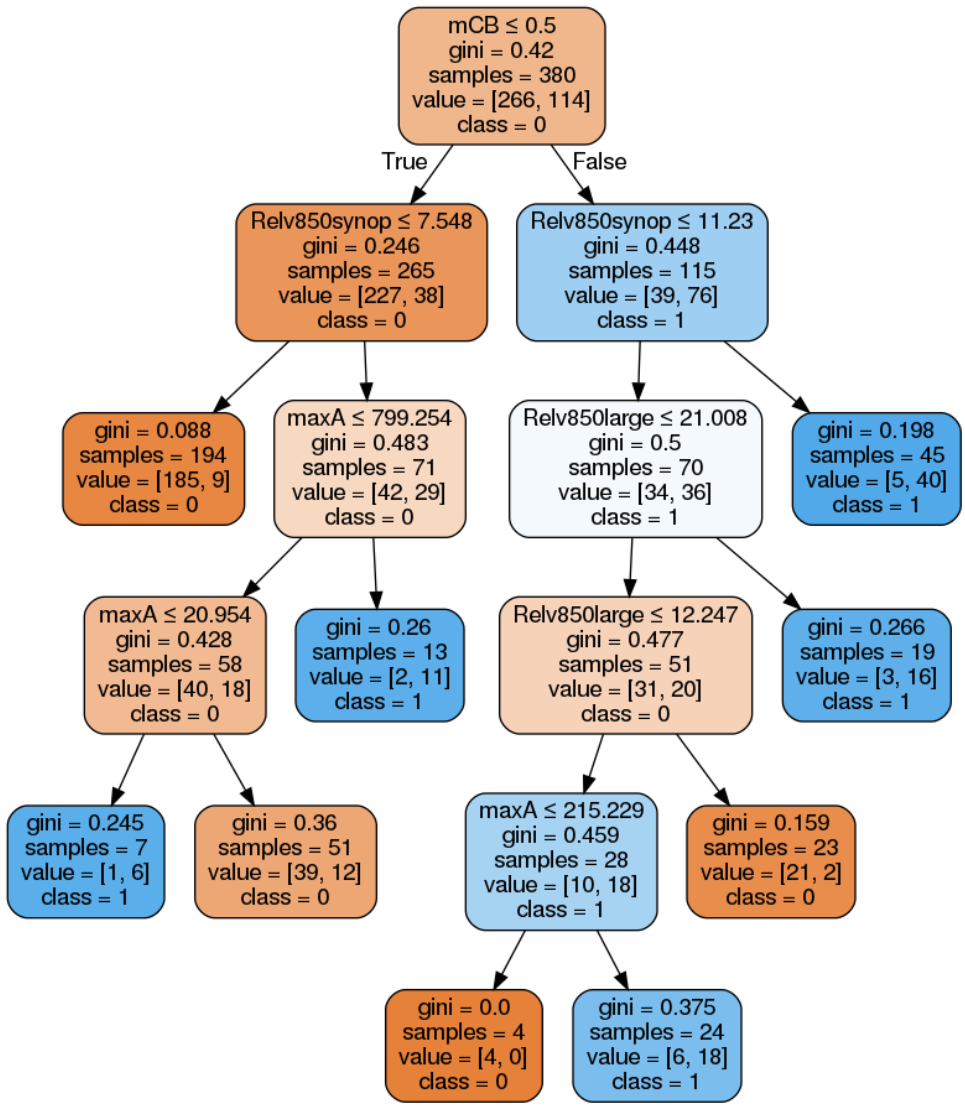

Figure 47. A decision tree with the minimum impurity threshold equal to 0.01 and the accuracy equal to 85.3%. In this chart, each internal node has a decision rule that splits the data. Blue boxes are forecasted as a TC developing disturbances, when the orange boxes are forecasted as non-developing disturbances.

4.2. Potential vorticity intrusion and tropical cyclogenesis

As the 15% of TC formation during 2007–2009, i.e., 12 out of 80 TCs, are associated with PV intrusion in the WNP, this section will discuss about the definition of TC formation influenced by PV intrusion. Yet, such formation pathway has not been documented as much as in the North Atlantic (Table 10). Therefore, if someone can provide a clear algorithm to determine such TC formation pathway, it would be useful in further investigation in various time scales.

The necessity is raised because when comparing D_pv members in this study with the classification according to McTaggart-Cowan et al. (2013), mismatches are frequently observed (T. J. Galarneau, personally obtained their dataset, 28 February 2020). McTaggart-Cowan et al. (2013) refers a TC formation influenced by PV intruison as baroclinic TC formaiton pathway. Aong 12 TCs found in this study, only 5 TCs are classfied as having baroclinic formation pathway (Table 11). The major reason is found to be difference in investigation time domain. McTaggart-Cowan et al. (2013) investigates since 12 hours before tropical storm (~17.5 m s^{-1}) formation, whereas this study investigates since 5 days before tropical depression (13–17 m s^{-1}) formation. Thus, if PV intrusion initiates pre-TC disturbance more than 12 hours before tropical storm formation, the TC is considered as non-baroclinic TC formation case in McTaggart-Cowan et al. (2013), but as D_pv case in this study. Therefore, in Table 11, TC formation pathway of 7 cases, classified as non-baroclinic in McTaggart-Cowan et al. (2013), are thought to be baroclinic in the earlier stage, but

Table 10. Summary of documentations regarding tropical transition in the western North Pacific and in the North Atlantic.

Western North Pacific	
(Sadler 1975, 1976, 1978)	Documentation on TUTT-induced TC formations
(Briegel and Frank 1997)	Identification on upper-tropospheric troughs near TC formation
(McTaggart-Cowan et al. 2013)	Climate study on baroclinic TC formation (~19% during 1948–2010)
North Atlantic	
(Hess et al. 1995)	Climate study on baroclinicallly influenced hurricane formation (~51% 1950–1993)
(Bracken and Bosart 2000)	Report the upper-tropospheric trough over lower-tropospheric cyclonic vorticity feature as a common feature during TC formations
(Davis and Bosart 2001)	Case study on baroclinic formation of a hurricane
(Davis and Bosart 2003)	Thorough documentation on baroclinically induced TC genesis
(Davis and Bosart 2004)	Thorough documentation on tropical transition
(Davis and Bosart 2006)	Case study on a hurricane formation from an extratropical precursor
(McTaggart-Cowan et al. 2008, 2013)	Climate study on baroclinic TC formation (~47% during 1948–2010)
(Galarneau et al. 2015)	Mechanical case and climate study on TC genesis near upper-tropospheric PV streamers
(Bentley et al. 2016)	Dynamically based climate study on tropical transition
(Bentley et al. 2017)	Climate study on TC formations influenced by anticyclonic (Rossby) wave breaking

non-baroclnic in the latter part, i.e., half-baroclinic. Likewias, TC formation pathway of 5 cases, classified also as baroclinic in McTaggart-Cowan et al. (2013), are thought to be full-baroclinic. Thus, more detailed classification method which can distintuish non-baroclinic, half-baroclinic, full-baroclinic pathways, will benefit many researchers.

Table 11. A list of D_pv with its classification by McTaggart-Cowan et al. (2013).

Year	List of D_pv	McTaggart-Cowan et al. (2013)
2007	USAGI	Non-baroclinic
	KROSA	Baroclinic
	PEIPAH	Non-baroclinic
2008	NURI	Non-baroclinic
	16W_NONAME	Baroclinic
	17W_NONAME	Baroclinic
	JANGMI	Non-baroclinic
	BAVI	Baroclinic
	HAISHEN	Non-baroclinic
	DOLPHIN	Baroclinic
2009	NANGKA	Non-baroclinic
	LUPIT	Non-baroclinic

5. Conclusion

In the report of the ninth International Workshop on Tropical Cyclones, the non-linear nature of TC genesis is stated as an interplay of diverse scales of processes, from convective scale to large environmental scale. Dunkerton et al. (2009) also describes that TC formations are associated with the collision between upscale aggregation of mesoscale convective vorticities and the energy breakdown larger-scale environments. In this section, the findings of this thesis will be summarized in terms of such scale interactions.

As TC formation accompanies gradual organization of mesoscale convective cloud clusters, a series of diurnal convective bursts more than two consecutive days (i.e., mCB) are frequently observed from TC precursor disturbances and known as a typical prelude before TC genesis. Such a series of deep convective activity likely favors the aggregation of vortex within the synoptic-scale circulation as the strong convective updrafts intensifies vorticity via vertical stretching. However, there was lack of documentation providing the quantitative information about mCB frequency on pre-TCs, or its possible role as one of TC precursor. Here, we examined the occurrence of mCB among 80 TC developing and 383 non-developing disturbances, that 67.5% total TC formations are associated with mCB, whereas mCB is also found in 13.8% of non-developing disturbances. When considering mCB as a brief manifestation of meso-scale convective cloud organization, the difference between development and non-development of TC is attributed to the larger-scale factor, i.e. the strength of environmental vertical wind shear and the synoptic-scale factor, i.e.,

a series of anticyclone-cyclone-anticyclone around the pre-TC disturbance. In other words, even though multiple occurrence of meso-scale convective bursts aggregates the vortex together, it is difficult for a tropical disturbance to develop into TC without favorable synoptic-scale and large-scale conditions.

We further assess the TC formation pathway of a portion of developing disturbances without mCB (32.5% of total developing disturbances). When considering the absence of regular diurnal convective bursts, which is known to help vortex aggregation, the TC vortex initiation among this group is thought to be engaged with some ambient external dynamic factors: one of them is found to be PV intrusion from the extra-tropics. As strong PV streamer intrudes into the tropics, an extratropical low-pressure system is induced by quasi-geostrophic forcing. Consequently, barotropic energy conversion from the mean kinetic energy in the large-scale environment into eddy kinetic energy helped the transition of extratropical low to tropical low-pressure system, a TC. In this case, the downscale energy cascade from large-scale environment seems to fill the deficiency from upscale cascade via convective activities.

Additional analysis adopting decision tree algorithm specified that mCB can be regarded as a primary classification standard for TC formation prediction. Yet, mCB cannot be used as a single standard, but with 850 hPa relative vorticity in synoptic scale, maximum deep convection area and 850 hPa relative vorticity in large scale. The last two attributes seem to be in equal hierarchy or in equal importance.

Despite the particularized investigation on each group of development and non-

development disturbances, there remains many possible future works. Especially, current result suggests a necessity to develop an integrated algorithm thoroughly determining non-baroclinic, half-baroclinic, full-baroclinic TC formation pathways. The development of such algorithm will enable many studies encompassing various time scale including interannual an long-term time scale.

References

Bentley, A. M., and N. D. Metz, 2016: Tropical Transition of an Unnamed, High-Latitude, Tropical Cyclone over the Eastern North Pacific. *Mon. Weather Rev.*, **144**, 713–736, https://doi.org/10.1175/MWR-D-15-0213.1.

——, D. Keyser, and L. F. Bosart, 2016: A Dynamically Based Climatology of Subtropical Cyclones that Undergo Tropical Transition in the North Atlantic Basin. *Mon. Weather Rev.*, **144**, 2049–2068, https://doi.org/10.1175/MWR-D-15-0251.1.

——, L. F. Bosart, and D. Keyser, 2017: Upper-Tropospheric Precursors to the Formation of Subtropical Cyclones that Undergo Tropical Transition in the North Atlantic Basin. *Mon. Weather Rev.*, **145**, 503–520, https://doi.org/10.1175/MWR-D-16-0263.1.

Bessho, K., Y. Tanaka, and T. Nakazawa, 2001: Validation of GMS brightness temperatrue difference technique for estimate of cumulonimbus in typhoon by TRMM PR data. Madison, Wisconsin, paper presented at 11th Conf. on Satellite Meteorology and Oceanography, Amer. Meteor. Soc., 3.26.

Bister, M., and K. A. Emanuel, 1997: The genesis of hurricane Guillermo: TEXMEX analyses and a modeling study. *Mon. Weather Rev.*, **125**, 2662–2682, https://doi.org/10.1175/1520-0493(1997)125<2662:TGOHGT>2.0.CO;2.

Bluestein, H. B., 1993: *Synoptic-Dynamic Meteorology in Mid latitudes*. Oxford University Press, 594 pp.

Bosilovich, M. G., R. Lucchesi, and M. Suarez, 2016: *MERRA-2: File Specification*. 73 pp. http://gmao.gsfc.nasa.gov/pubs/office_notes.

Bracken, W. E., and L. F. Bosart, 2000: The Role of Synoptic-Scale Flow during Tropical Cyclogenesis over the North Atlantic Ocean. *Mon. Weather Rev.*, **128**, 353, https://doi.org/10.1175/1520-0493(2000)128<0353:TROSSF>2.0.CO;2.

Briegel, L. M., and W. M. Frank, 1997: Large-Scale Influences on Tropical Cyclogenesis in the Western North Pacific. *Mon. Weather Rev.*, **125**, 1397–1413, https://doi.org/10.1175/1520-0493(1997)125<1397:LSIOTC>2.0.CO;2.

Cai, M., S. Yang, H. M. Van Den Dool, and V. E. Kousky, 2007: Dynamical implications of the orientation of atmospheric eddies: a local energetics perspective. *Tellus A Dyn. Meteorol. Oceanogr.*, **59**, 127–140, https://doi.org/10.1111/j.1600-0870.2006.00213.x.

Chang, M., C.-H. Ho, M.-S. Park, J. Kim, and M.-H. Ahn, 2017: Multiday evolution of convective bursts during western North Pacific tropical cyclone development and nondevelopment using geostationary satellite measurements. *J. Geophys. Res. Atmos.*, **122**, 1635–1649, https://doi.org/10.1002/2016JD025535.

Cheung, H. M., C. H. Ho, J. G. Jhun, D. S. R. Park, and S. Yang, 2018: Tropical cyclone signals on rainfall distribution during strong vs. weak Changma/Baiu years. *Clim. Dyn.*, **51**, 2311–2320, https://doi.org/10.1007/s00382-017-4014-1.

Cressman, G. P., 1961: A DIAGNOSTIC STUDY OF MID-TROPOSPHERIC DEVELOPMENT. *Mon. Weather Rev.*, **89**, 74–82, https://doi.org/10.1175/1520-0493(1961)089<0074:ADSOMD>2.0.CO;2.

Davis, C. A., and L. F. Bosart, 2001: Numerical simulations of the genesis of Hurricane Diana (1984). Part I: Control simulation. *Mon. Weather Rev.*,

129, 1859–1881, https://doi.org/10.1175/1520-0493(2001)129<1859:NSOTGO>2.0.CO;2.

Davis, C. A., and L. F. Bosart, 2003: Baroclinically Induced Tropical Cyclogenesis. *Mon. Weather Rev.*, **131**, 2730–2747, https://doi.org/10.1175/1520-0493(2003)131<2730:BITC>2.0.CO;2.

——, and ——, 2004: The TT Problem: Forecasting the Tropical Transition of Cyclones. *Bull. Am. Meteorol. Soc.*, **85**, 1657–1662, https://doi.org/10.1175/BAMS-85-11-1657.

——, and ——, 2006: The formation of hurricaneHumberto (2001): The importance of extra-tropical precursors. *Q. J. R. Meteorol. Soc.*, **132**, 2055–2085, https://doi.org/10.1256/qj.05.42.

——, and D. A. Ahijevych, 2012: Mesoscale Structural Evolution of Three Tropical Weather Systems Observed during PREDICT. *J. Atmos. Sci.*, **69**, 1284–1305, https://doi.org/10.1175/JAS-D-11-0225.1.

Duchon, C. E., 1979: Lanczos Filtering in One and Two Dimensions. *J. Appl. Meteorol.*, **18**, 1016–1022, https://doi.org/10.1175/1520-0450(1979)018<1016:LFIOAT>2.0.CO;2.

Dunkerton, T. J., M. T. Montgomery, and Z. Wang, 2008: Tropical cyclogenesis in a tropical wave critical layer: easterly waves. *Atmos. Chem. Phys. Discuss.*, **8**, 11149–11292, https://doi.org/10.5194/acpd-8-11149-2008.

Emanuel, K. A., 1986: An Air-Sea Interaction Theory for Tropical Cyclones. Part I: Steady-State Maintenance. *J. Atmos. Sci.*, **43**, 585–605, https://doi.org/10.1175/1520-0469(1986)043<0585:AASITF>2.0.CO;2.

Fischer, M. S., B. H. Tang, and K. L. Corbosiero, 2017: Assessing the Influence of Upper-Tropospheric Troughs on Tropical Cyclone Intensification Rates after Genesis. *Mon. Weather Rev.*, **145**, 1295–1313,

https://doi.org/10.1175/MWR-D-16-0275.1.

Funatsu, B. M., and D. W. Waugh, 2008: Connections between potential vorticity intrusions and convection in the eastern Tropical Pacific. *J. Atmos. Sci.*, **65**, 987–1002, https://doi.org/10.1175/2007JAS2248.1.

Galarneau, T. J., R. McTaggart-Cowan, L. F. Bosart, and C. A. Davis, 2015: Development of North Atlantic Tropical Disturbances near Upper-Level Potential Vorticity Streamers. *J. Atmos. Sci.*, **72**, 572–597, https://doi.org/10.1175/JAS-D-14-0106.1.

Ge, X., T. Li, and M. Peng, 2013: Effects of Vertical Shears and Midlevel Dry Air on Tropical Cyclone Developments*. *J. Atmos. Sci.*, **70**, 3859–3875, https://doi.org/10.1175/JAS-D-13-066.1.

Gray, W. M., 1968: Globla view of the origin of tropical disturbances and storms. *Mon. Weather Rev.*, **96**, 669–700, https://doi.org/10.1175/1520-0493(1968)096<0669:GVOTOO>2.0.CO;2.

——, and R. W. Jacobson, 1977: Diurnal Variation of Deep Cumulus Convection. *Mon. Weather Rev.*, **105**, 1171–1188, https://doi.org/10.1175/1520-0493(1977)105<1171:DVODCC>2.0.CO;2.

Hart, R. E., 2003: A Cyclone Phase Space Derived from Thermal Wind and Thermal Asymmetry. *Mon. Weather Rev.*, **131**, 585–616, https://doi.org/10.1175/1520-0493(2003)131<0585:ACPSDF>2.0.CO;2.

Hendricks, E. A., M. T. Montgomery, and C. a. Davis, 2004: The role of "vortical" hot towers in the formation of tropical cyclone Diana (1984). *J. Atmos. Sci.*, **61**, 1209–1232, https://doi.org/10.1175/1520-0469(2004)061<1209:TROVHT>2.0.CO;2.

Hennon, C. C., C. N. Helms, K. R. Knapp, and A. R. Bowen, 2011: An

objective algorithm for detecting and tracking tropical cloud clusters: Implications for tropical cyclogenesis prediction. *J. Atmos. Ocean. Technol.*, **28**, 1007–1018, https://doi.org/10.1175/2010JTECHA1522.1.

Hess, J. C., J. B. Elsner, and N. E. LaSeur, 1995: Improving Seasonal Hurricane Predictions for the Atlantic Basin. *Weather Forecast.*, **10**, 425–432, https://doi.org/10.1175/1520-0434(1995)010<0425:ISHPFT>2.0.CO;2.

Hoskins, B. J., I. N. James, and G. H. White, 1983: The Shape, Propagation and Mean-Flow Interaction of Large-Scale Weather Systems. *J. Atmos. Sci.*, **40**, 1595–1612, https://doi.org/10.1175/1520-0469(1983)040<1595:TSPAMF>2.0.CO;2.

Hoskins, B. J., M. E. McIntyre, and a. W. Robertson, 1985: of the Meteorological October 1985. *Q. J. R. Meteorol. Soc.*, **111**, 877–946, https://doi.org/10.1002/qj.49711147002.

Houze, R. A., W. C. Lee, and M. M. Bell, 2009: Convective contribution to the genesis of Hurricane Ophelia (2005). *Mon. Weather Rev.*, **137**, 2778–2800, https://doi.org/10.1175/2009MWR2727.1.

Juckes, M., and R. K. Smith, 2000: Convective destabilization by upper-level troughs. *Q. J. R. Meteorol. Soc.*, **126**, 111–123, https://doi.org/10.1002/qj.49712656206.

Kerns, B., K. Greene, and E. Zipser, 2008: Four Years of Tropical ERA-40 Vorticity Maxima Tracks. Part I: Climatology and Vertical Vorticity Structure. *Mon. Weather Rev.*, **136**, 4301–4319, https://doi.org/10.1175/2008MWR2390.1.

Kerns, B. W., and S. S. Chen, 2013: Cloud Clusters and Tropical Cyclogenesis: Developing and Nondeveloping Systems and Their Large-Scale Environment. *Mon. Weather Rev.*, **141**, 192–210,

https://doi.org/10.1175/MWR-D-11-00239.1.

Kiladis, G. N., 1998: Observations of Rossby Waves Linked to Convection over the Eastern Tropical Pacific. *J. Atmos. Sci.*, **55**, 321–339, https://doi.org/10.1175/1520-0469(1998)055<0321:OORWLT>2.0.CO;2.

Lin, Y.-L., and C.-S. Lee, 2011: An analysis of tropical cyclone formations in the South China Sea during the late season. *Mon. Weather Rev.*, **139**, 2748–2760, https://doi.org/10.1175/2011MWR3495.1.

Mapes, B. E., and R. A. Houze, 1993: Cloud Clusters and Superclusters over the Oceanic Warm Pool. *Mon. Weather Rev.*, **121**, 1398–1416, https://doi.org/10.1175/1520-0493(1993)121<1398:CCASOT>2.0.CO;2.

Martius, O., C. Schwierz, and H. C. Davies, 2007: Breaking Waves at the Tropopause in the Wintertime Northern Hemisphere: Climatological Analyses of the Orientation and the Theoretical LC1/2 Classification. *J. Atmos. Sci.*, **64**, 2576–2592, https://doi.org/10.1175/JAS3977.1.

McIntyre, M. E., and T. N. Palmer, 1983: Breaking planetary waves in the stratosphere. *Nature*, **305**, 593–600, https://doi.org/10.1038/305593a0.

McTaggart-Cowan, R., G. D. Deane, L. F. Bosart, C. A. Davis, and T. J. Galarneau, 2008: Climatology of Tropical Cyclogenesis in the North Atlantic (1948–2004). *Mon. Weather Rev.*, **136**, 1284–1304, https://doi.org/10.1175/2007MWR2245.1.

——, T. J. Galarneau, L. F. Bosart, R. W. Moore, and O. Martius, 2013: A global climatology of baroclinically influenced tropical cyclogenesis. *Mon. Weather Rev.*, **141**, 1963–1989, https://doi.org/10.1175/MWR-D-12-00186.1.

Melhauser, C., and F. Zhang, 2014: Diurnal radiation cycle impact on the

pregenesis environment of Hurricane Karl (2010). *J. Atmos. Sci.*, **71**, 1241–1259, https://doi.org/10.1175/JAS-D-13-0116.1.

Montgomery, M. T., M. E. Nicholls, T. a. Cram, and a. B. Saunders, 2006: A Vortical Hot Tower Route to Tropical Cyclogenesis. *J. Atmos. Sci.*, **63**, 355–386, https://doi.org/10.1175/JAS3604.1.

Nolan, D. S., Y. Moon, and D. P. Stern, 2007: Tropical Cyclone Intensification from Asymmetric Convection: Energetics and Efficiency. *J. Atmos. Sci.*, **64**, 3377–3405, https://doi.org/10.1175/JAS3988.1.

Olander, T. L., and C. S. Velden, 2009: Tropical Cyclone Convection and Intensity Analysis Using Differenced Infrared and Water Vapor Imagery. *Weather Forecast.*, **24**, 1558–1572, https://doi.org/10.1175/2009WAF2222284.1.

Orlanski, I., 1975: A rational Subdivision of Scales for Atmospheric Processes. *Am. Meteorol. Soc.*, **56**, 527–530, https://doi.org/10.1234/12345678.

Park, M.-S., Y.-S. Choi, C.-H. Ho, C.-H. Sui, S. K. Park, and M.-H. Ahn, 2007: Regional cloud characteristics over the tropical northwestern Pacific as revealed by Tropical Rainfall Measuring Mission (TRMM) Precipitation Radar and TRMM Microwave Imager. *J. Geophys. Res.*, **112**, D05209, https://doi.org/10.1029/2006JD007437.

——, H.-S. Kim, C.-H. Ho, R. L. Elsberry, and M.-I. Lee, 2015: Tropical Cyclone Mekkhala's (2008) Formation over the South China Sea: Mesoscale, Synoptic-Scale, and Large-Scale Contributions. *Mon. Weather Rev.*, **143**, 88–110, https://doi.org/10.1175/MWR-D-14-00119.1.

Park, M., R. L. Elsberry, and P. a. Harr, 2013: Vertical wind shear and ocean heat contents as environmental modulators of western North Pacific

tropical cyclone intensification and decay. *Trop. CYCLONE Res. Rev.*, **1**, 448–457, https://doi.org/10.6057/2012TCRR04.03.

Park, M. S., C. H. Ho, J. Kim, and R. L. Elsberry, 2011: Diurnal circulations and their multi-scale interaction leading to rainfall over the South China Sea upstream of the Philippines during intraseasonal monsoon westerly wind bursts. *Clim. Dyn.*, **37**, 1483–1499, https://doi.org/10.1007/s00382-010-0922-z.

Penny, A. B., P. A. Harr, and M. M. Bell, 2015: Observations of a nondeveloping tropical disturbance in the western North Pacific during TCS-08 (2008). *Mon. Weather Rev.*, **143**, 2459–2484, https://doi.org/10.1175/MWR-D-14-00163.1.

Postel, G. A., and M. H. Hitchman, 1999: A Climatology of Rossby Wave Breaking along the Subtropical Tropopause. *J. Atmos. Sci.*, **56**, 359–373, https://doi.org/10.1175/1520-0469(1999)056<0359:ACORWB>2.0.CO;2.

Puschell, J. J., and Coauthors, 2002: Japanese Advanced Meteorological Imager: a next generation GEO imager for MTSAT-1R. *Earth Observing Systems VII*, W.L. Barnes, Ed., Vol. 4814 of, 152.

Raymond, D. J., 1992: Nonlinear Balance and Potential-Vorticity Thinking At Large Rossby Number. *Q. J. R. Meteorol. Soc.*, **118**, 987–1015, https://doi.org/10.1002/qj.49711850708.

——, and C. L. Carrillo, 2011: The vorticity budget of developing typhoon Nuri (2008). *Atmos. Chem. Phys.*, **11**, 147–163, https://doi.org/10.5194/acp-11-147-2011.

——, S. L. Sessions, and C. López Carrillo, 2011: Thermodynamics of tropical cyclogenesis in the northwest Pacific. *J. Geophys. Res.*, **116**, D18101, https://doi.org/10.1029/2011JD015624.

Reynolds, R. W., T. M. Smith, C. Liu, D. B. Chelton, K. S. Casey, and M. G. Schlax, 2007: Daily high-resolution-blended analyses for sea surface temperature. *J. Clim.*, **20**, 5473–5496, https://doi.org/10.1175/2007JCLI1824.1.

Ritchie, E. A., and G. J. Holland, 1999: Large-Scale Patterns Associated with Tropical Cyclogenesis in the Western Pacific. *Mon. Weather Rev.*, **127**, 2027–2043, https://doi.org/10.1175/1520-0493(1999)127<2027:LSPAWT>2.0.CO;2.

Sadler, J. C., 1975: *Tropical cyclone initiation by the tropical upper tropospheric trough*. 35 pp.

——, 1976: A role of the tropical upper tropospheric trough in early season typhoon development. *Mon. Weather Rev.*, **104**, 1266–1278, https://doi.org/10.1175/1520-0493(1976)104<1266:AROTTU>2.0.CO;2.

——, 1978: Mid-season typhoon development and intensity changes and the tropical upper tropospheric trough. *Mon. Weather Rev.*, **106**, 1137–1152, https://doi.org/10.1175/1520-0493(1978)106<1137:MSTDAI>2.0.CO;2.

Schmetz, J., S. a. Tjemkes, M. Gube, and L. van de Berg, 1997: Monitoring deep convection and convective overshooting with METEOSAT. *Adv. Sp. Res.*, **19**, 433–441, https://doi.org/10.1016/S0273-1177(97)00051-3.

Tang, B., and K. Emanuel, 2012: A ventilation index for tropical cyclones. *Bull. Am. Meteorol. Soc.*, **93**, 1901–1912, https://doi.org/10.1175/BAMS-D-11-00165.1.

Trenberth, K. E., 1978: On the Interpretation of the Diagnostic Quasi-Geostrophic Omega Equation. *Mon. Weather Rev.*, **106**, 131–137, https://doi.org/10.1175/1520-

0493(1978)106<0131:OTIOTD>2.0.CO;2.

Wang, C., and L. Wu, 2016: Interannual shift of the tropical upper-tropospheric trough and its influence on tropical cyclone formation over the western North Pacific. *J. Clim.*, **29**, 4203–4211, https://doi.org/10.1175/JCLI-D-15-0653.1.

Wang, Z., 2014: Role of cumulus congestus in tropical cyclone formation in a high-resolution numerical model simulation. *J. Atmos. Sci.*, **71**, 1681–1700, https://doi.org/10.1175/JAS-D-13-0257.1.

Waugh, D. W., and L. M. Polvani, 2000: Climatology of intrusions into the tropical upper troposphere. *Geophys. Res. Lett.*, **27**, 3857–3860, https://doi.org/10.1029/2000GL012250.

——, and B. M. Funatsu, 2003: Intrusions into the tropical upper troposphere: three-dimensional structure and accompanying ozone and OLR distributions. *J. Atmos. Sci.*, **60**, 637–653, https://doi.org/10.1175/1520-0469(2003)060<0637:IITTUT>2.0.CO;2.

Wernli, H., and M. Sprenger, 2007: Identification and ERA-15 Climatology of Potential Vorticity Streamers and Cutoffs near the Extratropical Tropopause. *J. Atmos. Sci.*, **64**, 1569–1586, https://doi.org/10.1175/JAS3912.1.

Wissmeier, U., and R. K. Smith, 2011: Tropical cyclone convection: the effects of ambient vertical vorticity. *Q. J. R. Meteorol. Soc.*, **137**, 845–857, https://doi.org/10.1002/qj.819.

Wu, L., C. Wang, and B. Wang, 2015: Westward shift of western North Pacific tropical cyclogenesis. *Geophys. Res. Lett.*, **42**, 1537–1542, https://doi.org/10.1002/2015GL063450.

Yang, S., and E. A. Smith, 2006: Mechanisms for Diurnal Variability of Global Tropical Rainfall Observed from TRMM. *J. Clim.*, **19**, 5190–

5226, https://doi.org/10.1175/JCLI3883.1.

Zawislak, J., and E. J. Zipser, 2014a: A Multisatellite Investigation of the Convective Properties of Developing and Nondeveloping Tropical Disturbances. *Mon. Weather Rev.*, **142**, 4624–4645, https://doi.org/10.1175/MWR-D-14-00028.1.

——, and ——, 2014b: Analysis of the Thermodynamic Properties of Developing and Nondeveloping Tropical Disturbances Using a Comprehensive Dropsonde Dataset. *Mon. Weather Rev.*, **142**, 1250–1264, https://doi.org/10.1175/MWR-D-13-00253.1.

Zehr, Raymond Milton, 1992: Tropical Cyclogenesis in the Western North Pacific. *Thesis (PH.D.)--COLORADO STATE Univ.,*.

Zhang, G., Z. Wang, T. J. Dunkerton, M. S. Peng, and G. Magnusdottir, 2016: Extratropical Impacts on Atlantic Tropical Cyclone Activity. *J. Atmos. Sci.*, **73**, 1401–1418, https://doi.org/10.1175/JAS-D-15-0154.1.

——, ——, M. S. Peng, and G. Magnusdottir, 2017: Characteristics and impacts of extratropical Rossby Wave breaking during the Atlantic hurricane season. *J. Clim.*, **30**, 2363–2379, https://doi.org/10.1175/JCLI-D-16-0425.1.

국문 초록

태풍이 발생하는 과정을 인공위성에서 관찰하면 열대 요란이 동반하는 깊은 대류 면적이 며칠 동안 반복적인 일변화를 겪으며 점차 성장하는 과정이 자주 관찰되어 왔으며 이 현상은 열대 요란이 점진적으로 조직화되는 과정으로 이해되며 많은 선행연구에서 보고되어 왔다. 그러나 실제로 이러한 깊은 대류 면적의 일변화 현상이 태풍 발생의 전조증상으로 여겨질 수 있는지에 대한 깊은 논의나, 태풍으로 발달하지 않고 소멸하는 열대 요란에서 유사한 현상이 관찰되지 않는지에 대한 비교는 이루어진 바가 없다. 따라서 이 학위 논문에서는 2007년부터 2009년까지 북서태평양에서 태풍으로 발달한 열대 요란 사례 80개와 태풍으로 발달하지 못하고 소멸한 열대 요란 383개 사례를 대상으로 각 열대 요란이 동반하는 깊은 대류의 면적을 약 5일간 관찰하여 정량적인 분석을 수행하였다. 대류권 계면 고도까지 높게 도달하는 깊은 대류의 면적은 정지궤도 위성에서 관측한 적외(Infrared; IR) 및 수증기(Water Vapor; WV) 채널 밝기온도 차이 값을 이용하여 적외 채널 밝기온도 값보다 수증기 채널의 밝기온도 값이 높아지는 영역(IR minus WV <0)의 면적으로 계산했다. 깊은 대류의 면적이 일주기에 따라 극소점에서 극대점으로 증가하는 것을 깊은

대류의 폭발(Convective Burst; CB)이라고 정의하였으며 이러한 깊은 대류의 폭발이 최소 이틀이상 연속하여 나타나는 경우에 깊은 대류 면적의 일변화 현상이 규칙적으로 나타나는 것으로 정의하고 이 현상을 ‘Multi-day Convective Bursts (이하 mCB)’라고 명명하였다. 아울러 수일에 거친 태풍 발달 및 비발달과정에서 나타나는 깊은 대류의 변화를 대기환경 변화와 함께 이해하고자 Modern-Era Retrospective Analysis for Research and Applications, Version 1, 2와 ECMWF ReAnalysis-5를 분석하였다.

그 결과 태풍으로 발달하는 열대 요란 80개중 67.5%에 해당하는 54개의 열대 요란에서만 mCB가 관찰되었다. 이와 유사하게 태풍으로 발달하지 않는 열대 요란 383개 중 13.8%에 해당하는 53개의 열대 요란에서도 mCB가 관찰되었다. mCB가 관찰되는 두 열대 요란 그룹의 대기환경조건을 살펴보았을 때, 열역학적인 환경은 유사하게 나타났으며 역학적인 환경에서 유의한 차이점이 발견되었다. 특히 태풍으로 발달하는 열대 요란보다 비발달 열대 요란에서 대류권 하층 상대와도의 강도가 유의하게 약했으며 필터링 기법을 이용하여 규모를 나누어 분석한 결과 태풍으로 발달하는 열대 요란은 하층 저기압 주변에 상대적인 고기압 아노말리가 뚜렷하게 나타났지만 비발달 열대 요란 주변에서는 이러한

고기압 아노말리가 뚜렷하게 나타나지 않았다. 고기압과 저기압이 반복되는 파동패턴은 저기압 내부로 수증기의 유입을 효율적으로 수렴해 태풍 발달에 기여할 수 있다. 나아가 태풍으로 발달하는 열대 요란보다 비발달 열대 요란 주변의 연직 바람시어 또한 유의하게 강한 것으로 나타났으며 대류권 중층에서 상층까지의 바람시어 환경이 전체 대류권 연직 바람시어의 대부분을 차지했다. mCB가 관찰되는 열대 요란의 태풍 발달 과정의 특징은 2008년 태풍 하구핏 사례분석을 통해 재확인할 수 있었다.

태풍으로 발달하는 열대 요란 80개중 나머지 32.5%에 해당하는 26개 열대 요란에서는 mCB가 관찰되지 않고 며칠 동안 깊은 대류의 활동이 억제되어 있다가 태풍으로 발달하기 하루 또는 이틀전에 깊은 대류 활동이 시작되는 특징을 보였다. 열역학적으로도 주변 환경이 깊은 대류 활동이 활발하기 일어나기에 어려웠다. 역학적인 특징으로는 대류권내에서 상대와도 최대치가 나타나는 위치 및 연직 바람시어 강도에서 mCB가 관찰되는 열대 요란과 뚜렷한 차이를 보였다. 먼저 mCB가 관찰되는 열대 요란의 경우에는 상대와도가 대류권 하층에서 가장 강하게 나타나는 반면 mCB가 관찰되지 않는 열대 요란 중 12개의 열대 요란에서는 대류권 상층에서 상대와도가 가장 강하게 나타났다. 이를 상세하기 이해하기

위하여 2007년 태풍 페이파의 사례분석을 수행하였고 그 결과 페이파의 태풍발생과정이 북대서양에서는 상대적으로 빈번하게 나타나는 열대 전이 과정에 해당한다는 것을 알 수 있었다. 열대전이과정은 태풍발생과정 중 한가지로 중위도 성층권 하부에서 열대 대류권 상층으로 절대와도가 섭입될 때 생겨나는 대기 불안정 및 준지균힘에 의해 대류권 하층에 저기압 아노말리가 생겨나 이후에 태풍으로 발달하는 과정이다. 따라서 12개의 열대 요란은 이러한 열대전이과정을 통해 태풍으로 발달하였고 그 때문에 발생 이전에 mCB가 관찰되지 않으며 대류권 상층에 상대와도의 최대치가 나타났다. 태풍으로 발달하지만 mCB가 관찰되지 않는 나머지 14개의 열대 요란의 주변 대기환경장을 분석해 보았을 때에는 mCB가 관찰되는 열대 요란과 유사한 특징을 나타냈다. 대류권 하층에서 하층 저기압 주변에 상대적인 고기압 아노말리도 뚜렷하게 확인되었다. 다만, CB의 강도가 mCB 정의 기준에 비해 상대적으로 약하게 나타났으며 상대와도의 최대치가 대류권 중층에 나타났다는 점이 달랐다. 대류권 계면까지는 도달하지 않는 얕은 대류 활동과 상대와도 최대치의 위치를 고려하여 분석한다면 해당 태풍발생과정을 보다 상세하게 이해할 수 있을 것으로 기대된다.

정리하면, 이 학위 논문에서는 mCB와 태풍 발생의 정량적인 관계를

파악했고 mCB가 관찰되는지 여부를 기준으로 태풍발생과정을 구분하여 이해할 수 있었다. 먼저 태풍으로 발달하는 열대 요란과 비슷하게 태풍으로 발달하지 않는 열대 요란에서도 mCB가 관찰되기 때문에 mCB를 태풍발생 여부를 예측하는 단일 인자로 활용하기에는 어렵다는 결론을 얻을 수 있었다. 단, 연직바람시어의 강도나 대류권 하층의 상대와도 및 주변 고기압 아노말리를 같이 파악한다면 태풍 발생 예측에 이용할 수 있을 것이다. 두번째로 북서태평양 일부 태풍발생과정은 mCB가 관찰되지 않는다는 것을 파악했으며 이러한 경우 중 절반은 대류권 상부에서 작용하는 역학·열역학적 물리력이 태풍 발생에 기여한다는 것을 알 수 있었다. 마지막으로 mCB가 태풍으로 발달하지 않는 열대 요란을 매우 효율적으로 제거해 낼 수 있다는 점을 알 수 있었다.

핵심어: 태풍 발생, 깊은 대류, 일주기 변화, 열대 요란, 열대 전이, 북서태평양, 열대-온대 상호작용

학 번: 2013-20340